United States Nuclear Regulatory Commission

Protecting People and the Environment

NUREG/CR-6879
ANL-05/16

Steam Generator Tube Integrity Issues: Pressurization Rate Effects, Failure Maps, Leak Rate Correlation Models, and Leak Rates in Restricted Areas

Office of Nuclear Regulatory Research

United States Nuclear Regulatory Commission

Protecting People and the Environment

NUREG/CR-6879
ANL-05/16

Steam Generator Tube Integrity Issues: Pressurization Rate Effects, Failure Maps, Leak Rate Correlation Models, and Leak Rates in Restricted Areas

Manuscript Completed: October 2008
Date Published: July 2009

Prepared by
S. Majumdar, K. Kasza, S. Bakhtiari, J.Y. Park, J. Oras
J. Franklin, C. Vulyak, and W.J. Shack

Nuclear Engineering Division
Argonne National Laboratory
9700 South Cass Avenue
Argonne, IL 60439

M. Stambaugh, NRC Project Manager

NRC Job Code N6582

Office of Nuclear Regulatory Research

This page is intentionally left blank.

Abstract

This report summarizes results obtained under the Third International Steam Generator Tube Integrity Program (ISG–TIP–3). Tests were conducted to determine the effect of pressurization rate on rupture of flawed tubes. Based on analysis and tests, failure maps were developed that delineate ranges of ligament and crack sizes that could be susceptible to ligament rupture and/or unstable burst due to pressure drops of ΔP_{NO} (normal operation), ΔP_{MSLB} (main steam-line break), $1.4\Delta P_{MSLB}$, and $3\Delta P_{NO}$. Tests were conducted to determine the limits of applicability with respect to the through wall crack length and crack tightness of the simple orifice model for predicting leak rates of cracked tubes. Finally, leak rates were calculated for degraded tubes in restricted areas during postulated design-basis and severe accident conditions.

This page is intentionally left blank.

Foreword

This report discusses a study conducted by Argonne National Laboratory (ANL), under contract to the U.S. Nuclear Regulatory Commission (NRC), to evaluate four different steam generator (SG) tube integrity topics.

The first topic examines the effect of pressurization rate on steam generator (SG) tube burst pressure. Industry tests of pressurization rate suggest that rate has a significant effect. ANL noted industry's use of inconsistent test procedures. Argonne laboratory conducted these tests using more consistent test procedures. The results showed that the pressurization rate had a small effect which increases as the flaw size decreases.

In the second section, finite element calculations were used to develop failure maps for ligamented flaws. Stress corrosion cracks generally consist of multiple cracks separated by ligaments. Although ligament geometries may be complex, this study idealized the ligaments as radial, axial, or circumferential. At a SG tube rupture point, partial-throughwall radial cracks become throughwall. By contrast, the rupture of axial or circumferential ligaments results in longer cracks, which could subsequently rupture under normal or accident conditions. The ANL failure maps show the range of ligament and crack sizes that would be susceptible to ligament rupture during normal or accident conditions.

The applicability of an orifice flow model is examined in the third topic of this NUREG. ANL conducted tests to establish orifice flow model leak rates. The results show that the orifice flow model remains valid when the length of the orifice (i.e., the tube wall thickness) is less than approximately five times the hydraulic diameter of the flaw.

The final section examines the leak rate from flaws located under the tube support plate (TSP) during a postulated main steam line break (MSLB) and under severe accident conditions. ANL analyzed and predicted the flaw opening area during a postulated MSLB and the expected leak rates from cracks located under the TSP. Results indicate that the size of a crack opening and leak rate may be affected by SG tube contact with the tube support plate.

This research may be used by the NRC in assessment of industry SG tube integrity evaluations. The results may be useful to NRC staff during reviews of license amendment requests and other licensing actions. Regional inspectors may also find the information valuable when verifying proper implementation of licensee steam generator programs.

Michael J. Case, Director
Division of Engineering
Office of Nuclear Regulatory Research
U.S. Nuclear Regulatory Commission

This page is intentionally left blank.

Contents

Abstract iii

Foreword v

Executive Summary xvii

Acknowledgments xxi

List of Acronyms xxiii

List of Symbols xxv

1 Pressurization Rate Effect on Burst Pressure 1

1.1 Introduction 1

1.2 Factors Influencing Tests to Determine Pressurization Rate Effect 1

1.2.1 Initial test series 2

1.3 Test Specimens for the Second Series 4

1.4 Test Procedure for the Second Series 5

1.5 Test Results for the Second Series 5

1.5.1 Tests on 25 mm (1 in.) Long EDM Flaws 5

1.5.2 Tests on Short EDM Flaws 7

1.5.3 Tests on Stress Corrosion Cracks 7

1.6 Analysis of Test Results 7

1.6.1 Predicted Failure Pressures 7

1.6.2 Post-Test Observations of Specimens 9

1.7 Conclusions 9

2 Failure Maps for Complex Multiple Cracks 11

2.1 Introduction 11

2.2 Background Analysis and Tests 13

2.2.1 Throughwall Axial Cracks 13

2.2.2 Part–Throughwall Axial Cracks 15

2.3 Parametric Analyses for Axial Throughwall Cracks 16

2.4 Generation of Failure Maps 22

2.4.1 Failure Maps for Normal Operation (ΔP_{NO}) 22

2.4.2 Failure Maps for Main Steam Line Break Pressure (ΔP_{MSLB}) 25
2.4.3 Failure Maps for 1.4xMain Steam Line Break Pressure ($1.4\Delta P_{MSLB}$)..... 28
2.4.4 Failure Maps for 3xNormal Operating Pressure ($3\Delta P_{NO}$)..... 31
2.5 Discussion and Conclusions 34
3 Leak Rate Studies 37
3.1 Introduction 37
3.2 Test Procedure..... 37
3.3 Test Results..... 38
3.3.1 Stage 1 Room Temperature Test Results..... 38
3.3.2 Stage 2 High Temperature Test Results Under MSLB Condition 44
3.4 Leak Rate Model 49
3.5 Conclusions..... 53
4 Leak Rates in Restricted Areas 55
4.1 Introduction 55
4.2 Currently Available Leak Rate Data 55
4.2.1 Westinghouse/EPRI Tube/TSP Data 55
4.2.2 Dampierre-1 Tube/TSP Data..... 57
4.2.3 Tube/Tube-Sheet Data from a Retired Steam Generator..... 58
4.3 Analyses of Crack Opening Area and Leak Rate 59
4.3.1 Leak Rate Correlation for MSLB 60
4.3.2 Leak Rate Correlation for Severe Accidents..... 60
4.3.3 Material Properties Used in Analysis..... 61
4.4 Results 62
4.4.1 Main Steam-Line Break (MSLB) Conditions 62
4.4.2 Severe Accident Conditions 66
4.5 Effect of Crevice Deposits on Crack Opening and Leak Rate 69
4.6 Conclusions..... 71
5 References..... 73

Figures

1. Notch depth profile for Type 14 specimen. m_p denotes radial ligament stress magnification factor. 2

2. Type A: single rectangular notch and Type B: single trapezoidal notch. 4

3. Type C: 2–colinear notches (axial ligament) and Type D: 2–offset notches (circumferential ligament)..... 5

4. Predicted vs. observed ligament rupture pressure for quasi–static to 14 MPa /s (2 ksi/s) tests. 8

5. Variation of (a) test ligament rupture pressures and (b) normalized test ligament rupture pressures with pressurization rate. 9

6. Typical stress corrosion crack geometry. 11

7. Idealized single part–throughwall axial crack with a radial ligament. 12

8. Two idealized part–throughwall axial cracks each with a radial ligament at the through-thickness crack tip and separated from each other by either an axial (Type C) or a circumferential (Type D or Type E) ligament. 12

9. Two-TW axial notches separated by (a) an axial ligament (Type C) and (b) a circumferential ligament (Type D). 13

10. Engineering and true stress–strain curves of Alloy 600 used for finite element analysis. 14

11. Calculated variation of average inter–notch axial ligament thickness with pressure using finite deformation analyses by ANSYS and ABAQUS for two 6–mm (0.25–in.) long axial cracks separated by a 0.25–mm (0.01–in.) long axial ligament (Type C). 14

12. Predicted (by FEA, line) vs. observed (symbols) variation of ligament rupture pressure with circumferential ligament length for type D specimens having two 6– and 13–mm long TW notches. 15

13. Predicted (line) and observed (symbols) radial through–thickness ligament rupture pressures vs. axial or circumferential ligament lengths for two PTW EDM notches (a) 6–mm (0.25–in.) and (b) 13–mm (0.5–in.) long. 16

14. Specimens with two throughwall axial cracks, separated by (a) an axial ligament (Type C) and (b) a circumferential ligament (Type D), analyzed by FEA. 17

15. Specimens with (a) four and (b) six axial throughwall cracks analyzed by FEA. 17

16. Axial ligament rupture pressure for two throughwall axial cracks separated by an axial ligament. 17

17. Variation of fitting parameters (a) a_1 and (b) a_2 with crack length (in mm) for specimens with two throughwall axial cracks separated by an axial ligament. 18

18. Axial ligament rupture pressure for four throughwall axial cracks separated by three equally long axial ligaments. Symbols represent FEA results and lines are polynomial fits of the FEA results to Eq. 1. 18

19. Variation of fitting parameters (a) a_1 and (b) a_2 with crack length (in mm) for specimens with four throughwall axial cracks separated by three axial ligaments.. 19

20. Axial ligament rupture pressure for six throughwall axial cracks separated by five equally wide axial ligaments. Symbols represent FEA results and lines are polynomial fits of the FEA results to Eq. 1. 19

21. Variation of fitting parameters (a) a_1 and (b) a_2 with crack length for specimens with six throughwall axial cracks separated by five axial ligaments. 20

22. Circumferential ligament rupture pressure for two throughwall axial cracks separated by a circumferential ligament. 20

23. Variation of fitting parameters M_0, M_1, and M_2 with crack length for specimens with two throughwall axial cracks separated by a circumferential ligament. 21

24. Effects of axial and circumferential ligament widths on ligament rupture pressure of two 12 mm 100%TW axial cracks separated by axial or circumferential ligaments (total crack length = 25 mm) 21

25. Failure map of a single crack at normal operating pressure ΔP_{NO}. 23

26. Failure maps for SG tubes with two 90% deep axial cracks separated by (a) an axial ligament (Type C) and (b) a circumferential ligament (Type D) at normal pressure (ΔP_{NO}). 24

27. Failure maps for SG tubes with (a) four and (b) six 90% deep axial cracks separated by axial ligaments at normal pressure (ΔP_{NO}). "Crack length" denotes the total overall length of the individual cracks and ligaments. 25

28. Failure map of a single crack at main steam line break pressure ΔP_{MSLB}. 25

29. Failure maps for SG tubes with two 90% deep axial cracks separated by (a) an axial ligament (Type C) and (b) a circumferential ligament (Type D) at main steam line break pressure (ΔP_{MSLB}). "Crack length" denotes the total overall length of the individual cracks and ligaments. 26

30. Failure maps for SG tubes with two 80% deep axial cracks separated by (a) an axial ligament (Type C) and (b) a circumferential ligament (Type D) at main steam line break pressure (ΔP_{MSLB}). "Crack length" denotes the total overall length of the individual cracks and ligaments 26

31. Failure maps for SG tubes with four axial cracks, (a) 90% and (b) 80% deep, separated by three axial ligaments (Type C) at main steam line break pressure (ΔP_{MSLB}). "Crack length" denotes the total overall length of the individual cracks and ligaments 27

32. Failure maps for SG tubes with six axial cracks, (a) 90% and (b) 80% deep, separated by five axial ligaments (Type C) at main steam line break pressure (ΔP_{MSLB}). "Crack length" denotes the total overall length of the individual cracks and ligaments. 28

33. Failure map of a single crack at 1.4 times main steam line break pressure $1.4\Delta p_{MSLB}$. 28

34. Failure maps for SG tubes with two 90% deep axial cracks separated by (a) an axial ligament (Type C) and (b) a circumferential ligament (Type D) at 1.4 times main steam line break pressure ($1.4\Delta P_{MSLB}$). "Crack length" denotes the total overall length of the individual cracks and ligaments..... 29

35. Failure maps for SG tubes with two 80% deep axial cracks separated by (a) an axial ligament (Type C) and (b) a circumferential ligament (Type D) at 1.4 times main steam line break pressure ($1.4\Delta P_{MSLB}$). "Crack length" denotes the total overall length of the individual cracks and ligaments..... 30

36. Failure maps for SG tubes with four axial cracks, (a) 90% and (b) 80% deep, separated by three axial ligaments (Type C) at 1.4 times main steam line break pressure ($1.4\Delta P_{MSLB}$). "Crack length" denotes the total overall length of the individual cracks and ligaments 30

37. Failure maps for SG tubes with six axial cracks, (a) 90% and (b) 80% deep, separated by five axial ligaments (Type C) at 1.4 times main steam line break pressure ($1.4\Delta P_{MSLB}$). "Crack length" denotes the total overall length of the individual cracks and ligaments.. 31

38. Failure map of a single crack at 3 times normal operating pressure $3\Delta P_{NO}$. 31

39. Failure maps for SG tubes with two 90% deep axial cracks separated by (a) an axial ligament (Type 2) and (b) a circumferential ligament (Type 4) at 3 times normal operating pressure ($3\Delta P_{NO}$). "Crack length" denotes the total overall length of the individual cracks and ligaments 32

40. Failure maps for SG tubes with two 80% deep axial cracks separated by (a) an axial ligament (Type C) and (b) a circumferential ligament (Type D) at 3 times normal operating pressure ($3\Delta P_{NO}$). "Crack length" denotes the total overall length of the individual cracks and ligaments. 33

41. Failure maps for SG tubes with four axial cracks, (a) 90% and (b) 80% deep, separated by three axial ligaments (Type C) at 3 times normal operating pressure ($3\Delta P_{NO}$). "Crack length" denotes the total overall length of the individual cracks and ligaments. 33

42. Failure maps for SG tubes with six axial cracks, (a) 90% and (b) 80% deep, separated by five axial ligaments (Type C) at 3 times normal operating pressure ($3\Delta P_{NO}$). "Crack length" denotes the total overall length of the individual cracks and ligaments. 34

43. Stage 1 leak–rate behavior of ODSCC axial Flaw (a) SGL750 and (b) SGL905 under a constant pressure of 17.2 MPa (2500 psi) with room–temperature water. 39

44. Stage 1 leak–rate behavior of ODSCC axial flaw (a) SGL904 and (b) SGL911 under constant pressure of 17.2 MPa (2500 psi) with room–temperature water. 39

45. SCC axial flaw SGL750–OM–3/19/03. 40

46. SCC axial flaw SGL904–OM–1/15/03. 40

47. SCC axial flaw SGL905–OM–3/24/03. 40

48. SCC axial flaw SGL911–OM–2–1/20/03. 41

49. Magnified image of feature sf1 in SCC flaw SGL904–OM, which appears to be an intact or possibly torn ligament. 41

50. Image analysis line drawn between the end points of SCC flaw SGL905–OM used to calculate flaw length. 42

51. Image analysis line drawn around the crack perimeter of SCC flaw SGL905–OM by the wand method to define the opening 42

52. Crack opening of SCC flaw SGL905–OM highlighted by the threshholding method 42

53. Stage 2 SCC axial flaw SGL750 after the high temperature test. 46

54. Stage 2 SCC axial flaw SGL 904 after the high temperature test. 46

55. Stage 2 SCC axial flaw SGL905–BDTF–4/15/03. 46

56. Stage 2 SCC axial flaw SGL911 after the high temperature test. 46

57. Comparison of crack opening areas at the ID and OD for a 12.7 mm (0.5 in.) crack at 288°C. Results are shown for finite–element solutions using solid and shell elements as well as the analytical solution of Zahoor. 48

58. Comparison of crack opening areas at the ID and OD for a 19.0 mm (0.75 in.) crack at 288°C. Results are shown for finite–element solutions using solid and shell elements as well as the analytical solution of Zahoor. 48

59. L/D for cracks in SG tubes under normal operating pressures and MSLB conditions. The flow length L is taken as the wall thickness and the hydraulic diameter D is 2δ, where δ is the average cracking opening. 50

60. Test results from Amos and Schrock[8] on flashing as a function of stagnation pressure and subcooling for (a) L/D=85 and (b) L/D=135. Numbers next to symbols denote location of flashing in cm from entrance (wall thickness=6.35 cm)... 50

61. Flow loss factor as a function of L/D for Amos and Shrock slit tests[8] and tests on SG tubes. 52

62. Gap flow area for a tube with an axial crack inside the TSP. 56

63. Correlation of leak rate data with (a) throughwall crack opening area and (b) limiting flow area. 57

64. Optical metallography of a cross-section parallel to the tube axis at the maximum EC signals for TS0601 Alloy 600 SG tube specimen R39C43 near the TTS. 59

65. A throughwall circumferential ODSCC with crack branching in specimen No. 9 just below the top of the tube sheet. The crack opening is about 0.04 mm. 59

66. Finite element model of the tube-to-TSP junction. 60

67. True stress-plastic strain curves for Alloy 600. 61

68. Creep rate properties of Alloy 600. 62

69. Axial variation of radial gap between crack flank and the inner surface of the TSP tube hole with pressure for (a) 13 mm (0.5 in.) and (b) 19 mm (0.75 in.) axial cracks at 300°C. 63

70. Variation of gap opening area, OD crack opening area, and ID crack opening area with pressure for (a) 13 mm (0.5 in.) and (b) 19 mm (0.75 in.) axial crack at 300°C 63

71. Variation of leak rate with pressure for (a) 13 mm (0.5 in.) and (b) 19 mm (0.75 in.) axial crack at 300°C 64

72. Circumferential variation of radial gap between crack flank and the inner surface of the TSP tube hole with pressure for (a) 180° and (b) 240° cracks at 300°C. 64

73. Radial gap variation between the tube OD surface and the TSP hole/wall for 90, 180, and 240° circumferential cracks at the postulated MSLB condition. 65

74. Variation of gap opening area and ID crack opening area with pressure for (a) 90° and (b) 180° circumferential crack at 300°C. 65

75. Variation of gap opening area and ID and OD crack opening areas with pressure for a 240° circumferential crack. 66

76. Variation of leak rate with pressure for 90, 180, and 240° cracks at 300°C. 66

77. Variation of (a) temperature and (b) pressure with time assumed for severe accident analysis. 67

78. Axial variation of radial gap between crack flank and the inner surface of the TSP tube hole with time for (a) 13 mm (0.5 in.) and (b) 19 mm (0.75 in.) axial cracks at a pressure of 17 MPa (2.5 ksi). 67

79. Variation of gap opening area, OD crack opening area, and ID crack opening area with time for (a) 13 mm (0.5 in.) and (b) 19 mm (0.75 in.) axial crack. 68

80. Variation of leak rate with time for (a) 13 mm (0.5 in.) and (b) 19 mm (0.75 in.) axial crack. 68

81. Variation of gap opening area and ID crack opening area with time for (a) 90° and (b) 180° circumferential crack. 69

82. Variation of gap opening area and ID and OD crack opening areas with time for 240° circumferential crack. 69

83. Variation of leak rate with time for 90°, 180°, and 240° circumferential cracks during a postulated severe accident. 69

84. Effect of elastic modulus of sludge on the crack opening displacement of 13 mm (0.5 in.) axial crack..... 70

Tables

1. Ligament rupture pressures for < 25 mm (1 in.) long, part–throughwall rectangular EDM flaws with and without bladder 3

2. Unstable burst pressures (Stage 2) for < 25 mm (1 in.) long, part–throughwall and throughwall rectangular EDM flaws with and without bladder and foil. 4

3. EDM flaw ligament rupture pressure (Stage 1) for four flaw types (Types A, B, C, and D in Figs. 2–3) and five different pressurization rates. 6

4. EDM flaw unstable burst pressure (Stage 2) for four flaw types (Types A, B, C, and D in Figs. 2–3) and five different pressurization rates. 6

5. Axial crack lengths and opening areas after the RT tests 43

6. Variation of gap width along the crack, average gap, flaw length, and area. 44

7. Crack opening geometries and flow behavior in tests at 288°C. 47

8. Comparison of orifice model predictions and experimental results for the RT tests. 49

9. Comparison of orifice model predictions and experimental results for the tests at 288°C for different back–pressures 49

10. A summary of leak test data for tube/TS specimens from the retired SG. Note 1000 psi = 6.895 MPa and 1 gallon = 3.8 L. 58

Executive Summary

This report summarizes results on four topics obtained under the Third International Steam Generator Tube Integrity Program (ISG–TIP–3).

A Pressurization rate effects on flawed tube rupture pressure

The question of whether ligament rupture pressure or unstable burst pressure may vary significantly with pressurization rate at room temperature arose from the results of pressure tests by Westinghouse on tubes with machined part–throughwall notches. Slow (quasi–static) and fast 14 MPa/s (2000 psi/s) pressurization rate tests on specimens with nominally the same notch geometry appeared to show a significant effect of the rate of pressurization on the unstable burst pressure. Unfortunately, the slow and fast loading rate tests were conducted following two different test procedures, which could confound the results. The current series of tests were conducted on a variety of specimen geometries using a consistent test procedure to better establish the effect of pressurization rate.

Tests conducted on specimens with 25 mm (1 in.) long rectangular or trapezoidal notches and specimens with two rectangular notches separated by an axial or circumferential ligament did not show a significant effect of pressurization rate effect on the ligament rupture or unstable burst pressure. The tests show a small effect of pressurization rate on ligament rupture pressure for rates > 7 MPa/s (1000 psi/s) for rectangular notches < 25 mm (1 in.) long with shorter notches experiencing slightly greater rate effects than longer ones. However, the observed increases in ligament rupture pressure at 14 MPa/s (2000 psi/s), which is the upper limit for most laboratory and field pressure tests, are ≤ 10%. This is within the scatter band of the data for quasi–static loading. Post–test observation of the 6.35–, 19.05–, and 25.4–mm (1/4–, 3/4–, and 1–in.)–long notches indicates large, local, radial bulging deformation around the flaw for all the flaws, but the notches < 25–mm (1–in.)–long also experience significant bulk plastic strain away from the flaw because the nominal stress in these specimens exceeds the yield strength. The general level of plastic deformation diminishes with increasing flaw size, because the larger flaws undergo ligament rupture at lower pressures so that the bulk of the tube away from the flaws remains elastic. Because strain rate effects on plastic deformation are typically much greater than on elastic deformations, the apparent pressurization rate effect observed for the shorter flaws at pressurization rates > 7 MPa/s (1000 psi/s) may be the result of the increased overall plastic deformation in the tubes. No conclusions can be drawn regarding the effect of pressurization rate on unstable burst pressure of initially 100% throughwall notches < 25 mm (1 in.) long because of lack of sufficient data.

Burst pressure results can be affected by pressurization rate, bladder and foil sizes, and difference between as-built and nominal geometries of notches. The testing parameters (bladder and foil size, lubrication) recommended by the current EPRI guidelines were found to give reliable unstable burst pressure and ligament rupture pressure results without any artifact. We found no pressurization rate effect on unstable burst pressure or ligament rupture pressure below 1000 psi/s, which supports the current industry practice of limiting the pressurization rate during in-situ testing to 1.4 MPa/s (200 psi/s). In the past, pressurization rates of up to 14 MPa/s (2000 psi/s) have been used, which may have artificially increased the ligament rupture pressures in those tests by up to 10% for flaws less than 25 mm (1 in.) long.

B Failure maps for complex multiple cracks

Stress corrosion cracks generally consist of multiple cracks separated by ligaments rather than a single, planar crack. Although ligament geometry can be very complex, it can be idealized as being either radial (part–throughwall cracks), purely axial (Type C), or purely circumferential (Type D). During pressurization, the rupture of radial ligaments results in throughwall cracks and the rupture of axial or circumferential ligaments results in a longer crack that may undergo burst at pressures corresponding to normal operation (ΔP_{NO}) or design basis accident condition (ΔP_{MSLB}). Failure maps have been developed to delineate ranges of crack and ligament sizes that could be susceptible to ligament rupture and/or unstable burst due to pressure differences of ΔP_{NO}, ΔP_{MSLB}, $1.4\Delta P_{MSLB}$, or $3\Delta P_{NO}$. The possibility of the presence of 1, 2, 4 or 6 part–throughwall cracks, 80 or 90% deep has been considered. Each map shows the ligament widths and overall crack lengths for a number (2, 4, and 6) of axial part–throughwall cracks with a fixed depth that result in failure at pressure differentials of ΔP_{NO}, ΔP_{MSLB}, $3\Delta P_{NO}$, or $1.4\Delta P_{MSLB}$. The failures could occur due to a number of mechanisms. The failure mechanisms that were considered are the rupture of radial ligament (following which leakage occurs), crack coalescence (i.e., rupture of axial or circumferential ligament), and unstable burst. Each map identifies in terms of crack length and ligament width a region for which failure is predicted not to occur. Outside this no-failure region, the map delineates in terms of crack length and ligament width the regions of various failure mechanisms, e.g., radial ligament rupture, axial/circumferential ligament rupture, and unstable burst.

The maps are based on the ANL radial ligament rupture model for axial part–throughwall cracks, and have been validated over the last several years by tests on specimens with a single EDM notch or two EDM notches separated by axial or circumferential ligament and the well–known unstable burst pressure correlation for a single throughwall crack. Finite element analyses were then conducted to establish numerical models for predicting the coalescence of two axial throughwall cracks separated by axial or circumferential ligament of various widths. The current maps have been generated using typical strength properties of 22 mm (0.875 in.) OD, 1.3 mm (0.05 in.) wall thickness Alloy 600 tubes at 300°C (570°F), and would have to be modified for tubes with different sizes and/or strength properties.

The failure maps have been generated for idealized and regular geometry of cracks. In reality, individual crack lengths and ligament lengths will vary in the same specimen and the ligament geometry can be a mixture of the various idealized geometries considered in this report. Therefore, to use these maps in an actual application, the user has to exercise judgment in determining which map is applicable. Some averaging techniques (e.g., equivalent rectangular crack) will be needed to replace the actual crack geometry (as determined by NDE) with one of the idealized crack geometries considered in this report. For example, crack lengths and ligament lengths could be deliberately chosen to represent an upper or lower bound to the actual case.

C Leak–rate correlation models

Leak rates through stress corrosion cracks (SCCs) in steam generator (SG) tubes in the field are sometimes calculated assuming that the flow inside the tube wall is choked. However, previous tests at ANL have shown that a single–phase orifice discharge model can accurately predict leak rates for flaws with gap dimensions as small as 0.18 mm (0.007 in.). Additional tests have been performed to better establish the range of validity of the orifice flow model. Tests were performed on four stress corrosion cracks (SCCs). Two of the cracks exhibited choked flow, and

two did not. The tightness of the cracks can be described in terms of the length of the flow channel L, approximately the wall thickness, and a hydraulic diameter D, which for a crack is taken as twice the crack opening displacement. Since all the cracks had L/D values of 2–4, this establishes a critical value of L/D for the transition between choked and non–choked flow. This value of L/D is strictly valid only for the value of the subcooling used in the tests, which corresponds to the cold–leg conditions. The value of L/D required to produce choking for hot–leg conditions will be somewhat less.

These results, together with previous work by Amos and Shrock on flow through slits with L/D values from 85–300, have been used to develop a simple leak rate model that accounts for the transition between choked and non–choked flow and the effect of friction in tight cracks with $L/D > 75$. The major uncertainty in applying the model is probably the actual crack geometry. The crack opening area varies as $\sim c^{5.2}$, where c is the half axial crack length and $\sim\theta^{3.5}$, where θ is the half circumferential crack length. Thus, the presence of ligaments could change the leak rate by two orders of magnitude or more. Bounding estimates of crack length will typically grossly overestimate the leak rate, more so for axial cracks than for circumferential cracks.

D Leak rates in restricted areas

Voltage-based alternate repair criteria have been established with regard to outside-diameter stress corrosion cracking of steam generator tubes at tube support plates (TSPs). These criteria rely upon an existing database for free span leak rates from cracks to calculate the total leakage from tubes with indications remaining in service. The database for free-span leakage is utilized because the TSPs could displace laterally during a postulated main steam-line break (MSLB) loading and expose the cracks under the TSPs. To justify leaving higher voltage indications in service than currently allowed, licensees have minimized the displacement of TSPs during transients by expanding a number of tubes above and below the TSPs to effectively lock the TSPs to the tubes. Although this procedure does mitigate the potential for burst and reduce leakage for cracks in the TSP regions, it will not eliminate the potential for increased leakage during postulated MSLBs and severe accidents from such cracks.

The present study seeks to analytically predict flaw opening areas and leak rate increases from a crack, axial or circumferential, under the TSP during postulated MSLB and severe accident conditions. The results show that during postulated MSLB and severe accidents, the controlling leakage areas are the inner diameter (ID) crack opening area for short cracks [≤ 13 mm (0.5 in.)] and the area of the gap between the outer diameter (OD) surface of the tube and the TSP hole/wall for longer cracks. These results are in agreement with Westinghouse test results.

During a postulated MSLB, axial cracks ≤ 13 mm (0.5 in.) in length do not bulge sufficiently to contact the TSP hole/wall, which has a nominal radial clearance of 0.2 mm (0.008 in.). This length is consistent with the maximum crack length of 14 mm (0.55 in.) reported by Westinghouse for a radial clearance of 0.3 mm (0.012 in.) between the tube OD surface and the TSP hole/wall. During postulated severe accidents, the bulging is a function of time, and the tube OD surface is predicted to make contact with the TSP hole/wall at 12,690 s (t=0 represents start of the accident). The contact length increases to 3 mm (0.1 in.) at 13,240 s.

In contrast to the 13 mm (0.5 in.) crack, a 19 mm (0.75 in.) crack does contact the TSP hole/wall over a length of 6 mm (0.25 in.) during postulated MSLB. This result is consistent with

those reported by Westinghouse. During postulated severe accidents the contact length increases to 9 mm (0.35 in.) at 13,600 s.

Circumferential cracks undergo much less radial bulging than axial cracks during postulated MSLB. As a result, the minimum crack length at which contact between the tube OD surface and the TSP hole/wall occurs is much longer, about 180° (corresponding to a length of 35 mm [1.4 in.]). The contact length between the tube OD surface and the TSP hole/wall for a 240° crack is 4 mm (0.15 in.).

In contrast to axial cracks, the circumferential cracks deform very little by creep during the postulated severe accident transient. As a result, the crack opening area and the gap area change very little with time during the postulated severe accident.

At postulated MSLB conditions, the leak rates for 13 and 19 mm (0.5 and 0.75 in.) axial cracks under the TSP are predicted to be 8 and 21 L/min (2 and 5.5 gpm), respectively. These results are in agreement with experimental results from Westinghouse. The leak rates for 90, 180, and 240° circumferential cracks are predicted to be 2, 37, and 78 L/min (0.5, 9.7 and 20.6 gpm), respectively.

At 12,000 s during the postulated severe accident, the leak rates from the 13 and 19 mm (0.5 and 0.75 in.) axial cracks under the TSP are predicted to be 7 and 13 kg/min (3 and 5.8 lb/min). The leak rates from the 90, 180, and 240° circumferential cracks at the same time are predicted to be 11, 22, and 44 kg/min (5, 10, and 20 lb/min), respectively, and they decrease slightly with time.

The predicted leak rates reported here are upper bound rates computed assuming that crevice deposits are absent. Proprietary tests on tube-to-TSP junctions from an operating reactor in France, Dampiere-1, in which deposits were present, showed that leak rates could be reduced by as much as a factor of 1000 compared to those without deposits. Studies on deposits carried out at Chalk River Laboratories showed that the hardness, crushing strength, and consolidation properties of deposits depend strongly on the crevice chemistry. Small changes in crevice chemistry can lead to significant changes in these properties. Analytical predictions of leak rates that would account for the presence of sludge will require data on the mechanical and physical properties of the sludge deposits that are currently not available.

Acknowledgments

The authors thank Dr W. J. Shack of Argonne National Laboratory for helpful discussions. This work is sponsored by the Office of Nuclear Regulatory Research, U.S. Nuclear Regulatory Commission, under Job Code Y–6588; Project Manager E. Reichelt.

This page is intentionally left blank.

List of Acronyms

ANL	Argonne National Laboratory
ARC	Alternate repair criteria
ASME	American Society of Mechanical Engineers
CANDU	Canadian Deuterium Uranium reactor
COA	Crack opening area
COD	Crack opening displacement
CTOD	Crack tip opening displacement
EdF	Electricitè de France
EDM	Electrodischarge machining
EPRI	Electric Power Research Institute
FEA	Finite–element analysis
FWLB	Feed water line break
MA	Mill annealed
MSLB	Main steam line break
NO	Normal operation
NRC	(U.S.) Nuclear Regulatory Commission
OD	Outer diameter
PTW	Part–throughwall
RT	Room temperature
SG	Steam generator
SLB	Steam line break
TT	Thermally treated
TTS	Top of tubesheet
TSP	Tube support plate
TW	Throughwall

This page is intentionally left blank.

List of Symbols

A	Cross–sectional area
a	Crack length
C_D	Dimensionless orifice discharge coefficient
D	Bending stiffness; in Section 3 and 4 denotes a hydraulic diameter
δ	Average opening width of a crack
E, E_{eff}	Young's modulus and effective Young's modulus
h	Wall thickness
J, ΔJ	J–integral and range of J–integral
K, ΔK	Stress intensity factor and range of stress intensity factor
ΔK_J	Equivalent stress intensity factor range determined from ΔJ
K_{ax}	Axial stiffness
L	Span of beam; in Sections 3 and 4 used to denote the length of a flow channel
L/D	Ratio of channel length to hydraulic diameter
m_p	Radial ligament stress magnification factor
$\dot{M}$	Mass flow/unit area through a crack
N	Cycles
Δp	Pressure drop across the tube wall
p_{back}	Pressure acting on outside surface of tube
p_{sat}	Saturation pressure of water at a given temperature
ρ	fluid density
R	Mean radius of tube
ν, ν_{eff}	Poisson's ratio and effective Poisson's ratio

This page is intentionally left blank.

1 Pressurization Rate Effect on Burst Pressure

1.1 Introduction

The flow stress of a typical mill annealed (MA) or thermally treated (TT) Alloy 600 or TT Alloy 690 tube material at temperatures ≤ 300°C is not expected to show a strong dependence on strain rate or stress rate. Consequently, the ligament rupture pressure or unstable burst pressure of a SG tube with a part–throughwall axial crack is not expected to depend significantly on the rate of pressurization at these temperatures. However, Westinghouse conducted a series of room temperature (RT) tests with slow (quasi–static) and fast 14 MPa/s (2000 psi/s) pressurization rates tests that appeared to show a significant effect of the rate of pressurization on the unstable burst pressure. The tests were conducted on tubes with machined part–throughwall notches with a complex shape, the so–called Type 14 notch shown in Fig.1.[1] These notches were machined nominally to the same nominal depth profile (as measured by an eddy current technique) as that of a stress corrosion crack in a SG tube in Arkansas Nuclear One, Unit 2 (ANO–2). Slow (quasi–static) and fast 14 MPa/s (2000 psi/s) pressurization rate tests on these specimens with nominally the same notch appeared to show a significant effect of the rate of pressurization on the unstable burst pressure. Unfortunately, the two types of tests at the two strain rates were conducted following two different test procedures. The slow rate tests were conducted in two steps – first, the specimen was pressurized without bladder and foil until ligament rupture occurred (but not burst); next, a bladder and foil was inserted and the specimen pressurized until unstable burst. The unstable burst pressure during the second step was found to be significantly less than the ligament rupture pressure observed during the initial portion of the test, which indicated that the specimens would have burst unstably during the initial testing if the pump had sufficient flow capacity to maintain pressure after the initial ligament rupture. The fast rate 14 MPa/s (2000 psi/s) tests were conducted with bladder and foil from the beginning of the tests. The average ligament rupture (burst) pressure increased was 30% higher in the tests with a pressurization rate 14 MPa/s (2000 psi/s) than in the quasi–static case. Subsequent analyses suggested that differences in notch profiles between the slow and the fast rate test specimens could account for some of the observed "rate effect" but not all of it.

An earlier series of tests on EDM notch specimens at ANL showed relatively small rate effects. A second series of tests was conducted on a variety of specimen geometries to clearly determine the effect of pressurization rate on burst pressure.

1.2 Factors Influencing Tests to Determine Pressurization Rate Effect

It is known that ligament rupture pressure is more likely to display a pressurization rate effect than unstable burst pressure.[2] In order to be able to predict ligament rupture pressures reliably, we need crack length, the geometry of the crack tip ligament and the flow stress of the material. For a given crack geometry, a true pressurization rate effect on ligament rupture pressure can occur only if the flow stress of the material is a function of strain rate. Flow stress of Alloy 600 (mill-annealed or thermally-treated) at room or normal operating temperature (~300°C) is not expected to vary significantly with the range of strain rates that occur in conventional tensile testing. However, the effective strain rates in narrow crack tip ligaments at high pressurization rates may be significantly higher than what is achievable under conventional tensile testing. The effect of pressurization rate can be masked by spurious factors that need to be understood and

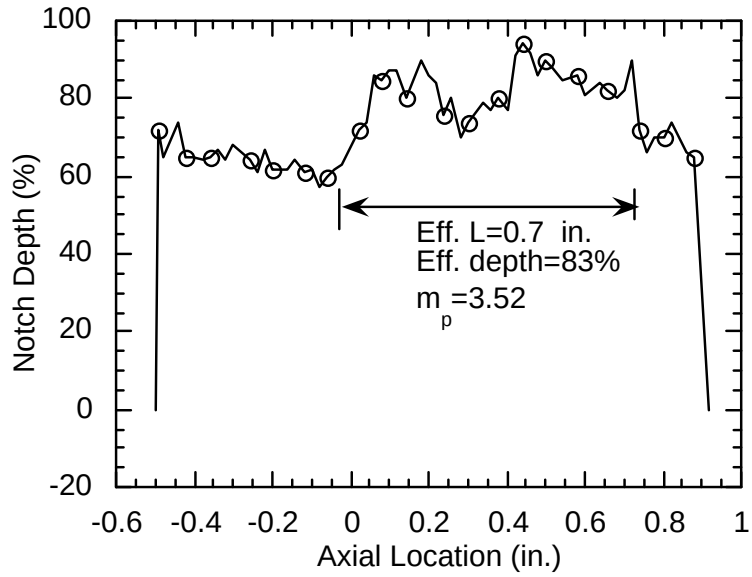

Figure 1.
Notch depth profile for Type 14 specimen. m_p denotes radial ligament stress magnification factor.

accounted for before the true pressurization rate effect on ligament rupture pressure can be established. Key factors other than the effect of strain rate on the flow stress that could affect the pressurization rate effect tests are:

a) Artificial elevation (or reduction) of ligament rupture and burst pressures due to the use of bladder and foil in the test specimens.

b) Specimen-to-specimen variation in as-fabricated ligament geometry and crack length for a given nominal crack geometry.

Tests were conducted with and without bladder and foil to determine the effect of the bladder and foil on the ligament rupture and burst pressure. The typical response time of the pressure transducer used in our RT test facility is 5 ms. The rise time to 2500 psi at a rate of 2000 psi/s is 1.25 s. Because this is much greater than the transducer response time, the response time should have negligible effect on the measured pressurization rate. Also, in order to assess the true effect of pressurization rate, the variability in the test data due to geometric variation from specimen-to-specimen has to be reduced. This was done by first computing the ligament rupture pressures of the specimens with the ANL model[3] using the as-fabricated flaw geometry and the flow stress of the material as determined from conventional tensile tests. If the ligament rupture pressures of the tests conducted with various pressurization rates could be predicted within the 95% confidence limits of the ANL model and showed no systematic bias with respect to the predicted values, we concluded that there was no significant effect of pressurization rate on the ligament rupture pressure. It is more difficult to directly establish a rate effect for SCCs, because the complex SCC flaw geometry varies from specimen to specimen in an arbitrary manner. Thus, any conclusion regarding pressurization rate effect in SCC specimens would have to be drawn on a statistical basis from a relatively large number of tests. Such a determination has not been made under the current study.

1.2.1 Initial Test Series

Test results for the initial series of tests on the effect of bladder and foil on ligament rupture pressure and unstable burst pressure at different pressurization rates are presented in Tables 1

and 2, respectively. The tubes were 22 mm (0.875 in.) in diameter with a 1.3 mm (0.050 in.) wall thickness and had nominal yield and ultimate tensile strengths of 290 and 630 MPa (42 and 91 ksi), respectively. The test facility has the capability to maintain a flow rate of 46 L/min (12 gpm) at 52 MPa (7500 psi). Because these were standard rectangular EDM notches, the as-fabricated geometries of the specimens were close to the nominal values shown in the tables. Table 1 shows that at comparable pressurization rates, the ligament rupture pressures for tests using a bladder but without any foil are close to those using neither bladder nor foil. The 100% TW, 12.7 mm (0.5 in.) long notch tests of Table 2 show no significant effect of foil and bladder thickness on burst pressures. The 100% TW 6.3 mm (0.25 in.) long notch tests in the same table show no significant difference in burst pressures for tests conducted with or without foil and bladder. Similarly, no systematic differences were detected in the burst pressures for tests using bladder with a 0.13 mm (0.005 in.) brass foil or with bladder but no foil. Although the comparison testing with and without bladder and foil has not been exhaustive, Westinghouse has also concluded that the use of bladder and foil of the same sizes as used here does not affect the ligament rupture or burst pressure significantly.[a]

Table 1 Ligament rupture pressures for < 25 mm (1 in.) long, part–throughwall rectangular EDM flaws with and without bladder

Flaw Length mm (in.)	Flaw Depth (%)	Foil	Bladder	Pressurization Rate MPa/s (psi/s)	Ligament Rupture Pressure MPa (psi)
19.0 (0.75)	80	No	No	Quasi–static	21.4 (3100)
				13.8 (2000)	24.1 (3500)
				48.3 (7000)	26.2(3800)
6.3 (0.25)	90	No	No	Quasi–static	30.0 (4350)
				5.2 (750)	28.3(4100)
				22.0 (3200)	33.8(4900)
12.7 (0.5)	60	No	No	13.8 (2000)	40.7 (5900)[a]
			3/32 in. Tygon	13.8 (2000)	41.4 (6000)[a]
6.3 (0.25)	80	No	No	Quasi–static	37.9 (5500)
			3/32 in. Tygon	20.7 (3000)	43.1 (6250)[a]
6.3 (0.25)	60	No	No	13.8 (2000)	49.60(7200)
			3/32 in. Tygon	20.7 (3000)	47.60(6900)[a]

[a] Specimen burst with fishmouth flaw opening

[a] Private Communication R. Keating of Westinghouse Corp. to S. Majumdar, Argonne National Laboratory, 2000.

Table 2 Unstable burst pressures (Stage 2) for < 25 mm (1 in.) long, part–throughwall and throughwall rectangular EDM flaws with and without bladder and foil.

Flaw Length mm (in.)	Flaw Initial Depth (%)	Foil	Bladder	Pressurization Rate MPa/s (psi/s)	Unstable Burst Pressure MPa (psi)[a]
12.7 (0.5)	100	Standard 0.005 in.	3/32 in. Tygon	13.8 (2000)	30.3 (4400)
		Standard 0.005 in.	1/8 in. Tygon		29.6 (4300)
		Standard 0.005 in.	1/8 in. Tygon		30.0 (4350)
		Oversize 0.005 in.	1/8 in. Tygon		30.7 (4450)
6.3 (0.25)	90	No	No	22.1 (3200)	44.8 (6500)[b]
		No	1/8 in. Tygon	4.80(700)	44.8 (6500)
		Standard 0.005 in.	1/8 in. Tygon	6.2 (900)	41.4 (6000)
6.3 (0.25)	90	No	No	Quasi–static	42.7 (6200)[b]
				5.2 (750)	44.1 (6400)[b]
				22.0 (3200)	44.8 (6500)[b]

[a] Nominal burst pressure of a 13 mm (0.5 in.), 100% throughwall notch is 30 MPa (4400 psi)
[b] Specimen did not burst with fishmouth flaw opening

1.3 Test Specimens for the Second Series

Four types of EDM notched specimens, shown in Figs 2–3, were fabricated from 0.875 in. (22 mm-)-diameter MA Alloy 600 tubes for additional pressurization rate effect tests. The tubes had nominal yield and ultimate tensile strengths of 290 and 630 MPa (42 and 91 ksi), respectively. The total notch length of each specimen was fixed nominally at 1 in. (25 mm). An additional series of rectangular EDM notches with shorter notch lengths were tested to determine if pressurization rate effects are more pronounced in such specimens. Also, two tests were conducted on specimens with SCC.

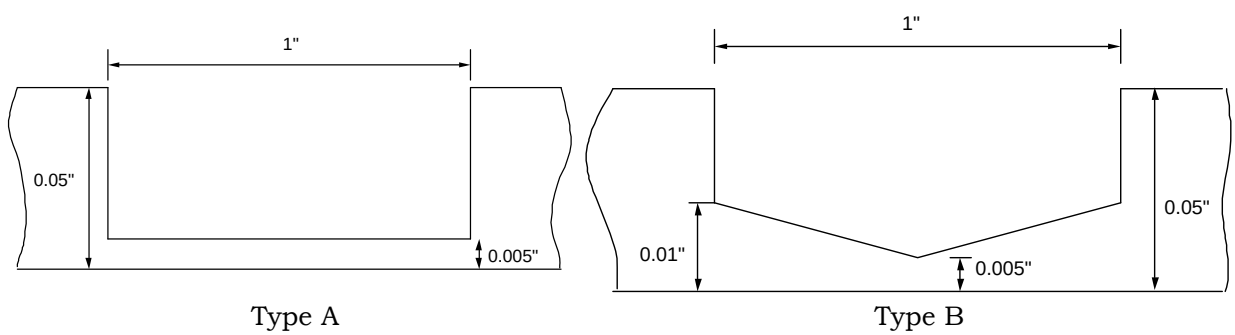

Figure 2. Type A: single rectangular notch and Type B: single trapezoidal notch.

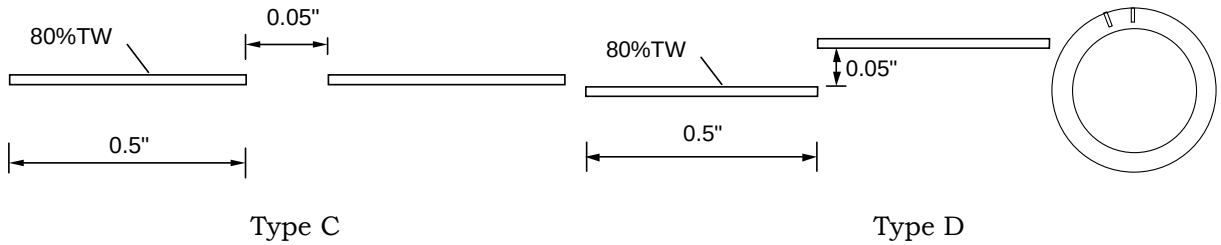

Figure 3. Type C: 2–collinear notches (axial ligament) and Type D: 2–offset notches (circumferential ligament)

1.4 Test Procedure for the Second Series

Four pressurization rates were used: quasi–static (stepwise pressure increases with intermittent hold), 7 MPa/s (1000 psi/s), 14 MPa/s (2000 psi/s), 41 MPa/s (6000 psi/s), and, for some tests, >70 MPa/s (>10,000 psi/s). The quasi–static tests were used as controls/references.

To minimize the effects of bladder and foil on the results, all of the specimens were tested in two stages. First, the specimens were pressurized without any bladder or foil at a controlled pressurization rate to ligament rupture. Pressurization then was continued until the pump ran out of flow or pressure capability. For the specimens that did not undergo unstable burst, a bladder and foil was inserted inside the specimens, and the specimens were pressurized at the desired rate until unstable burst occurred. Because all the flaws after ligament rupture were 25.4–mm (1–in.) long, they were expected to exhibit nominally the same burst pressure, and hence only a representative number were tested to unstable burst. The bladder used was a hard Tygon tubing with a 3.2–mm (1/8–in)–thick wall and a diameter slightly smaller than the specimen ID. Brass foils of thickness 0.13 mm (0.005 in.) were used, and they extended 6.35 mm (0.25 in.) beyond the flaw extremities. The foil and bladder were sprayed with a lubricant to reduce friction between the foil and SG tube.

1.5 Test Results for the Second Series

1.5.1 Tests on 25 mm (1 in.) Long EDM Flaws

Table 3 summarizes the data from the ligament rupture tests on rectangular and non-rectangular flaws 25 mm (1 in.) long. The raw data are somewhat misleading because the as–received EDM flaws varied somewhat from the specified dimensions which has a significant influence on ligament rupture pressure. As noted previously, these results have to be compared with predictions of ligament rupture pressures based on the as–fabricated flaw geometry before the effect of pressurization rate can be assessed.

Results from the unstable burst testing are summarized in Table 4. All of the unstable burst pressures varied between 14–16 MPa (2000–2300 psi), as expected because all of the notches had an overall length of 25 mm (1 in.). Consequently, the rest of the specimens were not tested.

Table 3 EDM flaw ligament rupture pressure (Stage 1) for four flaw types (Types A, B, C, and D in Figs. 2–3) and five different pressurization rates.

Pressurization Rate, MPa/s (psi/s)	Observed Failure Pressures, MPa (psi) [Specimen No.] For Flaw Types Indicated in Figs 2–3			
	A	B	C	D
Stage 1 Testing; Radial Ligament Rupture (no foil or bladder)				
Quasi–steady–state	9.1 (1320) [OM201]	13.1 (1900) [OM207]	23.9 (3460) [OM214[b]]	27.6 (4000) [OM219[c]] 21.7 (3150) [OM223[c]]
7 (1000)	12.5 (1815) [OM202] 11.5 (1675) [OM204]	10.6 (1535) [OM224]	24.4 (3540) [OM215[b]]	22.5 (3264) [OM220[c]]
14 (2000)	9.1 (1325) [OM203]	12.4 (1800) [OM210]	22.0 (3190) [OM216[b]]	24.1 (3500) [OM222[c]]
41 (6000)	11.7 (1690) [OM205]	13.4 (1950) [OM211]	21.6 (3135) (OM217[b]]	24.3 (3520) [OM225[c]]
> 69 (>10,000)	13.0 (1885) [OM206]	51.0 (7400) [OM209[a]] 12.9 (1875) [OM212]	23.7 (3440) [OM213[b]] 23.1 (3350) [OM218[b]]	–

[a]Flaw much shallower than specified dimensions.
[b] Both radial and axial ligaments ruptured.
[c] Both radial and circumferential ligaments ruptured.

Table 4 EDM flaw unstable burst pressure (Stage 2) for four flaw types (Types A, B, C, and D in Figs. 2–3) and five different pressurization rates.

Pressurization Rate, MPa/s (psi/s)	Observed Failure Pressures, MPa (psi) [Specimen No.] For Flaw Types Indicated in Figs 2–3			
	A	B	C	D
Stage 2 Testing; Unstable Burst (with foil and bladder)				
7 (1000)	–	–	14.1 (2050) [OM215]	–
14 (2000)	15.8 (2295) [OM203]	–	14.3 (2075) [OM216]	–
41 (6000)	14.7 (2130) [OM205]	–	13.9 (2020) [OM217]	–
> 69 (>10,000)	15.6 (2265) [OM206]	–	15.0 (2175) [OM218]	–

1.5.2 Tests on Short EDM Flaws

Three 6.35–mm– (1/4–in.)–long, 90% TW flaws, OM232, OM234, and OM250, were tested at a nominal pressurization rate of 41 MPa/s (6000 psi/s). The observed ligament rupture pressures are 40.0, 40.7, and 40.1 MPa (5800, 5900, and 5810 psi), respectively.

Two 19.05–mm (3/4–in.)–long, 80% TW flaws OM235 and OM236, tested at a nominal rate of 50.3 MPa/s (7300 psi/s), yielded ligament rupture pressures of 24.8 and 26.8 MPa (3600 and 3885 psi), respectively.

1.5.3 Tests on Stress Corrosion Cracks

Limited tests at various pressurization rates were initiated on 22.2–mm (7/8–in.)–diameter tubes containing laboratory–produced ODSCC axial flaws of nominally 12.7– and 19.05–mm (1/2– and 3/4–in.) length and ≥80% TW. The two pressure tests conducted on SCC specimens to date were inconclusive because, unlike EDM notches, no abrupt ligament rupture event occurred in these tests.

1.6 Analysis of Test Results

1.6.1 Predicted Failure Pressures

As noted, to minimize the uncertainties due to specimen-to-specimen variation in flaw geometry, the observed ligament rupture pressures should be compared with ligament rupture pressures predicted using the as-fabricated geometry. For the tests on the 25 mm (1 in.) flaws, this comparison is shown in Fig. 4 where the predicted values are based on a constant rate-independent yield stress=290 MPa (41.6 ksi), a rate-independent constant ultimate tensile strength = 630 MPa (91.4 ksi), and a flow stress factor k=0.55. The predicted test ligament rupture pressures are within the ± 95% confidence limits of the test predicted ligament rupture pressures and no strong bias about the predicted value is observed. Thus, there is no statistical evidence of a systematic pressurization rate effect on the ligament rupture pressure for rates up to 14 MPa/s (2 ksi/s) for 25 mm (1 in.) long notches.

For a 25 mm (1 in.) throughwall crack, the predicted unstable burst pressure is 17 MPa (2.4 ksi), which is within 10% of all the observed unstable burst pressures. Thus, there is no significant pressurization rate effect on the unstable burst pressures for rates up to 14 MPa/s (2 ksi/s) for 25 mm (1 in.) TW flaws.

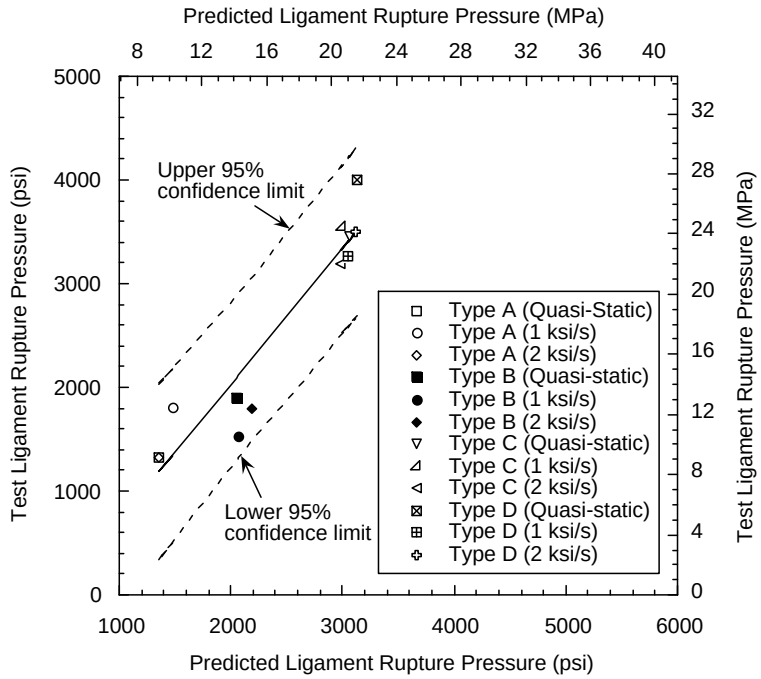

Figure 4.
Predicted vs. observed ligament rupture pressure for quasi–static to 14 MPa /s (2 ksi/s) tests.

The ligament rupture pressure data for flaws < 25 mm (1 in.) are plotted in Figs. 5a as a function of pressurization rate. Figs. 5a also includes Type 14 test data from Westinghouse.[1] The Type 14 data appear to exhibit a larger pressurization rate effect than the ANL tests; 30% increase for the Type 14 specimens compared to 10% increase for the ANL tests due to an increase in pressurization rate from quasi–static to 13.8 MPa/s (2 ksi/s).

Much of the variability in the ligament rupture data (particularly the Type 14 data) can be traced to the variability in the as–built notch geometry from the nominal geometry.[1] As mentioned earlier, a better estimate of the true effect of pressurization rate can be obtained by normalizing the test results by the predicted ligament rupture pressures using the as–fabricated geometry of the notches and the ANL ligament rupture model. The variation of the normalized ligament rupture pressures with pressurization rate is shown in Fig. 5b. The scatter band at 138 kPa/s [20 psi/s (quasi-static)] is estimated from a database on ligament rupture pressure on rectangular EDM notches conducted at ANL.[2-4] Note that most of the type 14 data fall within the ANL data scatter. The plot suggests no significant pressurization rate effect between quasi–static and 7 MPa/s (1 ksi/s). Beyond 7 MPa/s (1 ksi/s), there is a slight increase in the normalized ligament rupture pressure with pressurization rate that varies approximately as pressurization rate raised to an exponent 0.129. The shorter notches tend to show a slightly larger rate effect than the longer notches. However, if the pressurization rate is limited to 13.8 MPa/s (2 ksi/s), the increase in ligament rupture pressure compared to quasi–static is about 10%, which is within the scatter band of the quasi–static test data.

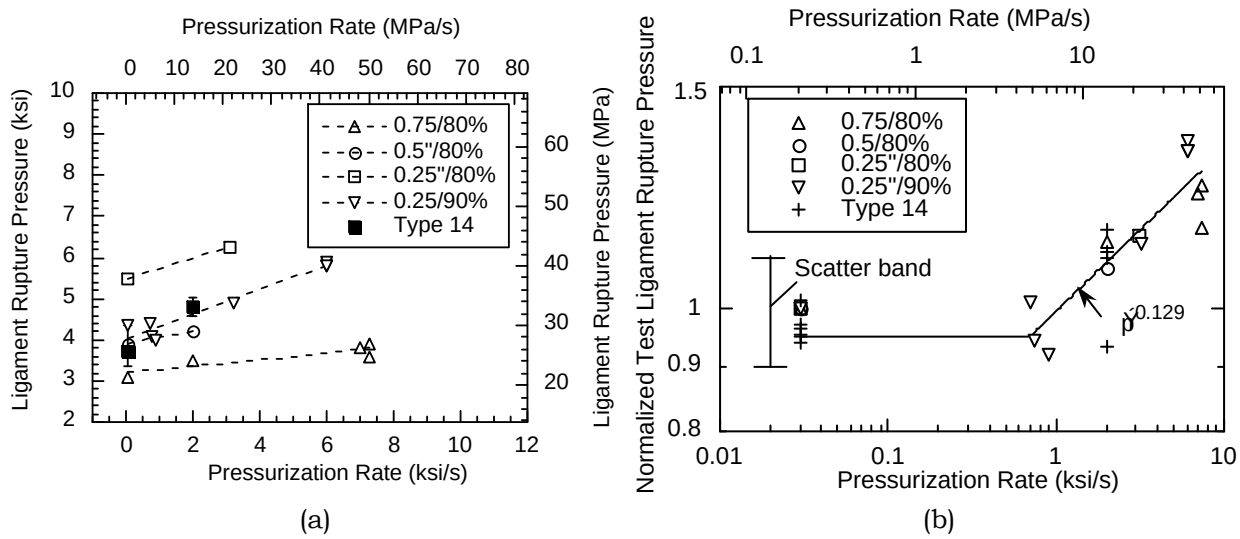

Figure 5. Variation of (a) test ligament rupture pressures and (b) normalized test ligament rupture pressures with pressurization rate.

1.6.2 Post-Test Observations of Specimens

Post–test observations of the 6.35–, 19.05–, and 25.4–mm (1/4–, 3/4–, and 1–in.)–long notches indicated large radial bulging deformation occurring locally around the flaw for all the flaws. However, the < 25–mm (1–in.)–long flaws also experience significant bulk plastic strain away from the flaw location because the nominal stress in these specimens exceeded the yield strength. The general level of plastic deformation diminishes with increasing flaw size, because the larger flaws undergo ligament rupture at lower pressures in a regime where the bulk of the tube away from the flaws remains elastic. The observed pressurization rate effect for the shorter flaws may be a result of a strain rate effects associated with the more extensive plastic deformation.

1.7 Conclusions

The 25 mm (1 in.) long rectangular as well as trapezoidal notches and two notches separated by axial and circumferential ligament do not show any pressurization rate effect on the ligament rupture or unstable burst pressure. Rectangular notches < 25 mm (1 in.) long show a small pressurization rate effect on ligament rupture pressure for rates > 7 MPa/s (1000 psi/s), with shorter notches experiencing a slightly greater rate effect than longer notches. However the increase in ligament rupture pressure at 13.8 MPa/s (2000 psi/s), which is the upper limit for most laboratory and field pressure tests[5], compared to quasi–static loading is only 10%, which is within the scatter of the data for quasi–static loading. Because of lack of sufficient data, no conclusions can be drawn regarding the effect of pressurization rate on unstable burst pressure of initially 100% throughwall notches < 25 mm (1 in.) long. Burst tests on initially 100% throughwall notches < 25 mm (1 in.) long are needed.

The pressurization rate effect observed in the specimens with shorter part-throughwall flaws may be associated with the significant plastic deformation in the bulk of the tubes away from the flaws. Plastic deformation is more localized in specimens with longer flaws.

The use of tygon bladder ≤ 3 mm (1/8 in.) thick, with or without standard size 0.13-mm (0.005 in.) thick brass foils, does not influence the ligament rupture or unstable burst pressures of part-throughwall notches. For initially throughwall notches, the change of tygon bladder thickness from 2 to 3 mm (3/32 to 1/8 in.) does not affect the unstable burst pressure if it is used together with standard size 0.13-mm (0.005 in.) thick brass foils.

Because of the difficulty of controlling the geometry of actual SCCs, pressurization rate effects in SCC specimens would have to be investigated by testing a large number of specimens with "similar" SCCs at several pressurization rates and comparing the pressure vs. leak rate data on a statistical basis. Such a program is not planned.

Although the current series of tests have been conducted at RT on MA Alloy 600 tubes, the conclusions relative to pressurization rate effect are expected to be applicable to TT tubes at RT as well as at operating temperatures (~300°C). The plastic deformation mechanisms and behavior of the MA and TT materials are similar and strain rate effects due to thermal creep are not expected to be significant at ≤ 300°C. The conclusions should also be applicable to TT Alloy 690 for the same reason. The grain boundary carbides associated with TT materials may have significant effects on the long–term deformation of grain boundaries, but the failure processes of interest involve primarily plastic deformations in the bulk of the grain.

2 Failure Maps for Complex Multiple Cracks

2.1 Introduction

Stress corrosion cracks generally consist of multiple cracks separated by ligaments (Fig. 6). Although ligament geometry can, in general, be very complex, it can be idealized as being either radial (part–throughwall cracks, Fig. 7), purely axial (Type C in Fig. 8), or purely circumferential (Type D or Type E in Fig. 8). Of all the three types of ligaments, cracks separated by type E ligaments show little or no interaction, i.e., they essentially behave as single cracks independent of ligament length.[2] Therefore, Type E ligament will not be considered separately in this report. During pressurization, the rupture of radial ligaments leads to leaking throughwall cracks and the rupture of axial (Type C) or circumferential (Type D) ligaments leads to joining of cracks, resulting in a longer crack that could undergo burst due to pressure during normal operation (ΔP_{NO}) or design basis accident condition (ΔP_{MSLB}). The purpose of this study is to develop failure maps that delineate ranges of ligament and crack sizes that could be susceptible to ligament rupture and/or unstable burst due to pressure differences of ΔP_{NO}, ΔP_{MSLB}, $1.4\Delta P_{MSLB}$, and $3\Delta P_{NO}$. For the purpose of this study, we have used ΔP_{NO} = 10 MPa (1.5 ksi) and ΔP_{MSLB} = 18 MPa (2.6 ksi). Such failure maps are intended to be used as a tool for identifying cracks that would require more detailed investigation during in-service inspection and screening out those for which interactions are unimportant. They are also helpful in providing a quantitative understanding of the important effect remaining ligaments have on the burst strength of flawed tubes. The maps consider the possibility of the presence of 1, 2, 4 and 6 part–throughwall cracks, 80 and 90% deep. Although field data show cracks that are generally shallower, for a much shallower crack to fail at any of the four critical pressures considered here, the crack would have to be very long.

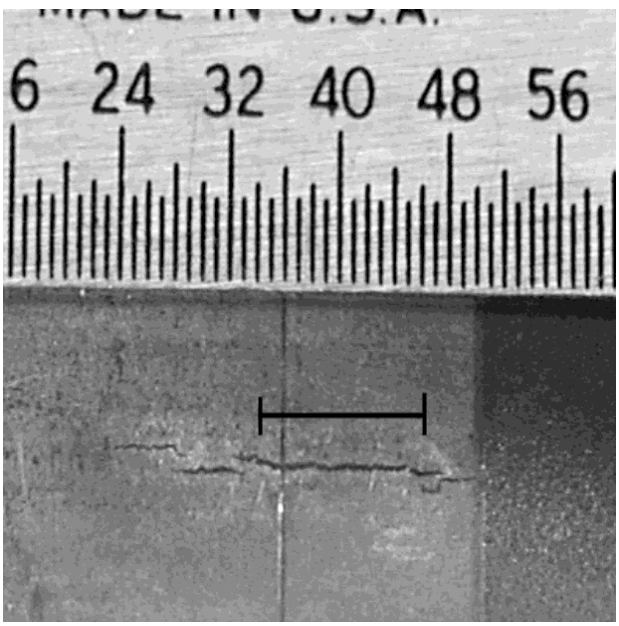

Figure 6.
Typical stress corrosion crack geometry.

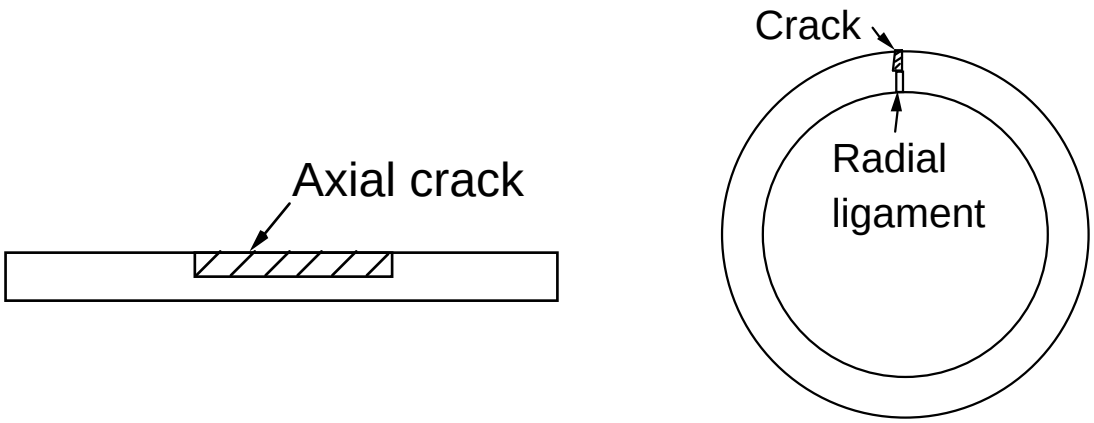

Figure 7. Idealized single part–throughwall axial crack with a radial ligament.

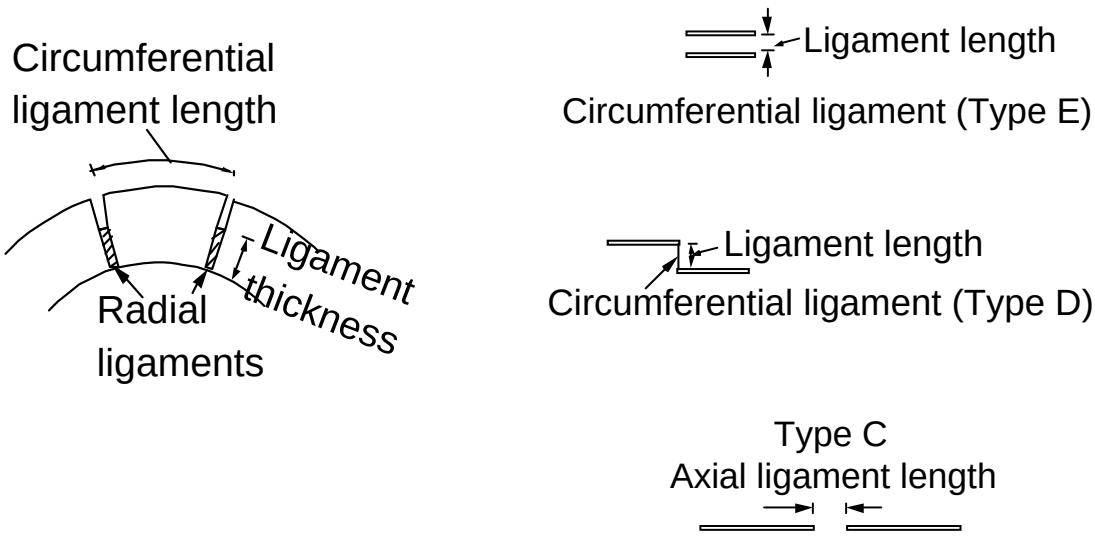

Figure 8. Two idealized part–throughwall axial cracks each with a radial ligament at the through-thickness crack tip and separated from each other by either an axial (Type C) or a circumferential (Type D or Type E) ligament.

2.2 Background Analysis and Tests

2.2.1 Throughwall Axial Cracks

Detailed finite–element analyses (FEA) and tests on specimens containing two notches were conducted under ISG–TIP–2 and reported in Ref. 4. Two types of throughwall (TW) notches were analyzed. First, in type C specimens (Fig. 9a), two axial notches, 0.19–mm (0.0075–in.) wide, were collinear with an axial ligament separating the two. Second, in type D specimens (Fig. 9b), the two axial notches, 0.19–mm (0.0075–in.) wide, were offset in the circumferential direction with the right tip of the first notch aligning with the left tip of the second notch. Finite element analyses were conducted for a type C specimen with two 6–mm (0.25–in.) long TW notches separated by a 0.25–mm (0.01–in.) long axial ligament at RT. The engineering and true stress–strain curves of the as–received material at RT are shown in Fig. 10. The problem was analyzed by ANSYS as well as ABAQUS using finite deformation theory (true stress–strain curve). Plots of the average thickness vs. pressure (Fig. 11) shows that rapid necking (the last step in the analysis beyond which numerical instability develops) in the ligament is predicted to occur at a pressure of 17 MPa (2.5 ksi) by ANSYS and 19.5 MPa (2.8 ksi) by ABAQUS, in reasonable agreement with the test result. Tests were also conducted on specimens with two TW axial notches (each either 6 or 13–mm long) in the type D configuration (circumferential ligament). The ligament rupture pressures predicted by FEA are compared with the observed ligament rupture pressures in Fig. 12. The two dashed lines in Fig. 12 represent the unstable burst pressures corresponding to single TW notches (with twice the individual notch length) that result after the coalescence of the two notches following circumferential ligament rupture. Specimens whose ligament rupture pressures lie above the dashed lines experience unstable burst immediately after ligament rupture, whereas those below the corresponding dashed lines remain stable with a single larger notch.

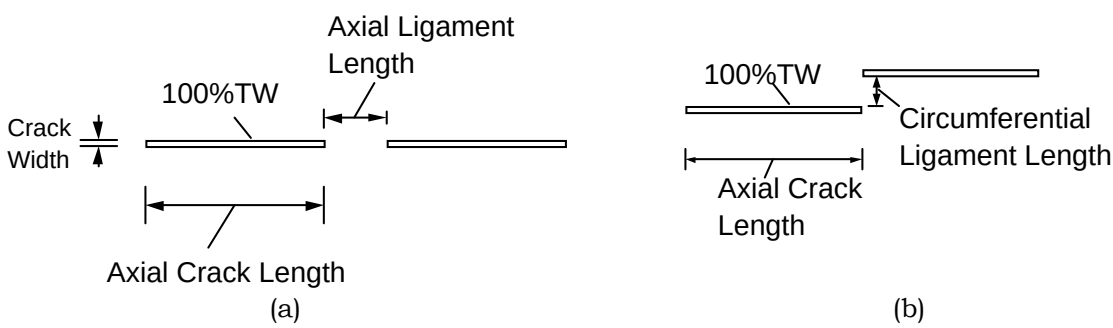

Figure 9. Two-TW axial notches separated by (a) an axial ligament (Type C) and (b) a circumferential ligament (Type D).

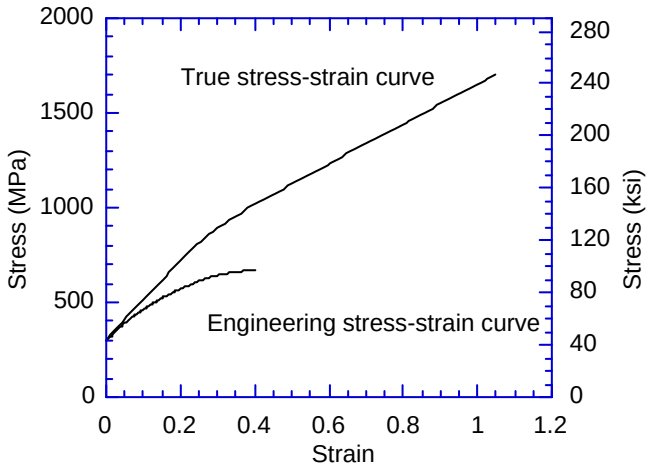

Figure 10.
Engineering and true stress–strain curves of Alloy 600 used for finite element analysis.

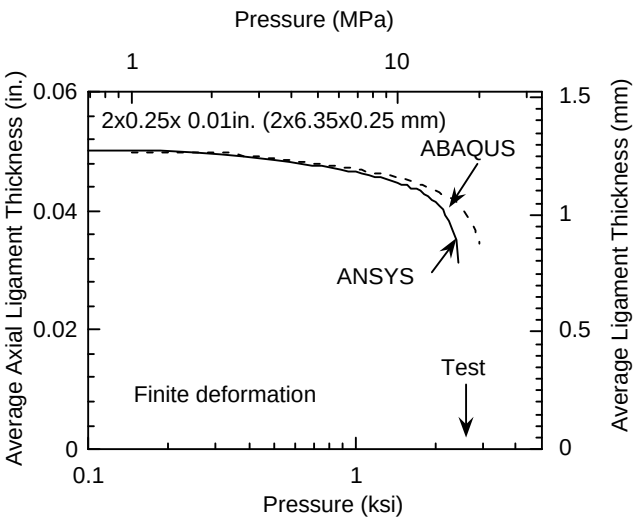

Figure 11.
Calculated variation of average inter–notch axial ligament thickness with pressure using finite deformation analyses by ANSYS and ABAQUS for two 6–mm (0.25–in.) long axial cracks separated by a 0.25–mm (0.01–in.) long axial ligament (Type C).

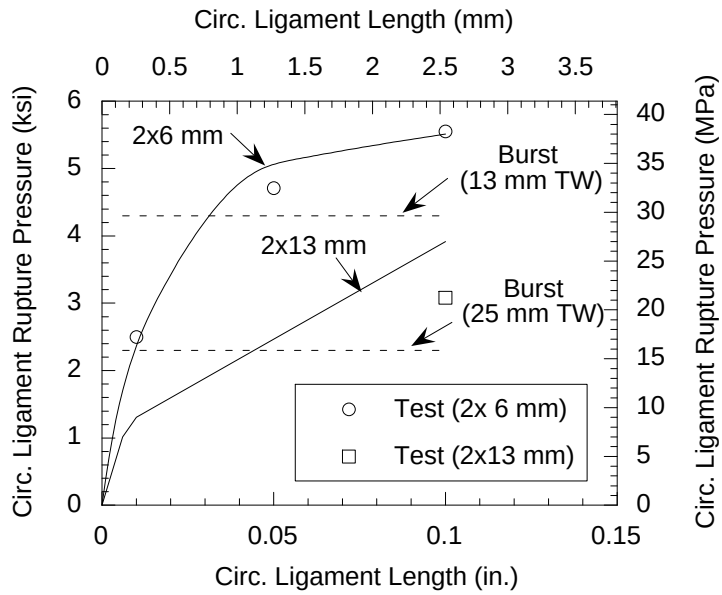

Figure 12.
Predicted (by FEA, line) vs. observed (symbols) variation of ligament rupture pressure with circumferential ligament length for type D specimens having two 6–and 13–mm long TW notches.

2.2.2 Part–Throughwall Axial Cracks

All the tubes considered in this section had a diameter of 22–mm (0.875 in.) and nominal yield and ultimate tensile strengths of 300 and 675 MPa (43 and 98 ksi), respectively. We used the equivalent rectangular crack method[4] to predict the through–thickness (radial) ligament rupture for two PTW cracks separated by either an axial (type C) or circumferential (type D) full–thickness ligament (see Figs. 7-8 for ligament definitions). The radial ligament rupture pressures for tubes with two axial notches, type C (axial ligament) and type D (circumferential ligament), were calculated by the equivalent rectangular approach for various notch lengths and inter–notch ligament lengths. Tests were conducted in the ANL High Pressure Test Facility on specimens without bladders and were interrupted after the through–thickness radial ligament ruptured, as evidenced by onset of leakage. The predicted vs. experimental ligament rupture pressures given in Figs. 13a–b for two 6– and 13–mm long notches, respectively, indicate that the equivalent rectangular crack approach can predict the through–thickness radial ligament rupture pressures reasonably well. Unless otherwise noted in the figures, in all of the tests, the axial and circumferential ligaments were also ruptured following radial ligament rupture. The rupture/non-rupture of the circumferential ligaments in Figs. 13a–b can be predicted from the circumferential ligament rupture pressure data presented in Fig. 12 depending on whether the failure pressures in Figs. 13a-b lie above or below the failure pressures for the corresponding crack and ligament lengths in Fig. 12. The two dashed lines in Fig. 13b, representing the radial ligament rupture pressures of single 13 and 25 mm (0.5 and 1 in.) long, 80%TW notches, provide limits within which the radial ligament rupture pressures for the 2 x 13 mm (2 x 0.5 in.) long, 80%TW notches must lie.

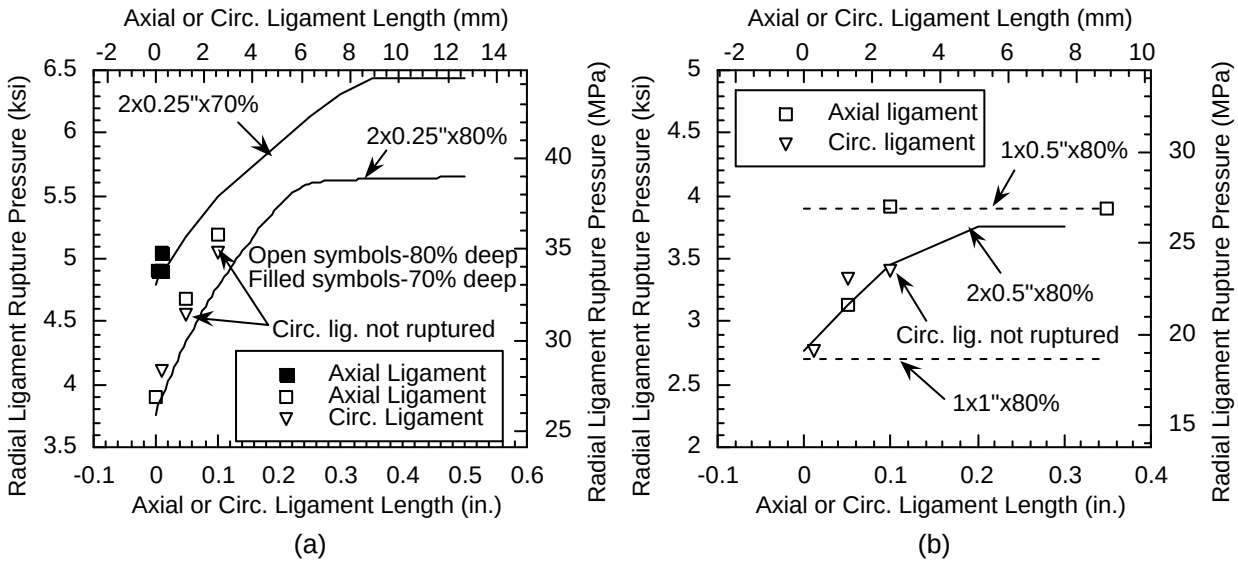

Figure 13. Predicted (line) and observed (symbols) radial through–thickness ligament rupture pressures vs. axial or circumferential ligament lengths for two PTW EDM notches (a) 6–mm (0.25–in.) and (b) 13–mm (0.5–in.) long.

2.3 Parametric Analyses for Axial Throughwall Cracks

To generate the failure maps for the various pressure loading, we ran a series of analyses with two, four and six axial throughwall cracks (Figs. 14a–b and 15a–b) to develop the pressures required for axial and circumferential ligament rupture (i.e., crack coalescence). Note that, in contrast to the convention followed so far, the "crack length" is defined as the total tip-to-tip length including all of the cracks and ligament lengths. "Ligament length" continues to refer the length of an individual ligament between two cracks. For a given overall crack length, individual cracks are assumed to all have the same length and individual ligaments are assumed to all have the same length. Results from these analyses for four overall crack lengths and ligament lengths are plotted (as symbols) in Fig. 16 for the case of two cracks separated by an axial ligament. For interpolation and limited extrapolation of the FEA results to different ligament lengths, the ligament rupture pressure (σ_{lig}) for each crack length was fitted by a polynomial function of the ligament lengths (l_w) of the form:

$$\sigma_{lig} = a_1 l_w + a_2 l_w^2 \tag{1}$$

The curve fits were constrained to ensure that for a given crack length, as the ligament length approached the crack length/the number of ligaments, i.e., as the lengths of the individual cracks approached zero, the rupture pressure can not exceed the burst pressure of an unflawed tube. The variation of the parameters a_1 and a_2 with crack length was determined by fitting the results for the four crack lengths by power law fits as shown in Figs. 17a–b, respectively. The rupture pressure vs. ligament length plot for the case of four axial cracks separated by axial ligaments is given in Fig. 18 and plots for the corresponding fitting parameters a_1 and a_2 are given in Figs. 19a–b, respectively. The rupture pressure vs. ligament length plot for the case of six axial cracks separated by axial ligaments is given in Fig. 20 and plots for the corresponding fitting parameters a_1 and a_2 are given in Figs. 21a–b, respectively.

(a) (b)

Figure 14. Specimens with two throughwall axial cracks, separated by (a) an axial ligament (Type C) and (b) a circumferential ligament (Type D), analyzed by FEA.

(a) (b)

Figure 15. Specimens with (a) four and (b) six axial throughwall cracks analyzed by FEA.

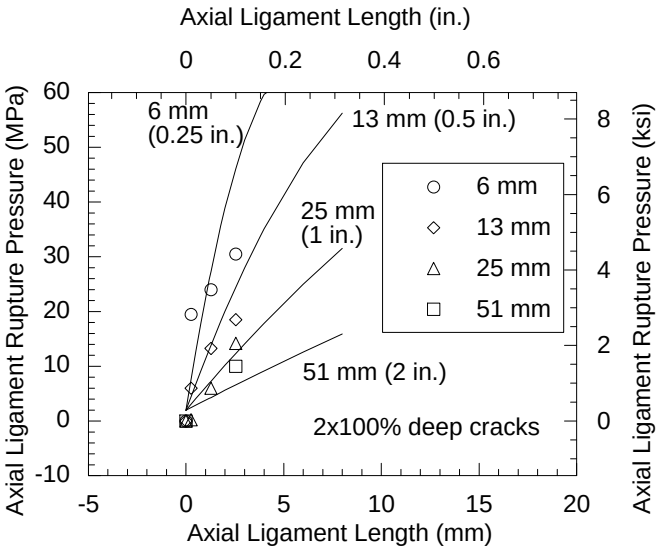

Figure 16.
Axial ligament rupture pressure for two throughwall axial cracks separated by an axial ligament. Symbols represent FEA results and lines are polynomial fits of the FEA results to Eq. 1.

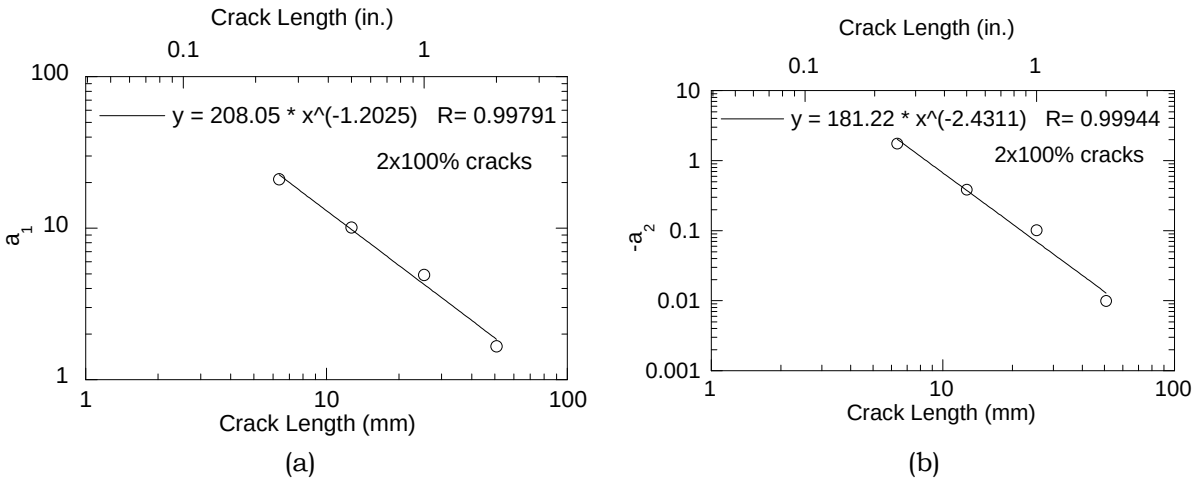

(a) (b)

Figure 17. Variation of fitting parameters (a) a_1 and (b) a_2 with crack length (in mm) for specimens with two throughwall axial cracks separated by an axial ligament. Symbols denote values of fitting parameters for the four crack lengths shown in Fig. 16 to Eq. 1 and lines are power-law fits for the fitting parameters as functions of crack length.

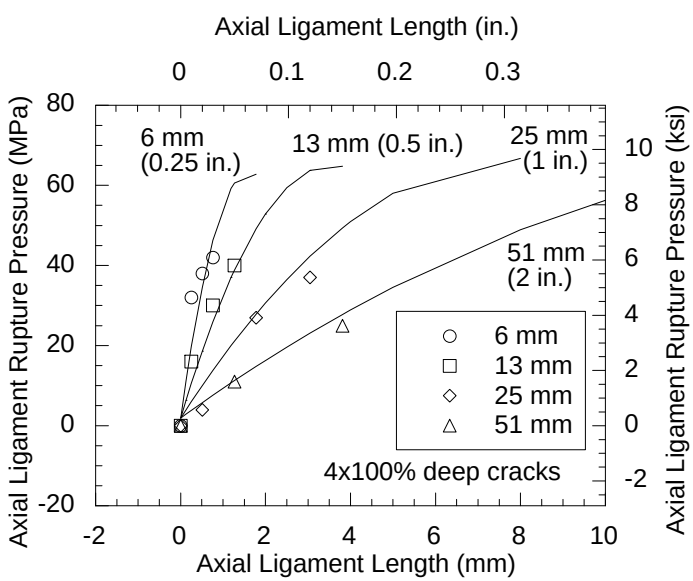

Figure 18.
Axial ligament rupture pressure for four throughwall axial cracks separated by three equally long axial ligaments. Symbols represent FEA results and lines are polynomial fits of the FEA results to Eq. 1.

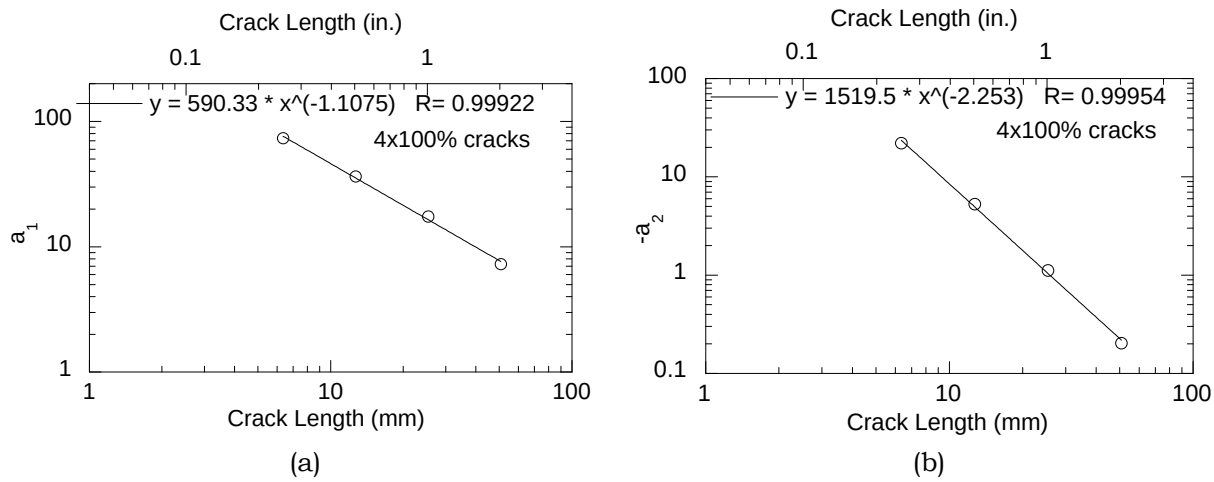

(a) (b)

Figure 19. Variation of fitting parameters (a) a_1 and (b) a_2 with crack length (in mm) for specimens with four throughwall axial cracks separated by three axial ligaments. Symbols denote values of fitting parameters for the four crack lengths for the four crack lengths shown in Fig. 18 to Eq. 1 and lines are power-law fits for the fitting parameters as functions of crack length.

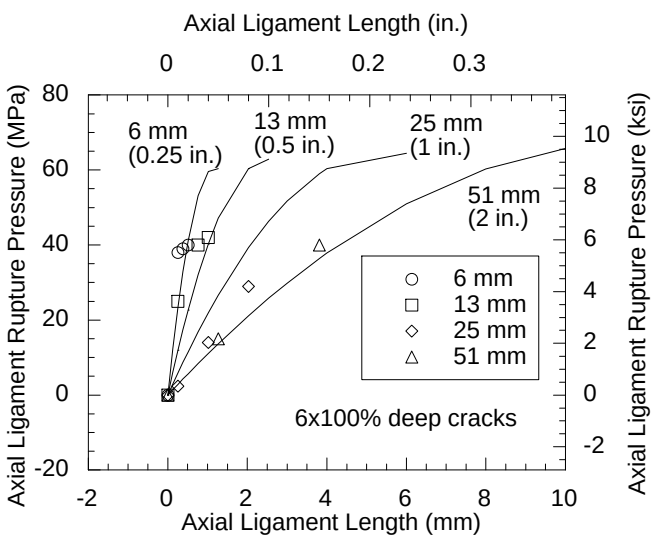

Figure 20.
Axial ligament rupture pressure for six throughwall axial cracks separated by five equally long axial ligaments. Symbols represent FEA results and lines are polynomial fits of the FEA results to Eq. 1.

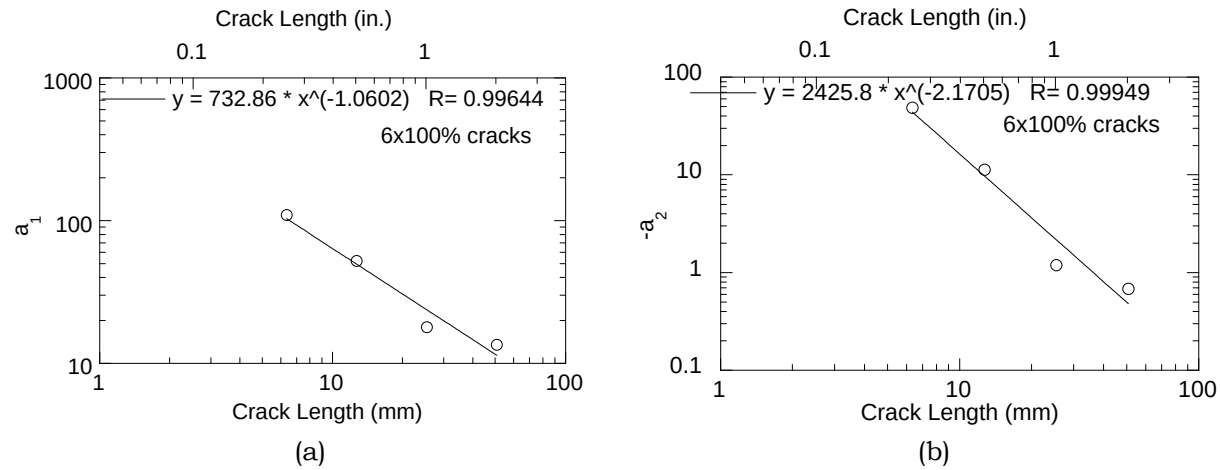

Figure 21. Variation of fitting parameters (a) a_1 and (b) a_2 with crack length for specimens with six throughwall axial cracks separated by five axial ligaments. Symbols denote values of fitting parameters for the four crack lengths for the four crack lengths shown in Fig. 20 to Eq. 1 and lines are power-law fits for the fitting parameters as functions of crack length.

The rupture pressure curve for the case of two axial cracks separated by a circumferential ligament is shown in Fig. 22. In fitting the rupture data, the fit must be constrained to ensure that as the ligament length increased, the rupture pressure can not exceed the unstable burst pressure of a single crack (i.e., half the crack length). However, a simple polynomial of the type used for the case of the axial ligament did not fit the data satisfactorily. A more satisfactory result was obtained by expressing $\log(\sigma_{lig})$ in terms of a polynomial in $\log(l_w)$ of the form:

$$\log(\sigma_{lig}) = M_0 + M_1 \log(l_w) + M_2[\log(l_w)]^2 \tag{2}$$

The variation of the parameters M_0, M_1 and M_2 with total crack length is shown in Fig. 23.

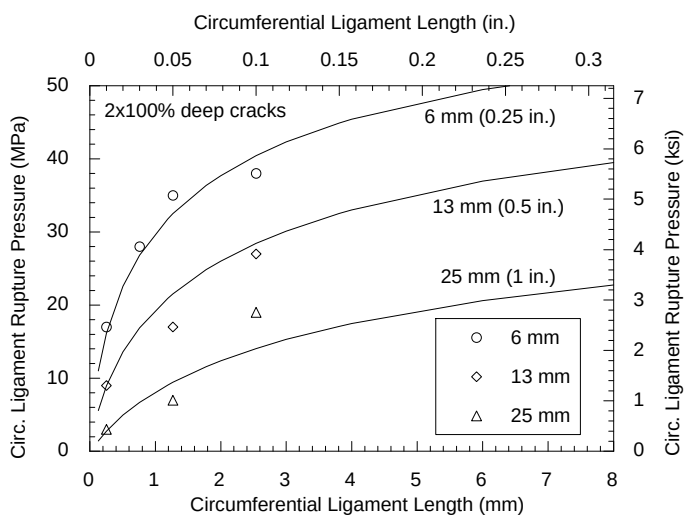

Figure 22.
Circumferential ligament rupture pressure for two throughwall axial cracks separated by a circumferential ligament. Symbols represent FEA results and lines are log-polynomial fits of the FEA results to Eq. 2.

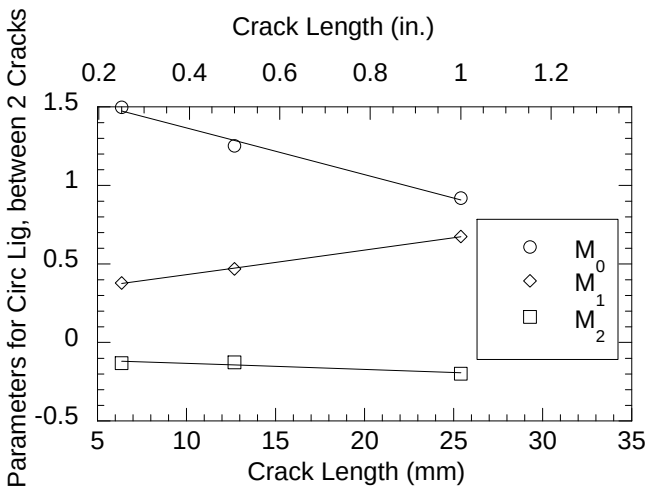

Figure 23.
Variation of fitting parameters M_0, M_1, and M_2 with total crack length for specimens with two throughwall axial cracks separated by a circumferential ligament. Symbols represent fitting parameters of the data for the three crack lengths shown in Fig. 22 to Eq. 2 and lines are linear fits to the fitting parameters as functions of crack length.

A comparison of the effects of axial and circumferential ligament lengths on the ligament rupture pressure of 2 x 100% deep cracks of total length 25 mm (1 in.) is shown in Fig. 24. The symbols in this figure represent FEA results and the curves are predicted from our fitting procedure discussed above. Note that for small ligament lengths, a circumferential ligament increases the ligament rupture pressure slightly more than an axial ligament of the same length. The asymptotic behavior of the two types of ligaments for large ligament lengths result from the fact that for the geometries being considered the total crack length for the axial case includes the ligament width whereas the total crack length for the circumferential case is independent of ligament width (Figs 14a–b). As a result, the individual crack length in the axial ligament case approaches zero as the axial ligament length increases, whereas the individual crack length is independent of the circumferential ligament length. The ligament rupture pressure curve for the axial ligament case provides a conservative (i.e., upper) bound to the curve for the circumferential ligament case at large ligament lengths, whereas the two are comparable for ligament lengths ≤ 3 mm (0.12 in.).

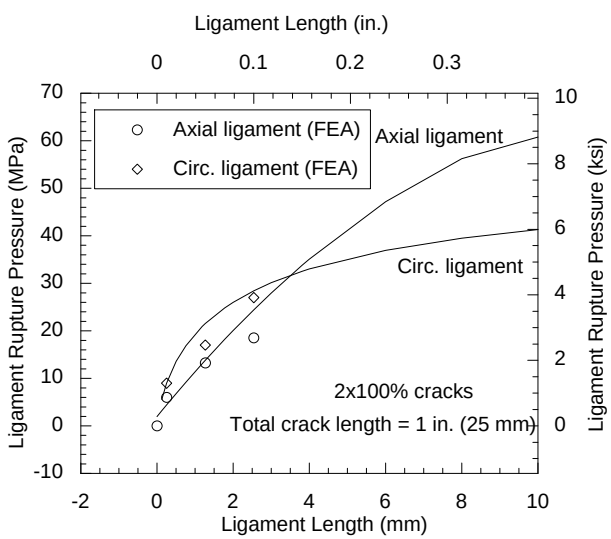

Figure 24.
Effects of axial and circumferential ligament widths on ligament rupture pressure of two 12 mm 100%TW axial cracks separated by axial or circumferential ligaments (total crack length = 25 mm) . Symbols denote the FEA results and the lines are the fitted values.

2.4 Generation of Failure Maps

Experience with testing of multiple PTW laser cut and EDM notches has shown that radial ligaments at the through-thickness notch tips of individual notches that are > 2.5 mm (0.1 in.) long and > 70% deep tend to rupture before the axial or circumferential ligaments of length ≥ 0.25 mm (0.01 in.).[2] Therefore, in generating the failure maps, it was assumed that during pressurization, the radial ligaments ruptured first, followed by the rupture of the axial (or circumferential) ligaments separating the cracks, and finally unstable burst of the resulting single throughwall crack. All the tubes considered in generating the failure maps had a diameter of 22–mm (0.875 in.).

Failure maps were developed for 80 and 90% deep cracks at 300°C. An Excel spreadsheet was written that computed the radial ligament rupture pressure by the equivalent rectangular crack method, the axial (or circumferential) ligament rupture pressure by the correlations developed above from FEA, and finally the unstable burst pressure of a single throughwall crack by the Erdogan correlation.[6] The equivalent area analyses and the burst calculations used:

S_y = 267 MPa (39 ksi) and S_u = 608 MPa (88 ksi) and flow stress parameter k = 0.55

for the properties at 300°C.

The failure maps for cracks of a given depth and at a given pressure (e.g., ΔP_{NO}) were generated by determining the various combinations of ligament length and crack length that correspond to the given pressure. Definitions of the various crack and ligament lengths are given in Figs. 14-15.

2.4.1 Failure Maps for Normal Operation (ΔP_{NO})

Single Crack

The failure map for a single crack at normal operation is shown in Fig. 25. Any crack of length less than 1.7 in. (44 mm), irrespective of depth, is predicted to remain stable (i.e., no unstable burst) during normal operation. The map also shows the combination of crack length and crack depth where neither radial ligament rupture nor unstable burst is predicted to occur. Also shown is the region where radial ligament rupture is predicted to occur without unstable burst.

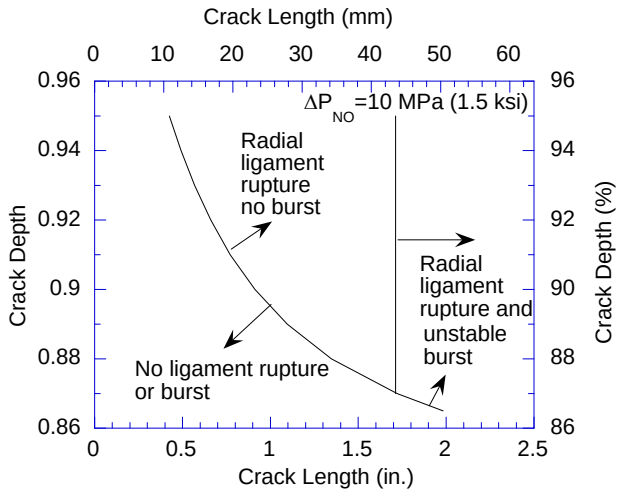

Figure 25.
Failure map of a single crack at normal operating pressure ΔP_{NO}.

Two Cracks

Figs 26a–b show failure maps for two–90% deep axial cracks separated by either an axial or a circumferential ligament, respectively. As in the case of a single crack, cracks shorter than 1.7 in. (44 mm) are predicted to remain stable (no unstable burst) for all ligament widths. Further, if two cracks have an axial ligament length greater than 1.4 mm (0.055 in.) or two cracks have a circumferential ligament length greater than 1.3 mm (0.050 in.), then cracks with a total length longer than 1.7 in. (44 mm) will experience unstable burst only if the ligament length/crack length lies in the zone marked "unstable burst". For shorter ligament lengths, both the radial and axial or circumferential ligaments are predicted to rupture provided the crack length/ligament length lies in the zones marked "radial/axial lig. rupture" or "radial/circ. lig. rupture" in the figures, but the single TW crack that results after the ligament rupture is predicted to remain stable (no unstable burst) provided the overall length is less than 1.7 in. (44 mm). The failure maps for the axial and circumferential ligament cases are quite similar and the axial ligament case provides a conservative bound to the circumferential ligament case, i.e., the non-failure region for the axial ligament case is contained within the non-failure region for the circumferential ligament case. The failure maps for two–80% deep cracks are not plotted because none of the failure mechanisms become active unless cracks are very long and not of practical interest.

Four Cracks

Figure 27a shows the failure map for four–90% deep axial cracks separated by three axial ligaments. As in the case of a single crack, cracks with a total length shorter than 1.7 in. (44 mm) are predicted to remain stable (no unstable burst) for all ligament lengths. Further, if four axial cracks have an axial ligament length greater than 0.5 mm (0.02 in.), then cracks longer than 1.7 in. (44 mm) will experience unstable burst only if the ligament length/crack length lies in the zone marked "unstable burst". For shorter ligament lengths, both the radial and axial ligaments are predicted to rupture provided the crack length/ligament length lies in the zone marked "radial and axial ligament rupture" in the figure, but the single TW crack that results after ligament rupture is predicted to remain stable (no unstable burst) provided the overall length is less than 1.7 in. (44 mm).

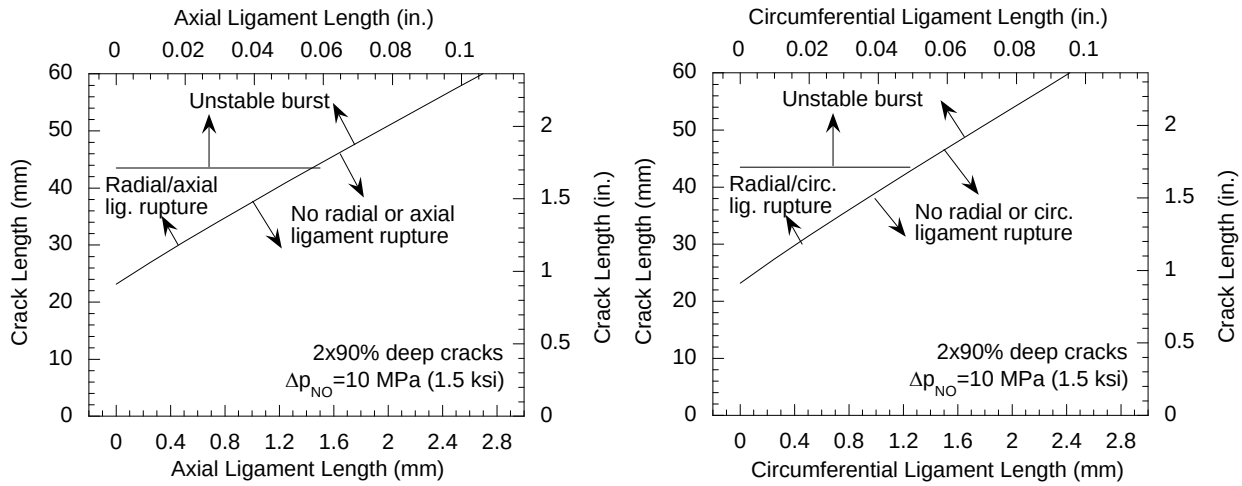

(a) (b)

Figure 26. Failure maps for SG tubes with two 90% deep axial cracks separated by (a) an axial ligament (Type C) and (b) a circumferential ligament (Type D) at normal pressure (ΔP_{NO}). "Crack length" denotes total overall length of the individual cracks and ligaments.

Six Cracks

Figure 27b shows the failure map for six–90% deep axial cracks separated by five axial ligaments. As in the case of a single crack, cracks shorter than 1.7 in. (44 mm) are predicted to remain stable (no unstable burst) for all ligament widths. Further, if six axial cracks have an axial ligament length greater than 0.3 mm (0.012 in.), then cracks longer than 1.7 in. (44 mm) will experience unstable burst only if the ligament length/crack length lies in the zone marked "unstable burst". For narrower ligament widths, both the radial and axial ligaments are predicted to rupture provided the crack length/ligament length lie in the zone marked "radial and axial ligament rupture" in the figure, but the resulting single crack after ligament rupture is predicted to remain stable (no unstable burst) provided the overall crack length is less than 1.7 in. (44 mm).

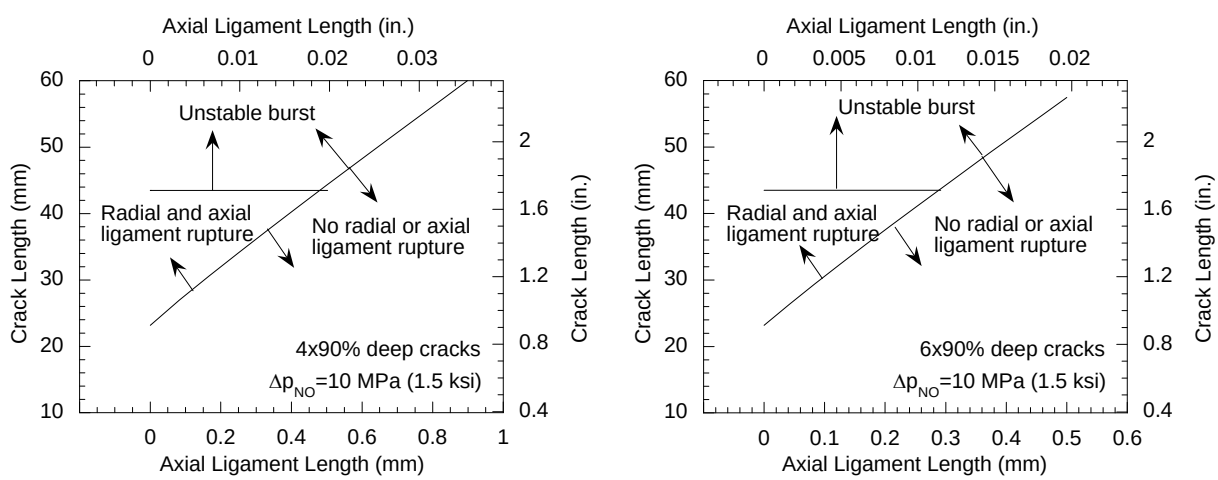

(a) (b)

Figure 27. Failure maps for SG tubes with (a) four and (b) six 90% deep axial cracks separated by axial ligaments at normal pressure (ΔP_{NO}). "Crack length" denotes the total overall length of the individual cracks and ligaments.

2.4.2 Failure Maps for Main Steam Line Break Pressure (ΔP_{MSLB})

Single Crack

The failure map of a single crack at main steam line break pressure is shown in Fig. 28. Any crack of length less than 0.85 in. (22 mm), irrespective of depth, is predicted to remain stable (i.e., no unstable burst) at main steam line break pressure. The map also shows the combination of crack length and crack depth where neither radial ligament rupture nor unstable burst is predicted to occur. Also shown is the region where radial ligament rupture is predicted to occur without unstable burst.

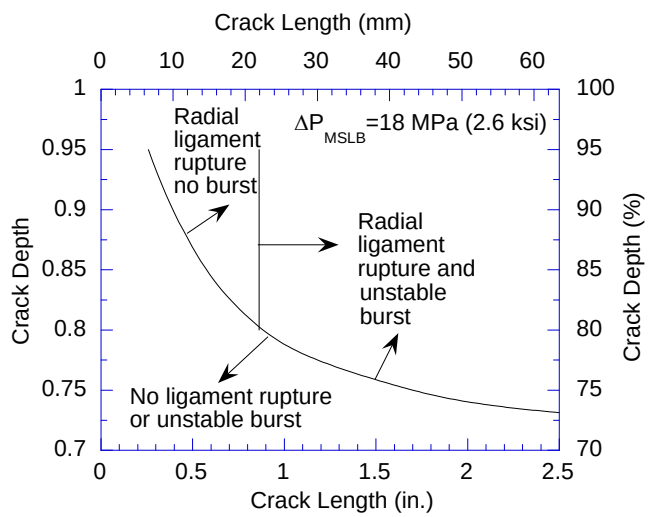

Figure 28.
Failure map of a single crack at main steam line break pressure ΔP_{MSLB}.

Two Cracks

Figures 29a–b show the failure maps for two–90% deep axial cracks separated by an axial and a circumferential ligament, respectively. As in the case of a single crack, cracks shorter than 0.85 in. (22 mm) are predicted to remain stable (no unstable burst) for all ligament widths. Further, if two Type C cracks have an axial ligament length greater than 2.5 mm (0.1 in.) or two type D cracks have a circumferential ligament length greater than 2 mm (0.080 in.), then cracks longer than 0.85 in. (22 mm) will experience unstable burst only if the ligament length/crack length lies in the zone marked "unstable burst". For shorter ligament lengths, both the radial and axial or circumferential ligaments are predicted to rupture provided the crack length/ligament length lies in the zones marked "radial/axial ligament rupture" or "radial/circ. lig. rupture" in the figures, but the resulting single TW crack after ligament rupture is predicted to remain stable (no unstable burst) provided the overall crack length is less than 0.85 in. (22 mm). Again the failure maps for the axial and circumferential ligament cases are quite similar and the axial ligament case provides a conservative bound to the circumferential ligament case, i.e., the non-failure regime for the axial ligament case is contained within the non-failure regime for the circumferential ligament case.

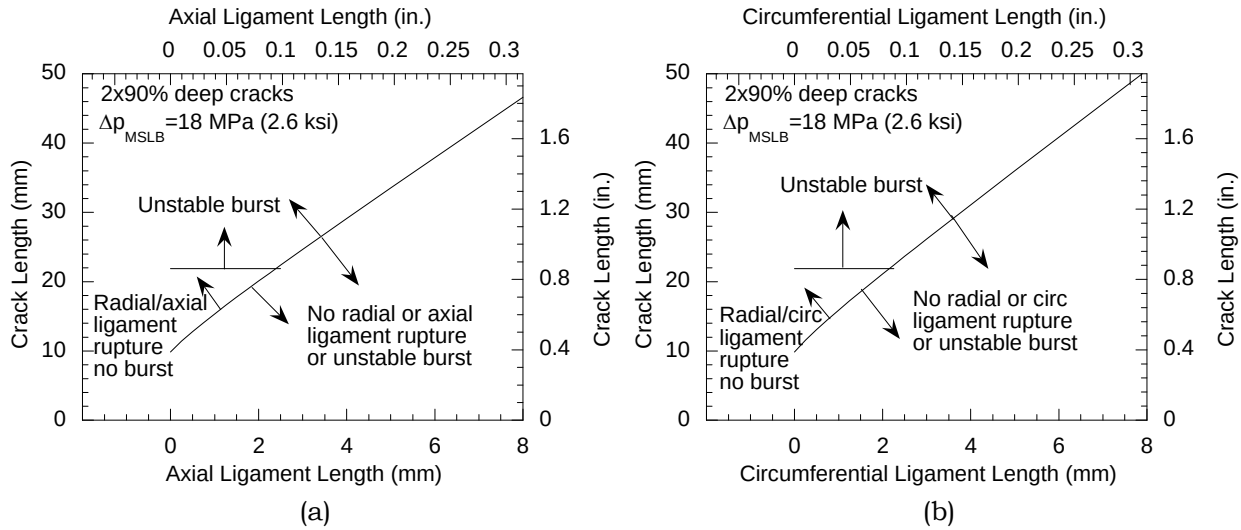

(a) (b)

Figure 29. Failure maps for SG tubes with two 90% deep axial cracks separated by (a) an axial ligament (Type C) and (b) a circumferential ligament (Type D) at main steam line break pressure (ΔP_{MSLB}). "Crack length" denotes the total overall length of the individual cracks and ligaments.

The failure maps for two–80% deep axial cracks separated by an axial and a circumferential ligament are shown in Figs. 30a–b, respectively. As before, cracks with total lengths less than 0.85 in. (22 mm) will not burst unstably irrespective of the axial or circumferential ligament length. In contrast to the two-90% deep crack case, there is no crack length/ligament length regime in which radial/axial (or radial/circumferential) ligament rupture will occur without unstable burst. As before, the failure maps for the axial and circumferential ligament cases are quite similar and the axial ligament case provides a conservative bound to the circumferential ligament case, i.e., the non-failure regime for the axial ligament case is contained within the non-failure regime for the circumferential ligament case

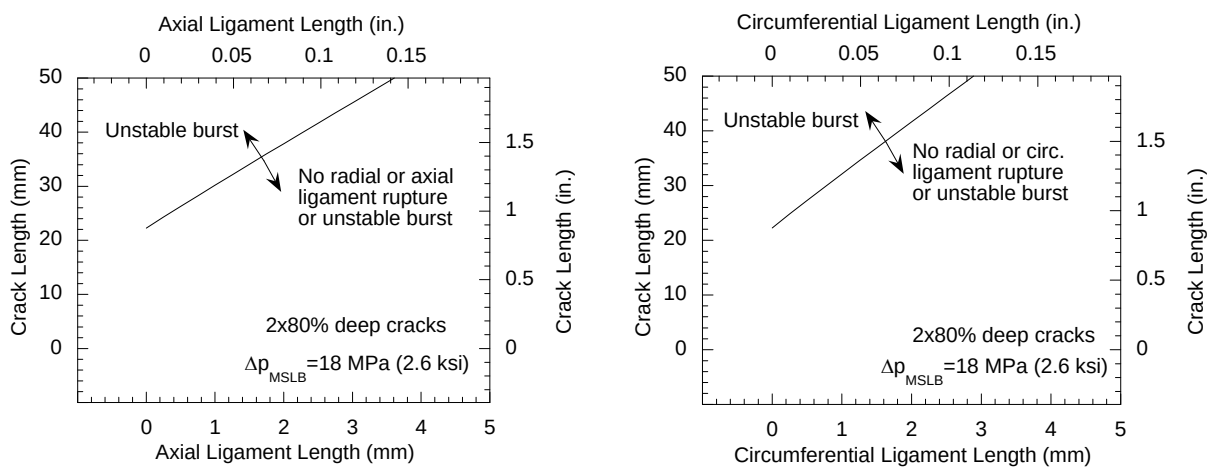

(a) (b)

Figure 30. Failure maps for SG tubes with two 80% deep axial cracks separated by (a) an axial ligament (Type C) and (b) a circumferential ligament (Type D) at main steam line break pressure (ΔP_{MSLB}). "Crack length" denotes the total overall length of the individual cracks and ligaments.

Four Cracks

The failure map for four–90% deep axial cracks separated by three axial ligaments is plotted in Figure 31a. As in the case of a single crack, cracks with a total length less than 0.85 in. (22 mm) are predicted to remain stable (no unstable burst) for all ligament widths. Further, if four Type C cracks have an axial ligament length greater than 0.75 mm (0.03 in.), then cracks longer than 0.85 in. (22 mm) will experience unstable burst only if the ligament length/crack length lies in the zone marked "unstable burst". For shorter ligament lengths, both radial and axial or circumferential ligaments are predicted to rupture provided the crack length/ligament length lie in the zone marked "radial/axial lig. rupture" in the figure, but the resulting single TW crack after ligament rupture is predicted to remain stable (no unstable burst) provided the overall crack length is less than 0.85 in. (22 mm). However, in contrast to previous cases, there is a narrow region of axial ligament length/crack length in which the cracks will undergo radial ligament rupture without experiencing axial ligament rupture or unstable burst. The failure map for four–80% deep axial cracks separated by three axial ligaments is shown in Figs. 31b. Cracks longer than 0.85 in. (22 mm) will not necessarily burst unstably provided the crack length/ligament length lie in the region marked as "no radial or axial ligament rupture". In contrast to the four-90% deep crack case, there are no crack length/ligament length regimes in which either radial and axial ligaments will rupture or radial but no axial ligament will rupture.

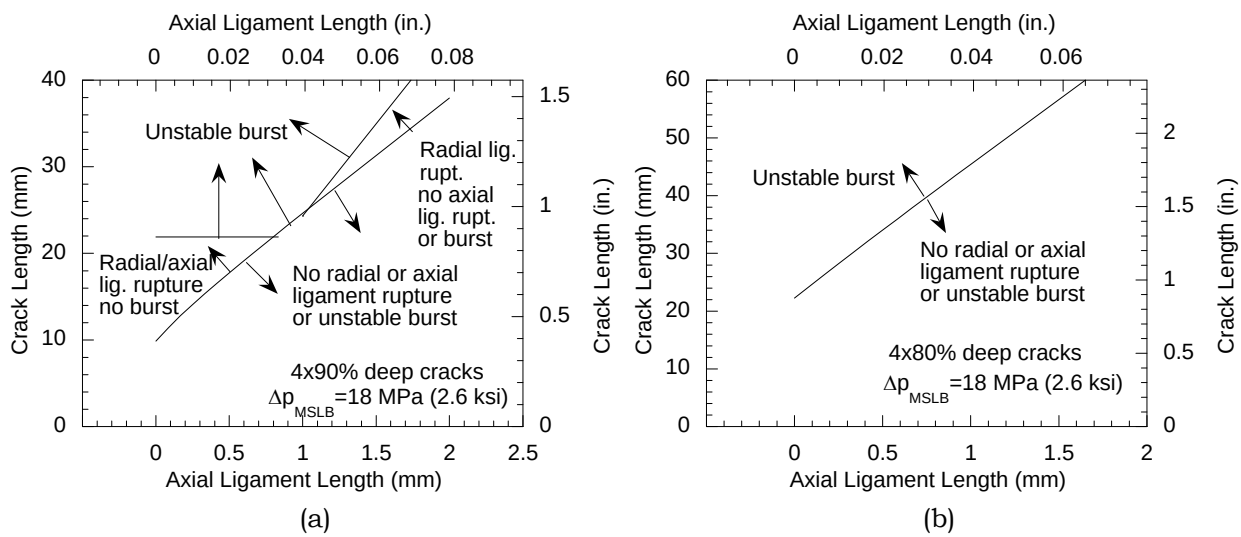

Figure 31. Failure maps for SG tubes with four axial cracks, (a) 90% and (b) 80% deep, separated by three axial ligaments (Type C) at main steam line break pressure (ΔP_{MSLB}). "Crack length" denotes the total overall length of the individual cracks and ligaments.

Six Cracks

Figures 32a-b show the failure maps for six–90% deep and six-80% deep axial cracks separated by five axial ligaments, respectively. The failure maps are similar to the four–90% and four-80% deep axial crack cases (Figs. 31a-b), except that the zones where unstable burst occurs are more limited. As before, cracks with a total length less than 0.85 in. (22 mm) are predicted to remain stable (no unstable burst) for all ligament widths.

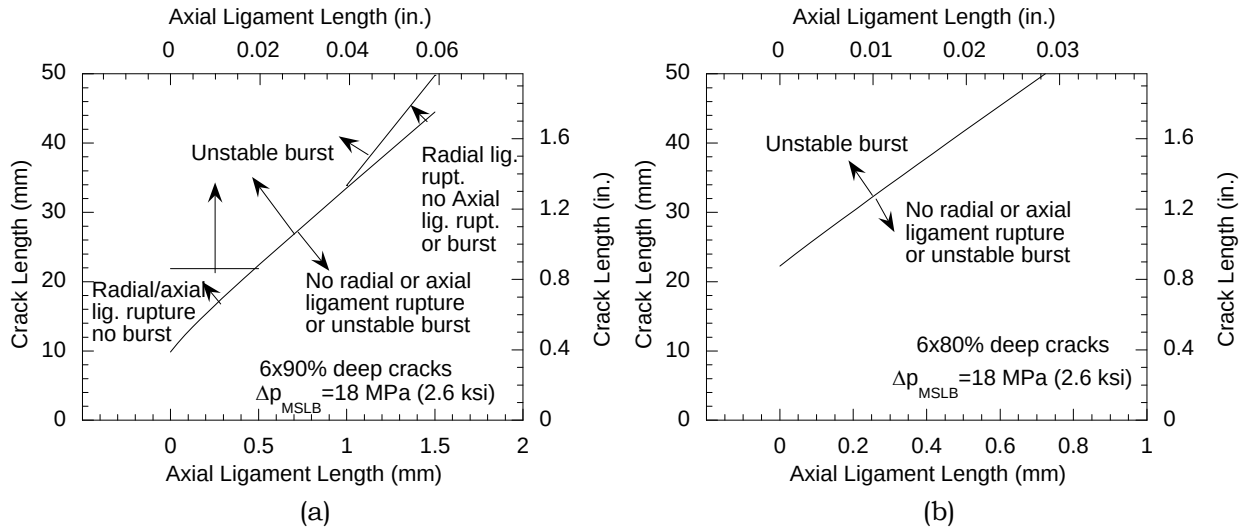

Figure 32. Failure maps for SG tubes with six axial cracks, (a) 90% and (b) 80% deep, separated by five axial ligaments (Type C) at main steam line break pressure (ΔP_{MSLB}). "Crack length" denotes the total overall length of the individual cracks and ligaments.

2.4.3 Failure Maps for 1.4xMain Steam Line Break Pressure ($1.4\Delta P_{MSLB}$)

Since a safety factor of 1.4 is used for accident analysis, the failure maps for $1.4\Delta P_{MSLB}$ are of interest.

Single Crack

The failure map of a single crack at 1.4 times main steam line break pressure, shown in Fig. 33, is similar to that at main steam line break pressure (Fig. 28) except that the maximum crack length below which no unstable burst is predicted is reduced to 0.59 in. (15 mm).

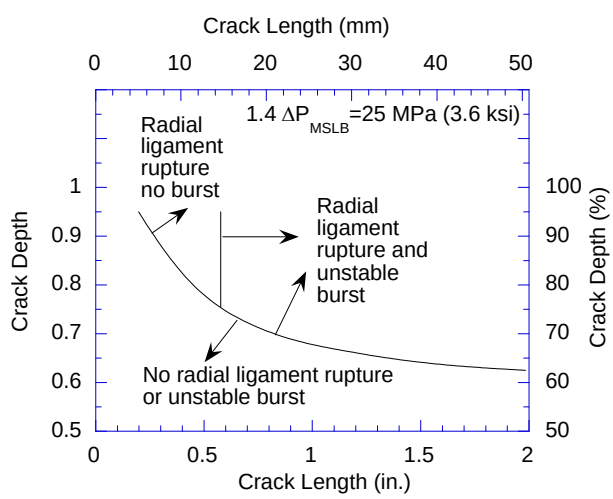

Figure 33.
Failure map of a single crack at 1.4 times main steam line break pressure $1.4\Delta p_{MSLB}$.

Two Cracks

Figures 34a–b show the failure maps for two–90% deep axial cracks separated by an axial and a circumferential ligament, respectively. The maps are similar to those for the postulated MSLB case (Figs. 29a-b), except cracks with a total length shorter than 0.59 in. (15 mm) are predicted to remain stable (no unstable burst) for all ligament lengths. Again the failure maps for the axial and circumferential ligament cases are quite similar, and the axial ligament case provides a conservative bound to the circumferential ligament case, i.e., the non-failure regime for the axial ligament case is contained within the non-failure regime for the circumferential ligament case.

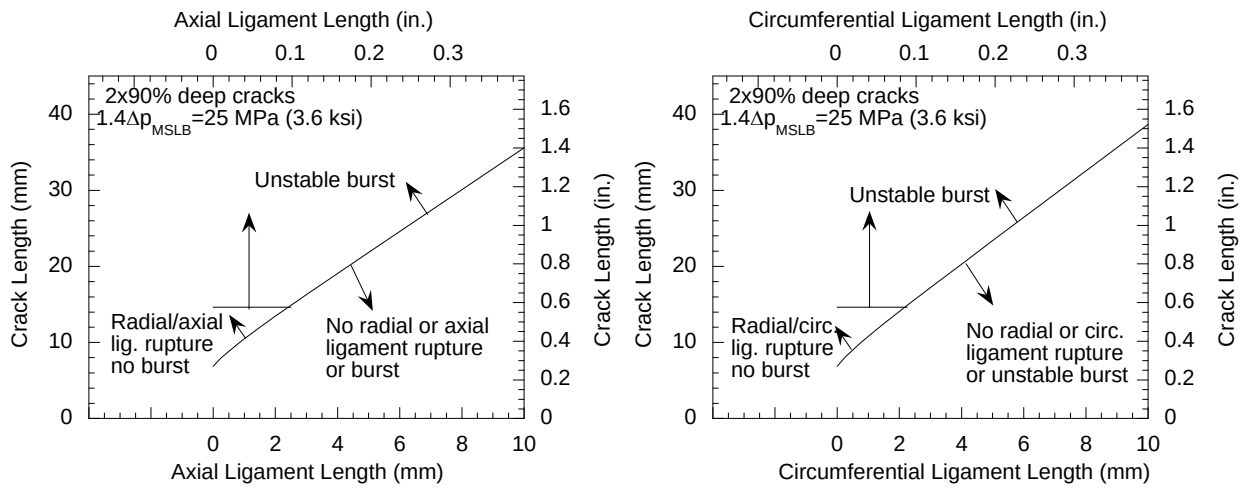

(a) (b)

Figure 34. Failure maps for SG tubes with two 90% deep axial cracks separated by (a) an axial ligament (Type C) and (b) a circumferential ligament (Type D) at 1.4 times main steam line break pressure ($1.4\Delta P_{MSLB}$). "Crack length" denotes the total overall length of the individual cracks and ligaments.

The failure maps for two–80% deep axial cracks separated by an axial and a circumferential ligament are shown in Figs. 35a–b, respectively. The maps are similar to those for the postulated MSLB case (Figs. 29a-b), except cracks shorter than 0.59 in. (15 mm) are predicted to remain stable (no unstable burst) for all ligament lengths and there is a small zone of crack length/ligament length where radial and axial (or circumferential) ligaments are predicted to rupture without burst.

Four Cracks

The failure map for four–90% deep axial cracks separated by three axial ligaments is plotted in Figure 36a. The map is similar to the map for the postulated MSLB case (Fig. 31a), except that cracks shorter than with a total length 0.59 in. (15 mm) are predicted to remain stable (no unstable burst) for all ligament widths. The failure map for four–80% deep axial cracks separated by three axial ligaments is shown in Figs. 36b. Because of the higher pressure, two additional failure zones, which were absent in the postulated MSLB case (Fig. 31b), appear in the $1.4\Delta p_{MSLB}$ case (Fig. 36b).

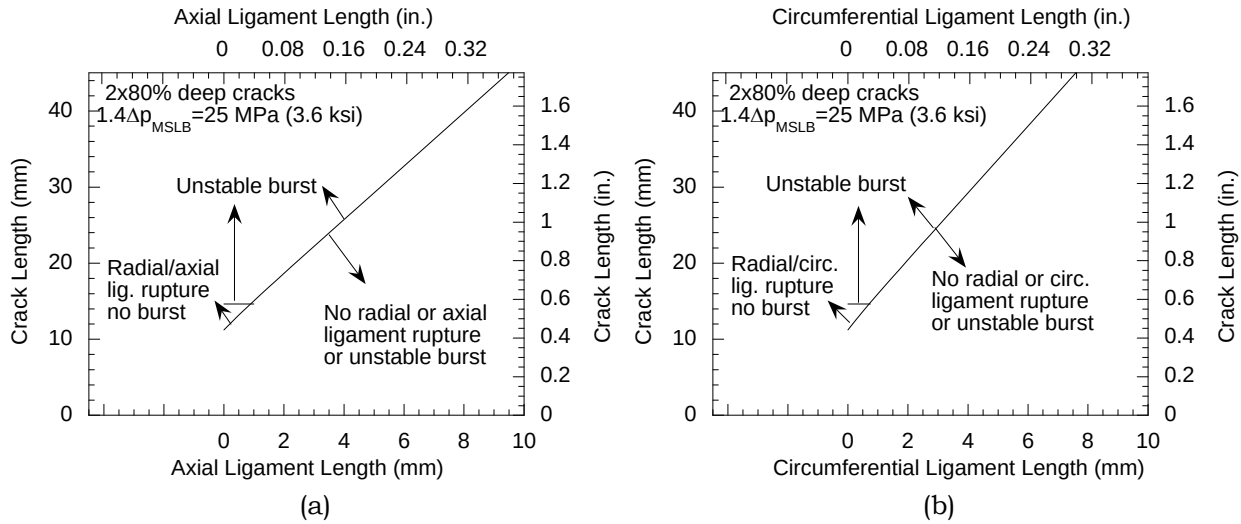

(a) (b)

Figure 35. Failure maps for SG tubes with two 80% deep axial cracks separated by (a) an axial ligament (Type C) and (b) a circumferential ligament (Type D) at 1.4 times main steam line break pressure ($1.4\Delta P_{MSLB}$). "Crack length" denotes the total overall length of the individual cracks and ligaments.

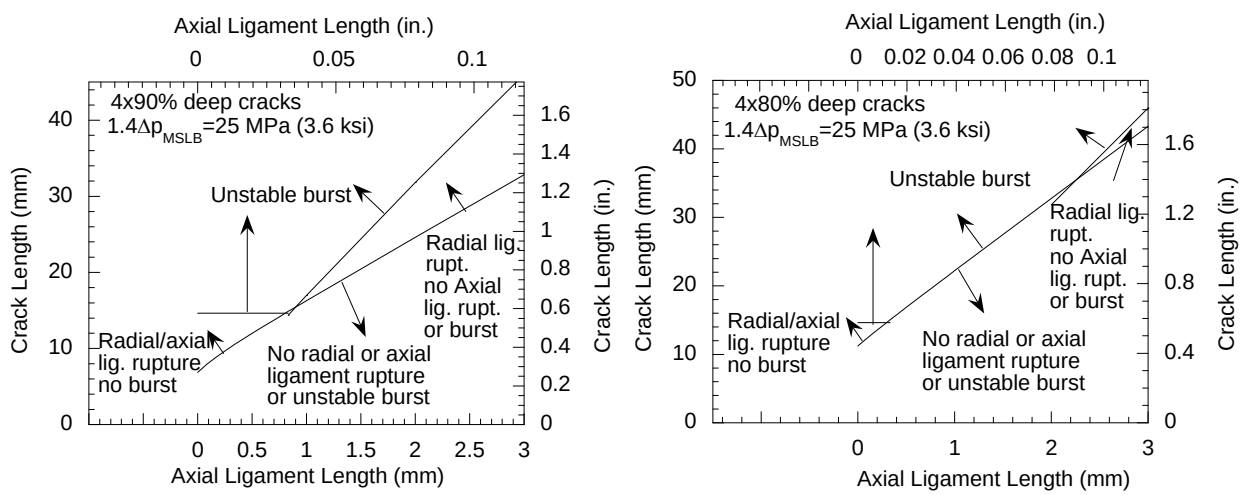

(a) (b)

Figure 36. Failure maps for SG tubes with four axial cracks, (a) 90% and (b) 80% deep, separated by three axial ligaments (Type C) at 1.4 times main steam line break pressure ($1.4\Delta P_{MSLB}$). "Crack length" denotes the total overall length of the individual cracks and ligaments.

Six Cracks

Figure 37a-b show the failure maps for six–90% and six-80% deep axial cracks separated by five axial ligaments, respectively. The maps are similar to those for the postulated MSLB case (Figs. 32a-b), except cracks with a total length shorter than 0.59 in. (15 mm) are predicted to remain stable (no unstable burst) for all ligament widths. Also, because of the higher pressure, an

additional failure zone, which was absent in the postulated MSLB case (Fig. 32b), appears in the $1.4\Delta p_{MSLB}$ case (Fig. 37b).

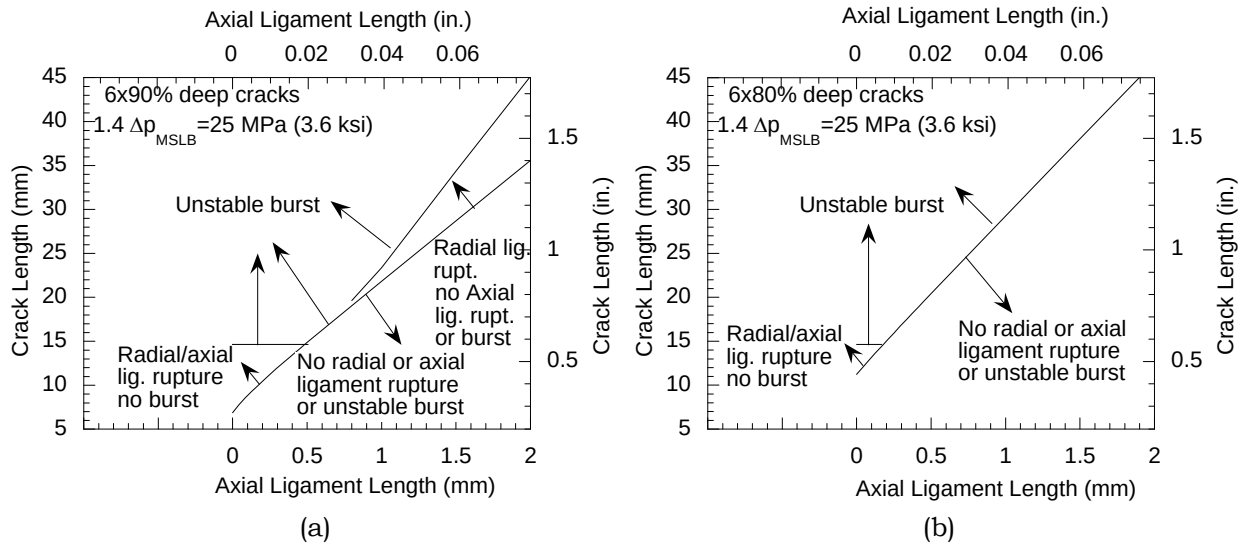

Figure 37. Failure maps for SG tubes with six axial cracks, (a) 90% and (b) 80% deep, separated by five axial ligaments (Type C) at 1.4 times main steam line break pressure ($1.4\Delta P_{MSLB}$). "Crack length" denotes the total overall length of the individual cracks and ligaments.

2.4.4 Failure Maps for 3xNormal Operating Pressure ($3\Delta P_{NO}$)

Since a safety factor of 3 is used in design, the failure maps for $3\Delta P_{NO}$ are of interest.

Single Crack

The failure map of a single crack at 3 times normal operating pressure ($3\Delta P_{NO}$) is shown in Fig. 38. The map is similar to the $1.4\Delta P_{MSLB}$ case (Fig. 33), except that any crack of length less than 0.44 in. (11 mm), irrespective of depth, is predicted to remain stable (no unstable burst) at 3 times normal operating pressure.

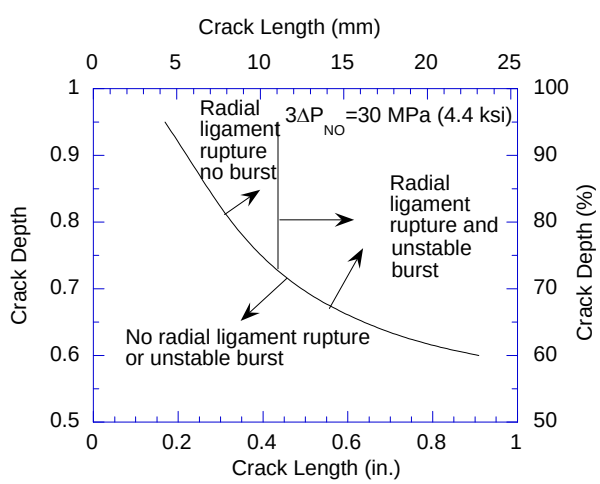

Figure 38.
Failure map of a single crack at 3 times normal operating pressure $3\Delta P_{NO}$.

Two Cracks

Figures 39a–b show the failure maps for two–90% deep axial cracks separated by an axial and a circumferential ligament, respectively. The maps are similar to the $1.4\Delta P_{MSLB}$ case (Figs. 34 a-b), except cracks with a total length shorter than 0.44 in. (11 mm) are predicted to remain stable for all ligament widths. As before, the failure maps for the axial and circumferential ligament cases are quite similar, and the axial ligament case provides a conservative bound to the circumferential ligament case, i.e., the non-failure regime for the axial ligament case is contained within the non-failure regime for the circumferential ligament case.

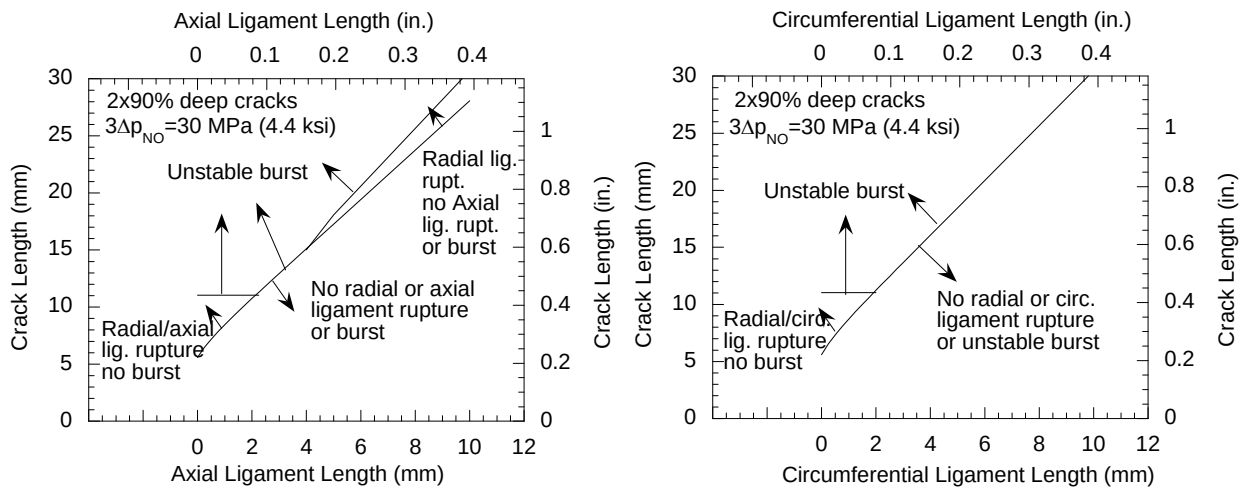

(a) (b)

Figure 39. Failure maps for SG tubes with two 90% deep axial cracks separated by (a) an axial ligament (Type 2) and (b) a circumferential ligament (Type 4) at 3 times normal operating pressure ($3\Delta P_{NO}$). "Crack length" denotes the total overall length of the individual cracks and ligaments.

The failure maps for two–80% deep axial cracks separated by an axial and a circumferential ligament are shown in Figs. 40a–b, respectively. The maps are similar to the $1.4\Delta P_{MSLB}$ case (Figs. 35a-b). As before, the axial ligament case provides a conservative bound to the circumferential ligament case, i.e., the non-failure regime for the axial ligament case is contained within the non-failure regime for the circumferential ligament case.

Four Cracks

The failure maps for four–90% and four-80% deep axial cracks separated by three axial ligaments are plotted in Figure 41a-b, respectively. The maps are similar to the $1.4\Delta P_{MSLB}$ case (Figs. 36a-b), except cracks with a total length shorter than 0.44 in. (11 mm) are predicted to remain stable (no unstable burst) for all ligament widths.

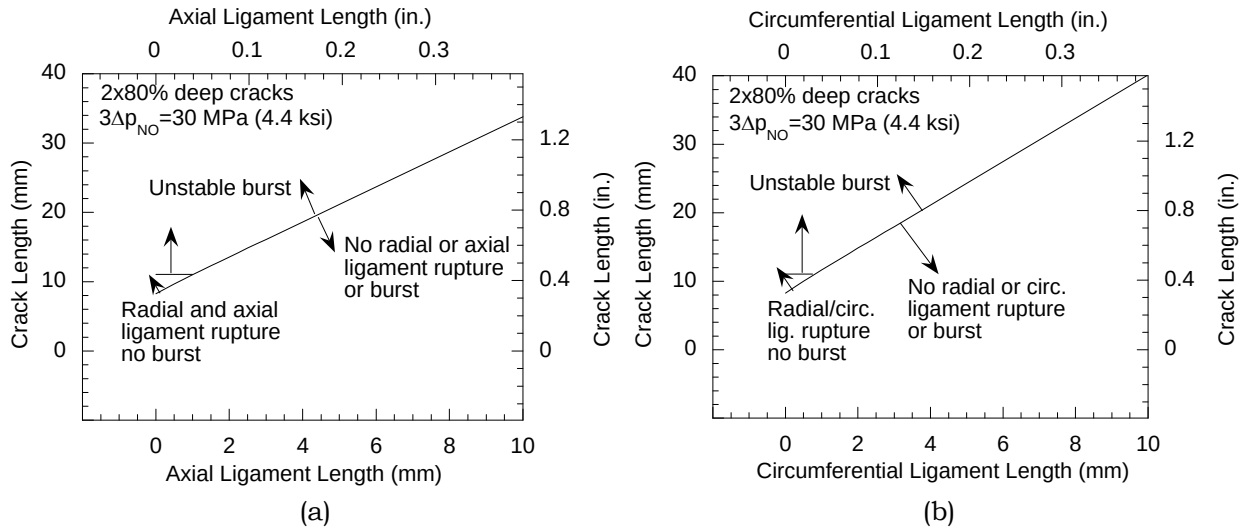

Figure 40. Failure maps for SG tubes with two 80% deep axial cracks separated by (a) an axial ligament (Type C) and (b) a circumferential ligament (Type D) at 3 times normal operating pressure ($3\Delta P_{NO}$). "Crack length" denotes the total overall length of the individual cracks and ligaments.

Six Cracks

Figure 42a-b show the failure maps for six–90% and six-80% deep axial cracks, respectively, separated by five axial ligaments. The maps are similar to the $1.4\Delta P_{MSLB}$ case (Figs. 37a-b), except cracks shorter than 0.44 in. (11 mm) are predicted to remain stable for all ligament widths. Also, because of the higher pressure, an additional failure zone, which was absent in the $1.4\Delta P_{MSLB}$ case (Fig. 37b), appears in the $3\Delta P_{NO}$ case (Fig. 42b).

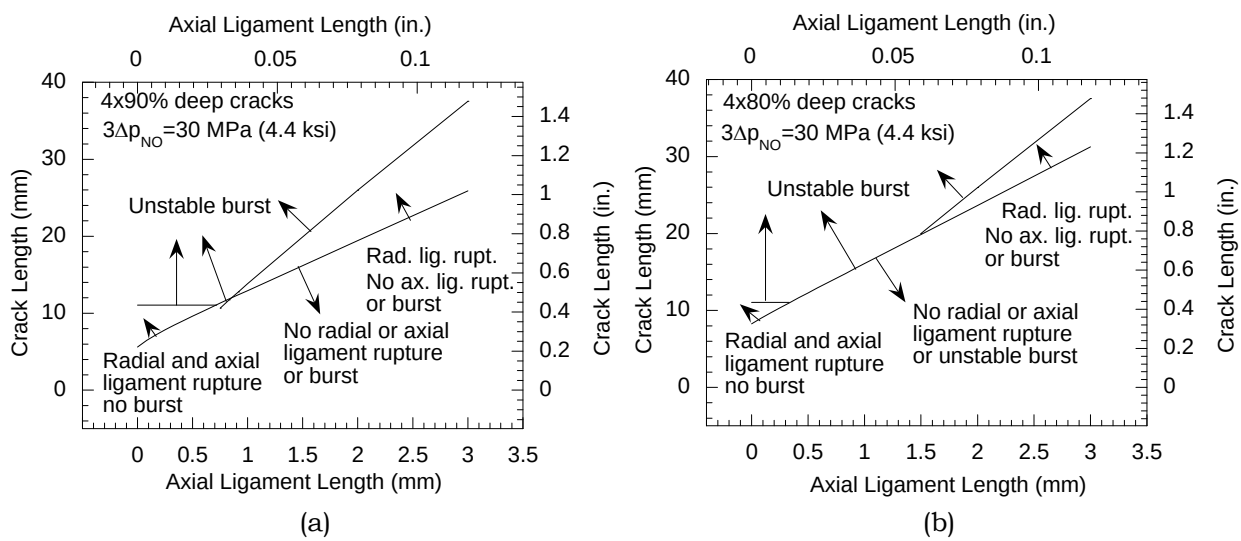

Figure 41. Failure maps for SG tubes with four axial cracks, (a) 90% and (b) 80% deep, separated by three axial ligaments (Type C) at 3 times normal operating pressure ($3\Delta P_{NO}$). "Crack length" denotes the total overall length of the individual cracks and ligaments.

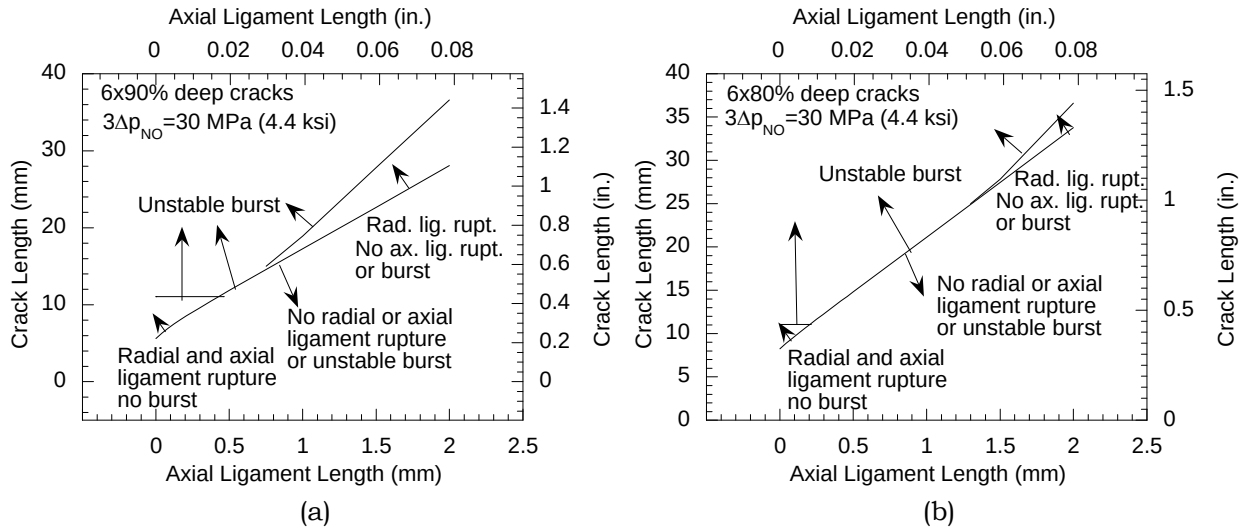

Figure 42. Failure maps for SG tubes with six axial cracks, (a) 90% and (b) 80% deep, separated by five axial ligaments (Type C) at 3 times normal operating pressure ($3\Delta P_{NO}$). "Crack length" denotes the total overall length of the individual cracks and ligaments.

2.5 Discussion and Conclusions

The ANL radial ligament rupture model for axial part–throughwall cracks have been validated over the last several years by tests on specimens with a single EDM notch or two EDM notches separated by axial or circumferential ligaments. At the same time, finite element analyses have been conducted to establish numerical models for predicting the coalescence of two axial throughwall cracks separated by axial or circumferential ligament of various widths. All of these models together with the well–known unstable burst pressure correlation for a single throughwall crack were used to generate a series of failure maps. Each map, plotted with ligament length and overall crack length as coordinates, is based on the ligament lengths and crack lengths for a fixed number (2, 4, and 6) of axial part–throughwall cracks with a fixed depth that are predicted to fail by various mechanisms at pressure differences of ΔP_{NO}, ΔP_{MSLB}, $3\Delta P_{NO}$, or $1.4\Delta P_{MSLB}$. The failure mechanisms that are considered are the rupture of radial ligament (following which leakage occurs), crack coalescence (i.e., rupture of axial or circumferential ligament), and unstable burst. Each map delineates the regions of various failure mechanisms from each other and identifies regions (i.e., combinations of crack length and ligament length) for which failure (or non-failure) of one of the following types is predicted:

(a) No radial or axial (or circumferential) ligament rupture and no unstable burst.

(b) Radial ligament rupture but no axial (or circumferential) ligament rupture or unstable burst.

(c) Radial and axial (or circumferential) ligament rupture but no unstable burst.

(d) Unstable burst.

These maps illustrate the importance of ligament and crack sizes in structural and leakage integrity evaluations and may be useful for identifying flaws that require more detailed evaluation during in-service inspection. They have been generated using the typical strength properties of 22

mm (0.875 in.) OD, 1.3 mm (0.05 in.) wall thickness Alloy 600 tubes at 300°C (570°F). If necessary, the maps can be modified for tubes of a different size and/or strength properties. However, because the failure pressures corresponding to all the failure mechanisms depend linearly on the flow stress and the maps are plotted in terms of the crack and ligament lengths, they should be invariant provided the ratio between the relevant pressure difference (ΔP_{NO} or ΔP_{MSLB}) and the flow stress remains approximately constant.

The failure maps have been generated for idealized and regular geometry of cracks. In reality, individual crack lengths and ligament lengths will vary in the same specimen and the ligament geometry can be a mixture of the various idealized geometries considered in this report. Therefore, to use these maps in an actual application, the user has to exercise judgment in determining which map is applicable. Some averaging techniques (e.g., equivalent rectangular crack) will be needed to replace the actual crack geometry (as determined by NDE) with one of the idealized crack geometries considered in this report. For example, crack lengths and ligament lengths could be deliberately chosen to represent an upper or lower bound to the actual case. If NDE is unable to resolve the ligaments, the predicted failure pressure based on the total crack length will in all cases be conservative. Real stress corrosion cracks have highly complex geometries, and although we have made some progress in the understanding of the various failure mechanisms involved by analyzing and testing a limited number of idealized geometries, the prediction of failure pressures of complex stress corrosion cracks is still evolving.

3 Leak Rate Studies

3.1 Introduction

The primary water in the steam generator tubes must be maintained at high pressure to remain liquid. If a leak occurs in the tube, when the water from the primary side enters the lower pressure secondary side, it will flash to steam. For incompressible flows, the leak rate is proportional to $\Delta p^{1/2}$ and the flow rate for a given condition on the primary side will monotonically increase as the secondary side pressure is decreased. For compressible fluids a phenomenon called choking can occur in which for secondary pressures lower than a certain critical value the flow no longer continues to increase as the secondary pressure is decreased. Most phenomenological models of leaks from cracks in steam generator tubes in main steam line break accidents assume that the flow through a crack is choked. However, earlier studies at ANL have shown for a range of crack geometries choking does not occur. For such geometries, the flow through the crack can be described by the flow of an incompressible fluid through an orifice with an area equal to that of the flaw. This model has yielded excellent predictions over a wide range of pressures and temperatures for flaw opening dimensions as small as 0.18 mm (0.007 in.). However, it is clear that for some geometries choking may occur and that for short cracks, frictional losses, which are not accounted for in a simple orifice model, will become significant. A series of tests has been performed to try to better determine the range of geometries for which the simple, single–phase orifice model is applicable.

3.2 Test Procedure

The tests were performed in two stages. The first stage was carried out in the room–temperature, high–pressure test facility. The target pressure for the overall leak testing was 17.2 MPa (2500 psi), which is approximately the postulated MSLB pressure. However, if a flaw leaked at 7.6 MPa (1100 psi), which corresponds to normal SG operating pressure, it was then tested at this lower pressure. The leak rate was measured at several values of the pressure up to the target pressure and then re–measured at several values of the pressure as the pressure was decreased.

After a tube was tested at RT, the flaw opening was characterized, and then the tube was tested in the High–Temperature Blowdown Test Facility (Stage 2 testing). In the Stage 2 tests, the flaws were first tested at RT to provide a check on results from the initial RT tests. They were then tested at 282°C (540°F) with zero back–pressure. The elevated–temperature test was then continued at the same primary pressure but with increasing levels of back–pressure. A decrease in flow rate with increasing back–pressure beyond that expected from the change in crack opening area due to a decrease in the elastic deformation indicates that the flow through the flaw is not choked.

Digital photography was used to characterize the flaw length and the OD opening along the flaw length. The photographs were taken with a Fujifilm Digital FinePix S1 Pro camera with an image file size of 3,040 x 2,016 pixels. The camera is fitted with a long range microscope Infinity K2 lens which can yield optical magnifications up to about 100x with add–on front objective lenses. The photographic system also includes fixtures to position the tube while focusing critically on the cracks and lighting to improve uniformity of flaw illumination and reduce glare.

The high–resolution flaw images produced by the hardware were analyzed using the ImageJ image analysis software, a public domain program based on the NIH Image software. The image analyses provided direct experimental measurements of crack opening displacement and crack opening area. Using digital magnification of the flaw images at highest resolution, the image can be magnified more than 400x without significantly degrading the image.

3.3 Test Results

3.3.1 Stage 1 Room Temperature Test Results

Four 22.2–mm (7/8–in.)–diameter Alloy 600 tubes containing laboratory–produced throughwall flaws were tested. These specimens are identified as SGL904, SGL905, SGL911, and SGL750, respectively.

The leak behavior of these flaws may be summarized as follows:

(1) In the 280 kPa (40 psi) air–pressurization test with the tube submerged in a water bath, all the flaws leaked air. Very small bubbles were emitted from one or two sites along the flaw length. When pressurized with water, none of the flaws showed any visual signs of leakage until much higher pressures. Specimen SGL904 leaked at a pressure of 13.8 MPa (2000 psi), SGL905 at 15.2 MPa (2200 psi), SGL911 at 9.7 MPa (1400 psi), and SGL750 leaked at 10.3 MPa (1500 psi) internal pressure, In all cases, the initial leak was in the form of individual droplets forming every 5–10 s, and none of the flaws leaked in the form of a continuous jet of liquid until the pressure was increased by a few MPa.

(2) Leak rate vs. pressure data were obtained at discrete intervals from flow collection and stop–watch measurements for pressures up to 17.2 MPa (2500 psi). In addition, the leak rate for each flaw was monitored vs. time at a constant pressure of 17.2 MPa (2500 psi) over time periods of 2–5 h to evaluate how stable the flaws were under constant pressure conditions.

(3) The leak rates increased with time at the constant test pressure of 17.2 MPa (2500 psi). Figures 43 and 44 show the leak rate as a function of time at 17.2 MPa (2500 psi) for Specimens SGL750, SGL905, SGL904, and SGL911, respectively. The leak rate for SGL904 started out at 0.90 kg/min (1.98 lbs/min) and, after somewhat more than five hours under constant pressure, the leak rate increased to 9.03 kg/min (19.9 lbs/min), a ten–fold increase. The other specimens exhibited similar behavior. At the end of the test period none of the flaws showed any evidence that the rate of increase in the leak rate was diminishing or approaching a stable, constant leak rate. The final leak rates were used with the observed crack opening areas for comparisons with the orifice model.

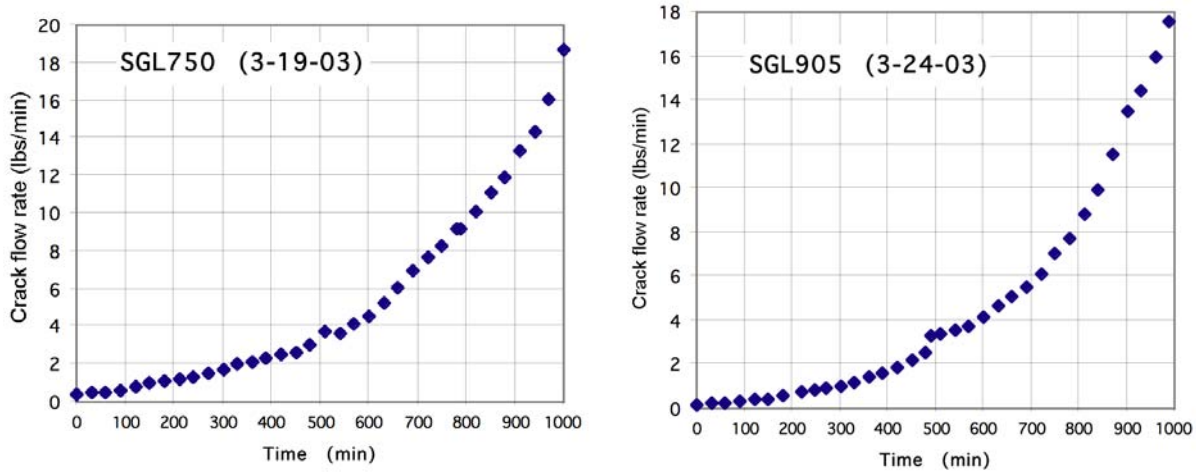

(a) (b)

Figure 43. Stage 1 leak–rate behavior of ODSCC axial Flaw (a) SGL750 and (b) SGL905 under a constant pressure of 17.2 MPa (2500 psi) with room–temperature water.

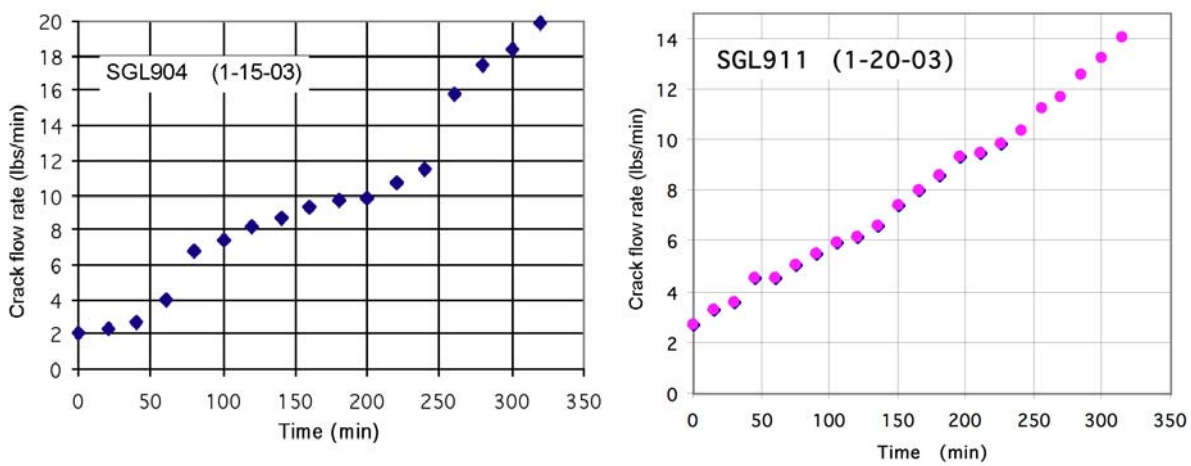

(a) (b)

Figure 44. Stage 1 leak–rate behavior of ODSCC axial flaw (a) SGL904 and (b) SGL911 under constant pressure of 17.2 MPa (2500 psi) with room–temperature water.

Based on dye penetrant results, the nominal pretest lengths on the outer surface of the flaws ranged from 5.8–7.9 mm (0.23 to 0.31 in.). Figures 45–48 show high–resolution images of flaws SGL750, SGL904, SGL905, and SGL911 after being tested at 17.2 MPa (2500 psi) in Stage 1 at RT. In all cases, there is an apparent increase in length during the testing. Superimposed on each image are 9 reference points (g1 – g9) equally spaced along the length of each flaw. These points are locations at which the flaw opening has been measured. These points, together with special feature numbers (sf1, sf2, etc.), serve as points of reference in the magnified images. Each flaw image contains a ruler with 0.40–mm (1/64–in.) divisions. The ruler image permits one to relate a specific number of image pixels to the known distance and thereby define the scale for the image analysis.

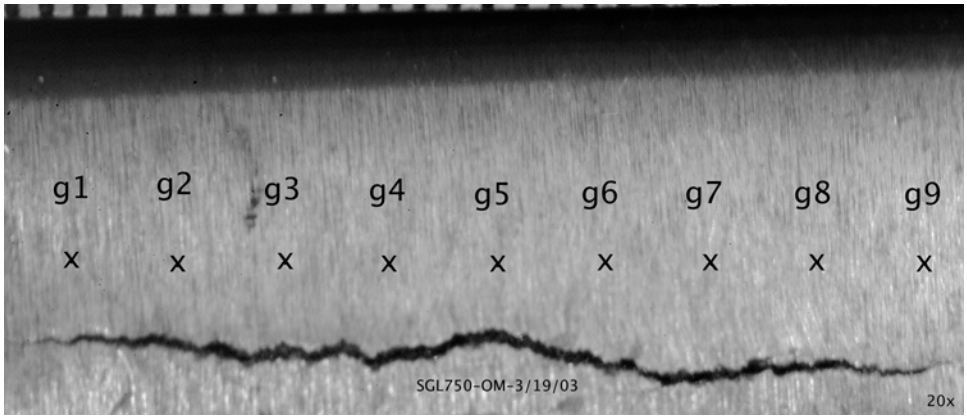

Figure 45. SCC axial flaw SGL750–OM–3/19/03.

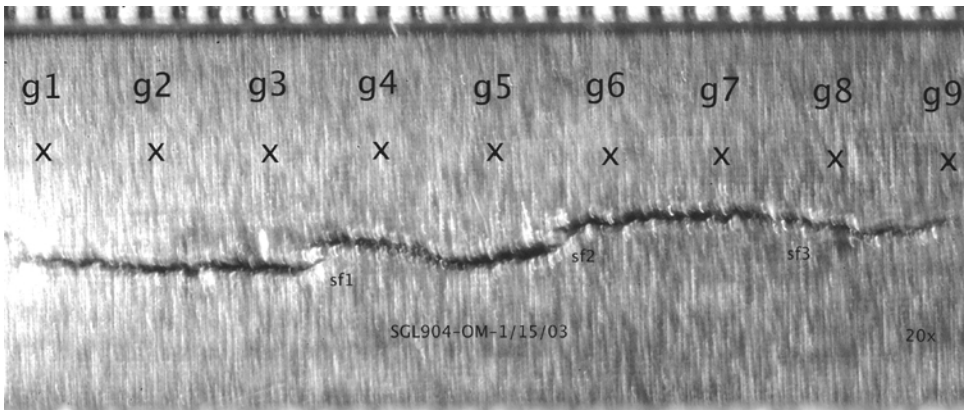

Figure 46. SCC axial flaw SGL904–OM–1/15/03.

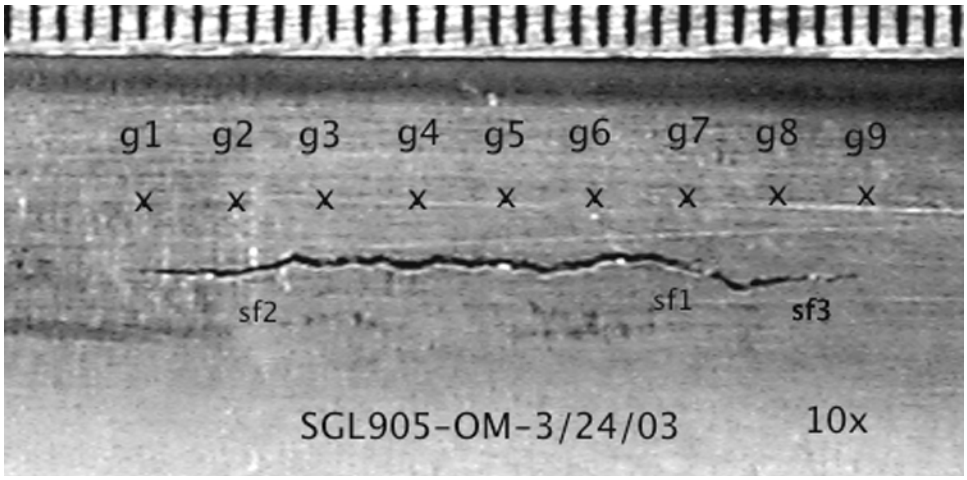

Figure 47. SCC axial flaw SGL905–OM–3/24/03.

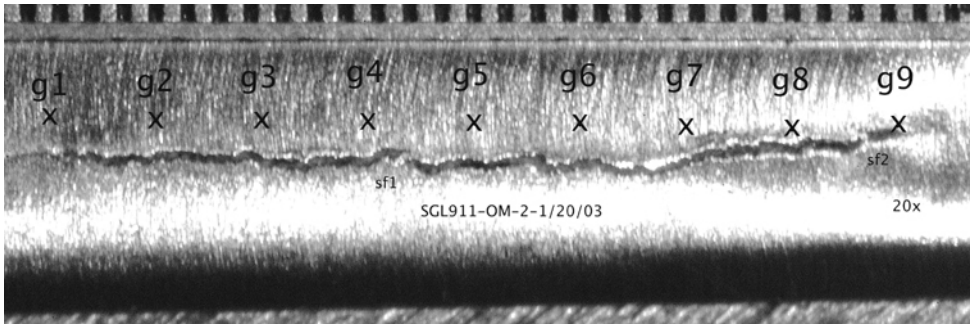

Figure 48. SCC axial flaw SGL911–OM–2–1/20/03.

Figure 49 shows a magnified image of the feature sf1 identified in Fig. 46 on flaw SGL904–OM. The feature appears to be an intact or possibly torn ligament. This is one of two ligaments evident in this flaw at the end of Stage 1 testing.

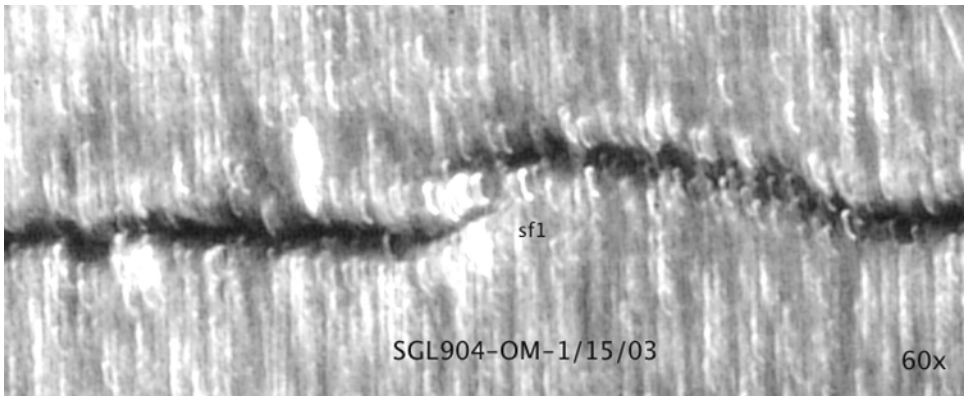

Figure 49. Magnified image of feature sf1 in SCC flaw SGL904–OM, which appears to be an intact or possibly torn ligament.

Several approaches were used to determine the flaw opening area. If the perimeter of the opening could be identified, image analysis software was used to calculate the enclosed area. The perimeters were highlighted either by drawing a line around the crack perimeter (the "wand" method) or using contrast to set the opening to white and everything else to black (the "threshholding" method). Fig. 51 shows a line drawn around the crack perimeter by the wand method. Figure 52 shows the crack opening for SGL905–OM highlighted by the threshholding method.

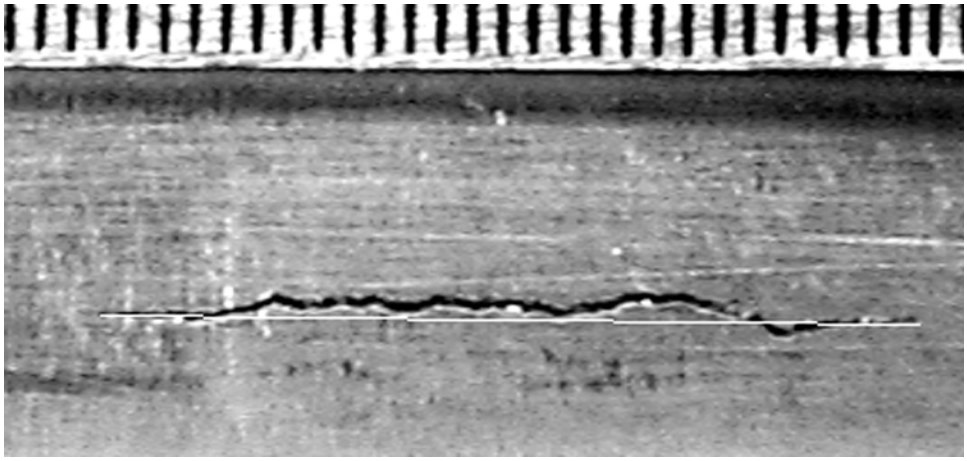

Figure 50. Image analysis line drawn between the end points of SCC flaw SGL905–OM used to calculate flaw length

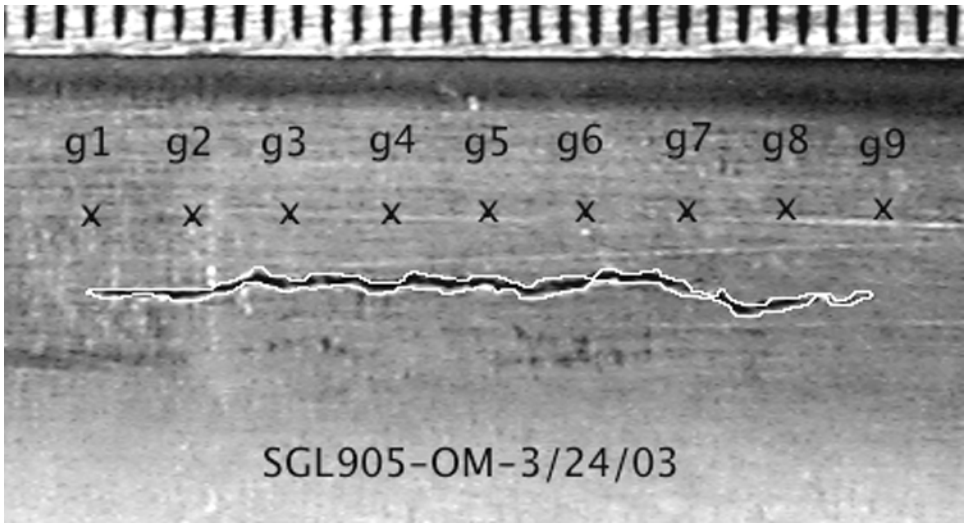

Figure 51. Image analysis line drawn around the crack perimeter of SCC flaw SGL905–OM by the wand method to define the opening

Figure 52. Crack opening of SCC flaw SGL905–OM highlighted by the threshholding method

Table 5 shows the lengths and areas of the flaws as determined by post–test image analysis as well as the pretest lengths determined by eddy current NDE and dye–penetrant exam. The eddy current estimates are based on conventional PlusPoint analysis. In most cases the wand and the threshholding methods gave similar results, but in some cases the differences were significant. For flaw SGL905–OM, the crack length is 10.7 mm (0.42 in.). The crack opening area was determined to be 1.44 mm^2 (0.00223 $in.^2$) by the wand method and 1.01 mm^2 (0.00156 $in.^2$) by the threshholding method. The wand method gave the most consistent agreement with the room–temperature, single–phase flow measurements when used with the orifice model .

The opening width of the cracks as a function of distance along the crack was measured from the images, and the values are given in Table 6. The widths at G1 and G9, which are the end points of the flaws, are zero and are not shown. The average opening width reported in Table 6 was calculated by averaging the values at locations G2 through G8. The measured widths can be used to compute an alternative estimate of flaw opening area, which is reported in the last column of Table 6. A comparison of these approximate areas with those presented obtained by image analysis shows reasonable agreement, but the areas determined by image analysis using the wand method are taken as the most accurate representation of the OD area of the crack.

Table 5 Axial crack lengths and opening areas after the RT tests

	Length, mm (in.)			Post–test Area, mm^2 ($in.^2$)	
Flaw ID	Eddy Current (Pretest)	Dye Penetrant (Pretest)	Image Analysis (Post–test)	Wand Traced	B&W Thresh–Holding
SGL750–OM–3/19/03	7.6 (0.3)	7.9 (0.31)	10.2 (0.40)	1.26 (0.00196)	1.39 (0.00215)
SGL904–OM–1/15/03	12.7 (0.5)	7.9 (0.31)	10.7 (0.42)	1.16 (0.00180)	*
SGL905–OM–3/24/03	10.2 (0.4)	5.8 (0.230	10.7 (0.42)	1.44 (0.00223)	1.01 (0.00156)
SGL911–OM–2–1/20/03	8.0 (0.3)	7.6 (0.30)	10.4 (0.41)	1.23 (0.00191)	*

*Thresholding difficult because the digital photos lacked sharp focus and the lighting caused glare from crack walls.

The disagreement between the pretest measurements of crack length by dye penetrant and the post–test measurements is not surprising. SCC cracks are typically very tight and it can be difficult to get the penetrant to penetrate the crack. However, the time dependent behavior of the leak rate shown in Figs. 43 and 44 indicates the situation is more complicated than simply the opening of a tight crack under load. At least for flaw SGL904 there is a visual indication of a ligament across the crack opening (Fig. 49). Thus part of the increase in leak could be associated with time–dependent failure of ligaments on the crack faces. The mechanical behavior of SG tubes at RT or at operating temperature is usually described in terms of time–independent plastic behavior. However, some short–term plastic behavior would not be unexpected, although steady state creep rates at these temperatures are very low. Even time–dependent failure of the ligaments and some time–dependent opening of the crack does not seem to completely explain the observed behavior, since these would be expected to lead to some stable, steady–state condition. Instead the leak rates in all cases seem to be increasing with time. Later tests have shown that it is possible to have crack growth driven by the dynamics of the leak jet, but in these tests no intermediate crack lengths were measured so it is not possible to distinguish clearly between the increase in leak rates associated with time dependent crack opening, ligament failure, and jet–driven crack growth.

Table 6 Variation of the opening width along the crack, average crack opening width, flaw length, and area.

	Width at Locations g1, g2,... along the Flaw, mm (in.)							Ave. width mm (in.)	Flaw length, mm (in.)	Flaw area, mm^2 ($in.^2$)
Flaw ID	g2	g3	g4	g5	g6	g7	g8			
SGL 750	0.10 (0.00413)	0.16 (0.00642)	0.15 (0.00587)	0.15 (0.00587)	0.06 (0.00241)	0.10 (0.00409)	0.10 (0.00413)	0.12 (0.004700	10.1 (0.398)	1.21 (0.00187)
SGL 904	0.08 (0.00299)	0.05 (0.00192)	0.07 (0.00278)	0.08 (0.00320)	0.07 (0.00256)	0.14 (0.00533)	0.06 (0.00235)	0.08 (0.00302)	10.8 (0.425)	0.83 (0.00128)
SGL 905	0.09 (0.00349)	0.09 (0.00349)	0.15 (0.00581)	0.09 (0.00349)	0.12 (0.00465)	0.12 (0.00465)	0.09 (0.00349)	0.11 (0.00415)	10.6 (0.416)	1.12 (0.00173)
SGL 911	0.11 (0.00439)	0.11 (0.00443)	0.11 (0.00439)	0.10 (0.00376)	0.11 (0.00443)	0.11 (0.00439)	0.11 (0.00443)	0.11 (0.00432)	10.4 (0.409)	1.14 (0.00177)

3.3.2 Stage 2 High Temperature Test Results Under Postulated MSLB Condition

Circular Orifice

A 1.59–mm (1/16–in.)–diameter EDM circular orifice was tested as a reference case. This orifice leaks at about the same rate as the SCC flaws tested in this series. At RT with 17.2 MPa (2500 psi) internal pressure and zero back–pressure, the observed leak rate was 12.6 kg/min (27.7 lbs/min). A value of 13.1 kg/min (28.8 lbs./min) was obtained in Stage 1 testing in the High–Pressure Facility. At 288°C (550°F) with 17.2 MPa (2500 psi) internal pressure and zero back–pressure, the leak rate was 11.3 kg/min (24.9 lbs./min). The mass flow rate ratio for the room–to–elevated–temperature is 12.6/11.3 = 1.11, which is close to the value of 1.15 predicted by the orifice model due to the change in density of the fluid.

For the same elevated temperature and internal pressure but with a back–pressure of 1.85 MPa (269 psi), the leak rate was 10.6 kg/min (23.3 lbs./min). The reduction in leak rate with an increase in back–pressure below the saturation pressure indicates that the flow was not choked. The orifice model for the circular hole predicted flow rates of 13.2, 11.4, and 10.8 kg/min (29.2, 25.1, and 23.8 lbs./min) for the room–temperature test, the elevated–temperature test with zero back–pressure, and the elevated–temperature test with a back–pressure of 1.85 MPa (269 psi), respectively. Hence the flow model gives good predictions under this non–choked condition.

Stress Corrosion Cracks

Flaws SGL750, SGL904, SGL905, and SGL911 were tested first at a 17.2 MPa (2500 psi) internal pressure level and zero back–pressure at RT. The elevated–temperature cases were then tested for the same internal pressure with increasing levels of back–pressure to determine if choked flow occurs.

SGL905 had a flow rate of 7.6 kg/min (16.8 lbs./min) at room–temperature with 17.2 MPa (2500 psi) internal pressure and zero backpressure. This is reasonably close to the Stage 1 leak–rate value of 8.0 kg/min (17.6 lbs./min). At the 288°C (550°F) test with 17.2 MPA (2500 psi) internal pressure and zero back–pressure, the flaw leaked at a rate of 14.0 kg/min (30.8 lbs./min).

The back–pressure was then raised to 2.34 MPa (340 psi) back–pressure, yielding a flow rate of 13.9 kg/min (30.6 lbs/min). Comparison of the zero and non–zero back–pressure cases reveals essentially identical flow rates, indicating a choked flow condition. At a back–pressure of 8.83 MPa (1280 psi), the flow rate was 10.98 kg/min (24.21 lb/min), which indicates the flow was not choked, and that the back–pressure was too high for choking to occur. The pressure ratio of downstream to upstream was 0.512, which is below the critical value of 0.528 for choked flow of gas through a converging nozzle.

SGL904 yielded a flow rate of 7.5 kg/min (16.6 lbs./min) at room–temperature with 17.2 MPa (2500 psi) internal pressure and zero backpressure. This compared favorably to the Stage 1 leak–rate value of 9.0 kg/min (19.9 lbs./min). For the 288°C (550°F) test at 17.2 MPa (2500 psi) internal pressure with zero back–pressure, the flaw leaked 15.0 kg/min (33.1 lbs./min). The mass flow rate ratio for the room–to–elevated–temperature testing is 16.6/33.1 = 0.50. Assuming a crack length of 11.2 mm (0.44 in.), a reduction in yield stress with temperature of 15%, and the orifice flow model, a ratio of 0.61 is expected.

At 288°C (550°F) test at the 17.2 MPa (2500 psi) internal pressure, Flaw SGL904 was then tested with 4.08 MPa (593 psi) back–pressure, yielding a flow rate of 15.0 kg/min (33.0 lbs/min). Comparison of the zero and non–zero back–pressure cases reveals essentially identical flow rates, indicating a choked flow condition. At a back–pressure of 5.90 MPa (855 psi), the flow rate was 13.0 kg/min (28.7 lb/min), which indicates the flow was not choked. After elevated–temperature testing with 17.2 MPa (2500 psi) internal pressure and zero backpressure, SGL904 yielded a flow rate of 19.2 kg/min (42.2 lbs./min) under room–temperature testing. This is much larger than would be expected simply from the increased plastic deformation that occurred due to decrease in yield stress during testing at 288°C. Comparison of Figs. 46 and 54 suggests that ligaments were present after that RT test that failed during the high temperature test.

SGL750 was tested with 17.2 MPa (2500 psi) internal pressure and at 288°C (550°F) with no back–pressure and a back–pressure of 3.84 MPa (557 psi) yielding flow rates of 12.8 and 12.3 kg/min (28.1 lb/min and 27.0 lb/min), respectively. In contrast to SGL905 and SGL904, SGL750, which is nominally about the same length as the other two flaws, exhibited a reduction in leak rate with an increase in back–pressure indicating the flow was not choked.

SGL911 was tested with 17.2 MPa (2500 psi) internal pressure and at 288°C (550°F) with no back–pressure and a back–pressure of 5.12 MPa (742 psi), yielding flow rates of 9.6 and 9.0 kg/min (21.2 lb/min and 19.9 lb/min), respectively. Hence, this SCC flaw, like flaw SGL750, exhibited a reduction in leak rate with an increase in back–pressure; indicating the flow was not choked.

Thus, for the four SCC flaws tested at 17.2 MPa (2500 psi) and 288°C (550°F), SGL904 and SGL905 appear to exhibit choking, and SGL750 and SGL911 do not.

Figs. 53–56 show images of flaws SGL750, SGL904, SGL905 and SGL911 after Stage 2 testing. The reference points (g1– g9) again denote the locations at which the flaw opening was

measured and sf1, sf2, etc. again denote special features of note. Comparison of the post–test Stage 1 and Stage 2 flaw areas shows that each flaw area has increased between 100 to 275% from the end of Stage 1 testing to the end of Stage 2 testing.

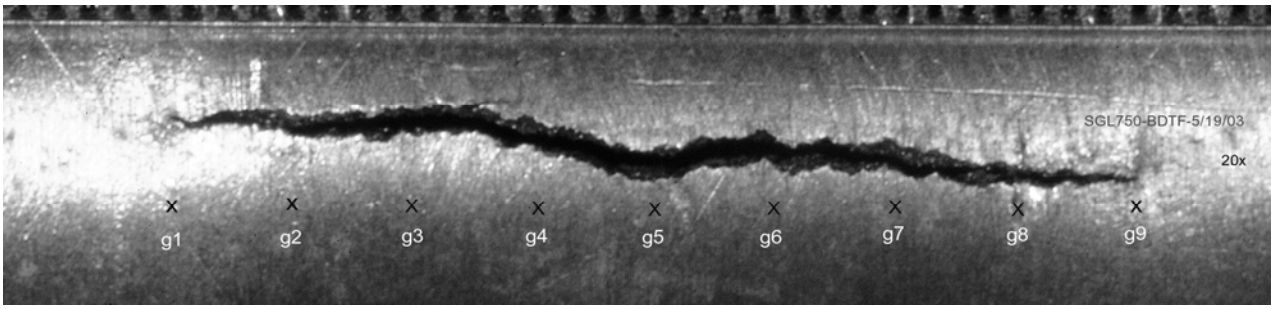

Figure 53. Stage 2 SCC axial flaw SGL750 after the high temperature test.

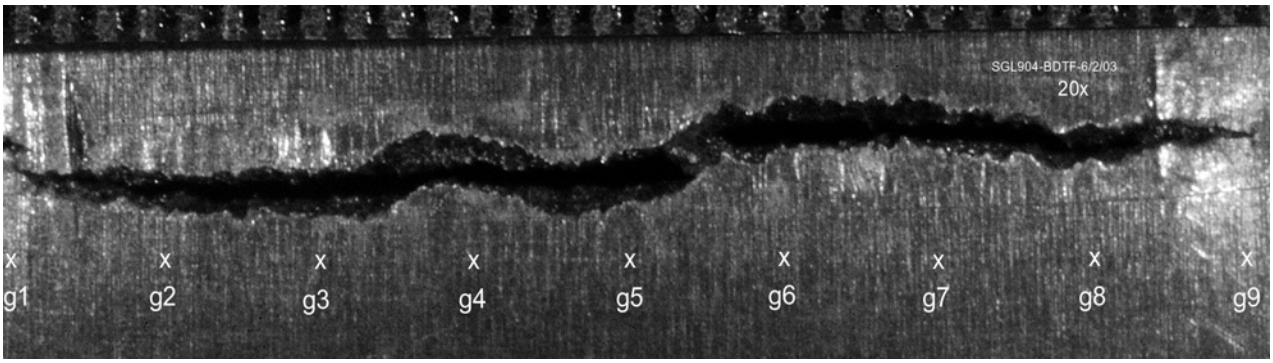

Figure 54. Stage 2 SCC axial flaw SGL 904 after the high temperature test.

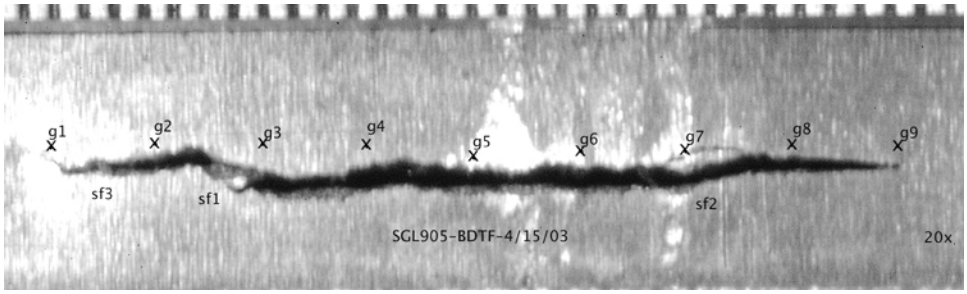

Figure 55. Stage 2 SCC axial flaw SGL905–BDTF–4/15/03.

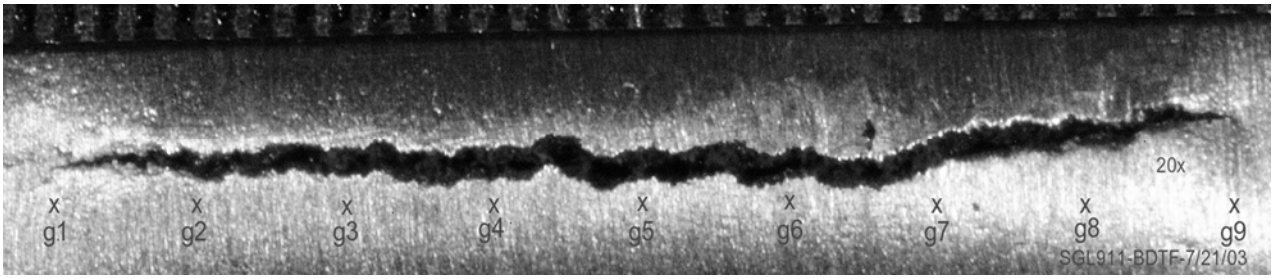

Figure 56. Stage 2 SCC axial flaw SGL911 after the high temperature test.

The geometry of the crack openings after the high temperature tests are summarized in Table 7. A hydraulic diameter, D, was defined as 4A/P where A is the area of the flaw and P is the

perimeter. For cracks, D is 2δ where δ is the opening width. For the 1.59 mm (1/16–in.)–diameter EDM circular hole flaw the hydraulic diameter is equal to the geometric diameter. The ratio of the wall thickness to hydraulic diameter gives the effective L/D for the flaw. For the flaws tested, L/D ranges from 1.7 to 3.2. Larger L/D ratios would be associated with larger frictional flow losses and would tend to lead to choked flow. Because two of the flaws had choked flow and two did not, this suggests that the transition to choked flow will occur for L/D ratios in the range of 2–4, i.e., for cracks of the order of 12 mm (0.5 in.) for postulated MSLB pressures and a temperature of 288°C (550°F). The critical value would be expected to depend on the degree of subcooling. In the tests summarized in Table 7, the subcooling is representative of that expected in the cold leg. In the hot leg, where the subcooling is less, choking would be expected to occur with smaller frictional losses, i.e., for smaller L/D ratios (i.e., larger flaws). Thus using a value of L/D of 5–10 to describe the onset of choking would be conservative for leaks in both the hot and cold leg.

Table 7 Crack opening geometries and flow behavior in tests at 288°C.

Flaw	SGL905	SGL904	SGL750	SGL911	1/16–in Orifice
Choked	Yes	Yes	No	No	No
Flaw Area mm^2 ($in.^2$)	2.97 (0.00461)	4.32 (0.00671)	3.10 (0.00481)	2.36 (0.00366)	1.97 (0.00306)
Flaw Length, mm (in)	11.2 (0.442)	11.9 (0.470)	11.3 (0.446)	12.0 (0.471)	1.5875 (0.0625)
Ave. Width, mm (in)	0.265 (0.01043)	0.365 (0.01438)	0.274 (0.01078)	0.197 (0.00777)	1.5875 (0.0625)
L/D	2.4	1.7	2.3	3.2	0.8

The crack opening areas on the OD and ID surfaces can be significantly different. To estimate this difference, finite element calculations were performed. The calculations were done with five layers of solid elements through the thickness. The results shown in Fig. 57 for 288°C suggest that the difference of about a factor of 1.4 between the OD and ID areas for a 12 mm (0.5–in) crack. The effect is smaller at low–temperature because of the higher yield strength. Shell–element solutions appear to give good approximations to the OD opening area, but overestimate the ID area. The closed form solution of Zahoor[7] gives reasonable to conservative solutions for the OD area when the yield stress is used to characterize the material.

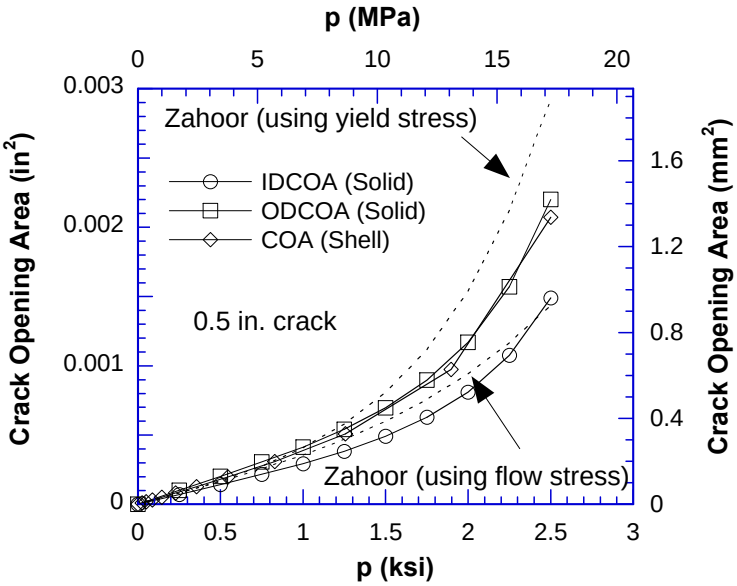

Figure 57.
Comparison of crack opening areas at the ID and OD for a 12.7 mm (0.5 in.) crack at 288°C. Results are shown for finite–element solutions using solid and shell elements as well as the analytical solution of Zahoor.

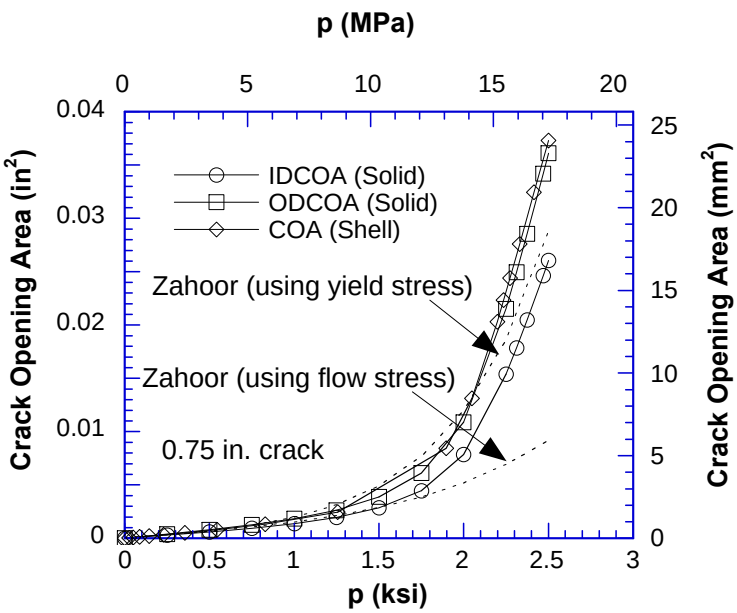

Figure 58.
Comparison of crack opening areas at the ID and OD for a 19.0 mm (0.75 in.) crack at 288°C. Results are shown for finite–element solutions using solid and shell elements as well as the analytical solution of Zahoor.

The flaw opening areas from image analysis of the flaws after the test together with computed corrections for the elastic contribution and the differences between the OD and ID opening areas were used to estimate the flow area. For the RT tests, the observed flows and the flows predicted using the estimated flow areas and an orifice coefficient of 0.6 are summarized in Table 8. The agreement between the observed and predicted flows is good and indicates that the orifice model has not been invalidated by flow path frictional losses for these flaws.

Similar results for the tests at 288°C are shown in Table 9. The predicted flows were again obtained from the orifice model using a coefficient of 0.6. The differences between the ID and OD areas are larger than in the RT case and both areas were used to compute predicted flows. For flaws SGL905, SGL904, which appeared to have choked flow, an estimate of the choked flow based on the assumption that for back–pressures less than the saturation pressure, p_{sat}, the effective pressure difference is $p - p_{sat}$.

Table 8. Comparison of orifice model predictions and experimental results for the RT tests.

Flaw	Image Analysis Flaw Area, mm^2	Observed Q, kg/min	Predicted Q kg/min
SGL750	1.26	8.5	8.4
SGL904	1.16	9.0	7.7
SGL905	1.43	8.0	9.5
SGL911	1.23	6.4	8.2

In Table 9, the observed and predicted flows for the tests at 288°C with different back–pressures are given. In addition to the actual predicted flows, normalized values that are scaled to agree with the observed flow rates for zero back–pressure were also computed. This reduces the effect of uncertainties in the flow area and orifice coefficient and provides a better estimate of the dependence on the pressure difference. The assumption that the effective pressure difference is $p - p_{sat}$ in the choked flow regime seems to be slightly conservative.

Table 9 Comparison of orifice model predictions and experimental results for the tests at 288°C for different back–pressures

Flaw	Back–pressure MPa	Observed Q, kg/min	Predicted Q Choked Flow kg/min	Predicted Q Non–choked kg/min	Normalized Q Choked Flow kg/min	Normalized Q Non–choked kg/min
SGL904	0	15.0	14.3	19.0	15.0	15.0
SGL904	4.08	15.0	14.3	16.6	15.0	13.1
SGL904	5.9	13.0	14.3	15.4	15.0	12.2
SGL905	0	14.0	9.8	13.1	14.0	14.0
SGL905	2.34	13.9	9.8	12.2	14.0	13.0
SGL905	8.83	11.0	9.1	9.1	12.9	9.8
SGL750	0	12.8	10.3	13.6	12.8	12.8
SGL750	3.84	12.3	10.3	12.0	12.8	11.3
SGL911	0	9.6	7.8	10.4	9.6	9.6
SGL911	5.12	9.0	7.8	8.7	9.6	8.0

3.4 Leak Rate Model

The tests reported here and previous results[3,4] show that the orifice model works well for flaws with $L/D \leq 3$–4. As shown in Fig. 59, this corresponds to cracks about 10–12 mm (0.43–in) under postulated MSLB pressures and to cracks about 25 mm (1–in) long under normal operating conditions. For shorter cracks where L/D can be much larger, frictional losses in the channels could be significant and lead to significant reduction in the flow rates predicted by the orifice model. Amos and Schrock[8] have conducted a series of tests on two–phase critical flow on rectangular slits in a plate of thickness 2.5 in. (6.35 cm) with the slit opening varying between

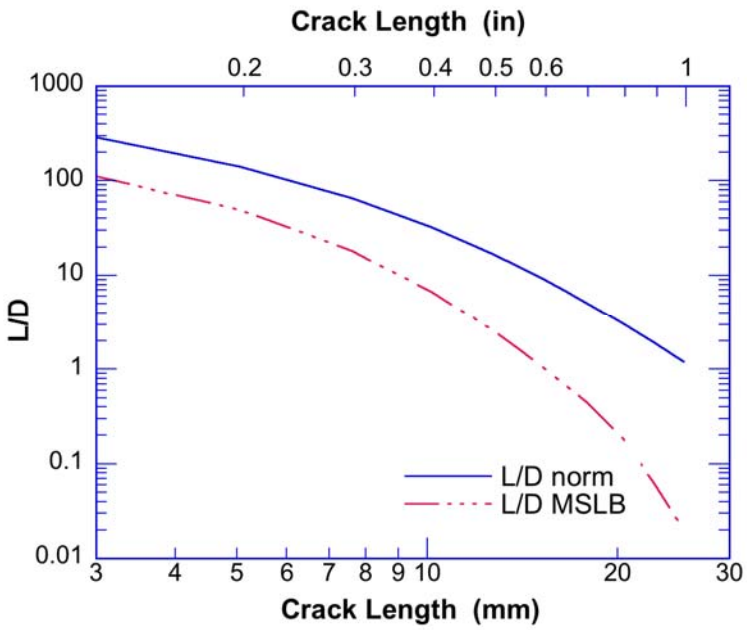

Figure 59.
L/D for cracks in SG tubes under normal operating pressures and postulated MSLB conditions. The flow length L is taken as the wall thickness and the hydraulic diameter D is 2δ, where δ is the average cracking opening.

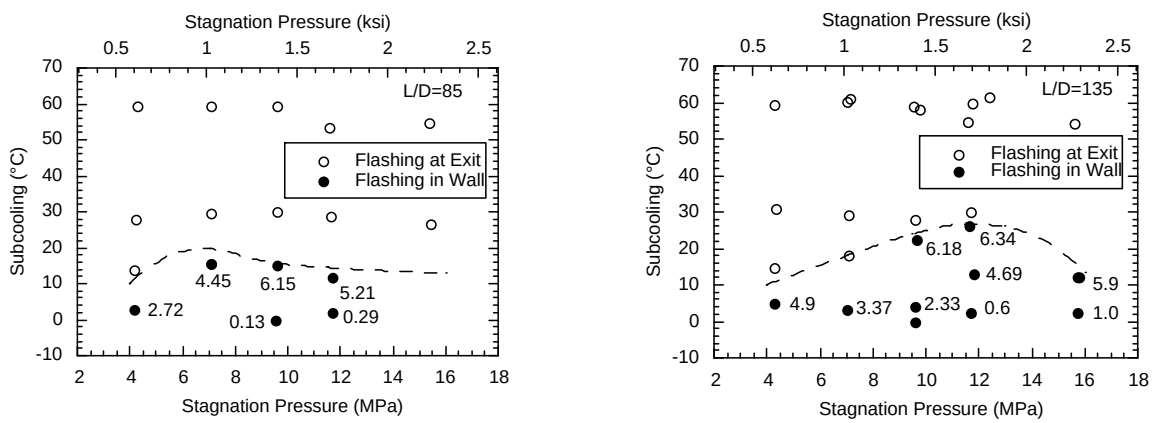

(a) (b)

Figure 60. Test results from Amos and Schrock[8] on flashing as a function of stagnation pressure and subcooling for (a) L/D=85 and (b) L/D=135. Numbers next to symbols denote location of flashing in cm from entrance (wall thickness=6.35 cm).

0.007 and 0.03 in. which gives L/D values of 85–300. Their results can be used to get insight into the effect of larger L/D values on the flow rate.

In the Amos and Schrock tests, the channels were instrumented so that it could be determined whether flashing was occurring within the channel or at the exit. Their results on flashing are shown in Figs. 60a–b. The dashed lines provides estimates of the minimum subcooling necessary to ensure that flashing does not occur inside the wall as a function of stagnation pressure, i.e., the pressure in the reservoir feeding the flaw, for values of L/D of 85 and 135. An L/D of 135 would correspond to about a 3 mm (0.12-in) crack in a steam generator tube under postulated MSLB conditions or about a 6 mm (0.24-in) crack under normal operating conditions (Fig. 59). The data show that the minimum subcooling initially increases with

stagnation pressure, but reaches a peak beyond which it either drops slightly (L/D=85) or drops substantially (L/D=135). The maximum value of subcooling needed to prevent flashing inside the wall increases from 20°C (stagnation pressure=1 ksi) to 26°C (stagnation pressure=1.7 ksi) when L/D is increased from 85 to 135 (i.e., when the crack becomes smaller). The pressures in the Amos and Schrock tests are lower than those of interest in PWRs, but the results suggest that for cracks with L/D ≤ 135 (i.e., for crack lengths > 3 mm (0.12-in) for postulated MSLB conditions), flashing within the wall of the steam generator tube would not occur in either the cold leg or the hot leg.

The flow in the channel wall is then single phase for L/D ≤ 135. The mass flow rate per unit area $\dot{M}$ for a single–phase flow though a long channel with friction is

$$\frac{\dot{M}}{\sqrt{2\rho\Delta p}} = \left(f \frac{L}{D} \right)^{-0.5} \tag{3}$$

where f is a friction factor (function of Reynolds number and surface roughness). For flow through an orifice

$$\frac{\dot{M}}{\sqrt{2\rho\Delta p}} = C_D \tag{4}$$

where C_D is the orifice discharge coefficient, which has a value of 0.6.

For the channel, the flow rate depends on L/D; for the orifice, it is independent of L/D. The loss factors computed from the tests of Amos and Schrock[8] on slits with opening varying from 0.007 to 0.03–in. at subcooling temperatures of 54–60°C and the steam generator flaw tests at ANL are shown as a function of L/D in Fig. 61.

A value of L/D ≈ 75 marks the transition between channel flow (dependent on L/D) and orifice flow (independent of L/D). L/D ≈ 3-4 marks the transition between a choked orifice and an unchoked orifice. For L/D > 4 the flow is always choked. Flashing will occur outside the wall for L/D < 135, but the flow will behave as though it is choked. For L/D > 75 in addition to the losses due to choking, frictional losses within the wall become important.

For L/D > 75 a fit to the Amos and Schrock[8] data gives

$$\frac{\dot{M}}{\sqrt{2\rho\Delta p}} = 13.44 \left(\frac{L}{D} \right)^{-0.72} \tag{5}$$

The observed dependence on L/D is reasonably close to that expected for single–phase flow. The data shown in Fig. 61 suggest that the orifice model should be valid for L/D < 75. This corresponds to cracks with an unligamented length > 5mm (0.2–in) for postulated MSLB pressures and > 8 mm (0.3–in) for normal operating pressures. For larger values of L/D the frictional losses in the channel dominate the expansion loss associated with the orifice. For L/D > 135 flashing could occur within the wall. This would result in an additional reduction in flow beyond that predicted by Eq (5).

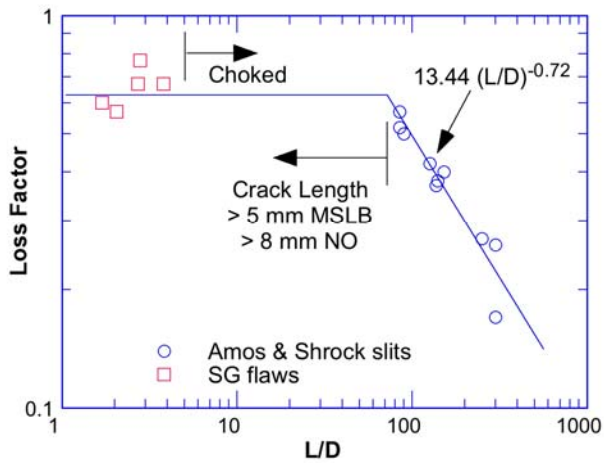

Figure 61.
Flow loss factor, $\dot{M}/\sqrt{2\rho\Delta p}$, as a function of L/D for Amos and Shrock slit tests[8] and tests on SG tubes.

Eqs (4) and (5) give the mass flow rate per unit area. To estimate the actual leak rate, an expression is needed for the crack opening area. The Zahoor model[7] for the crack opening area:

$$A = 2\pi c_e^2 V_o \sigma / E = \pi V_o (2c_e)(c_e \sigma / E) \tag{6}$$

where V_o is a geometry factor, c_e is the effective crack half length. σ is the hoop stress = $\Delta pR / h$, R and h = mean radius and thickness of tube, E is Young's modulus, S_y is the yield strength,

$$c_e = c\left[1 + \frac{F}{2}\left(\frac{\sigma}{S_y}\right)^2\right], \; F = 1 + 1.30\lambda^2 - 2.69\text{x}10^{-2}\lambda^4 + 5.35\text{x}10^{-4}\lambda^6 ,$$

$$\lambda^2 = c^2 / Rh ,$$

$$V_o = 1 + 0.65\lambda_e^2 - 8.97\text{x}10^{-3}\lambda_e^4 + 1.34\text{x}10^{-4}\lambda_e^6 , \; \lambda_e^2 = c_e^2 / Rh$$

and c is the half length of the crack, has been found by comparison with finite–element analyses and experiment to give good estimates of the crack opening area until the pressure begins to approach that for unstable burst. The average crack opening displacement is

$$\delta = A/2c.$$

Although flashing did not occur within the channel for L/D < 135 in the Amos and Shrock tests, in the current tests on steam generator flaws, choked flow was observed to occur for L/D ≈ 3–4. This result and the results shown in Fig. 61 are strictly valid only for the case where the subcooling is 50–60°C, i.e., cold leg conditions. Amos and Schrock[8] attribute the departure from the expected choked behavior when flashing occurs to the kinetics of the flashing process. The fluid passes through the narrow steam generator wall so quickly that there is not enough time for it to flash and thus it acts and behaves more like a single phase liquid. For the lower values of subcooling in the hot leg, the flow would be expected to flash more readily than under cold leg conditions, and would be expected to be choked at lower values of L/D than measured in our current tests. Because choking will result in lower flow rates, the current model will thus tend to overpredict leak rates in the hot leg for a range of L/D values between those assumed to produce

choking here (3–4) and the somewhat lower values of L/D that actually characterize choking in the hot leg.

The flow rate equations and their expected regions of validity are summarized as follows:

$$\frac{\dot{M}}{\sqrt{2\rho\Delta p}} = 0.6 \qquad L/D \le 75 \tag{7}$$

$$\frac{\dot{M}}{\sqrt{2\rho\Delta p}} = 13.44\left(\frac{L}{D}\right)^{-0.72} \qquad L/D > 75$$

where for cracks L is the wall thickness and the hydraulic diameter D is twice the crack opening displacement. For very tight cracks, the effective length can be even longer than wall thickness because of crack meandering, but taking L as the wall thickness should give conservative estimates. The effective Δp is:

$$\Delta p = p - p_{back} \qquad L/D \le 5$$

$$\Delta p = p - p_{back} \qquad L/D > 5 \text{ and } p_{back} \ge p_{sat}$$

$$\Delta p = p - p_{sat} \qquad L/D > 5 \text{ and } p_{back} < p_{sat}$$

where p_{back} is the secondary side back–pressure and p_{sat} is the saturation pressure. The value of L/D for the onset of choked flow has been taken as 5, since the tests indicated a transition value ranging from 2–4. The results are based on tests with 50–60°C of subcooling (cold leg conditions). The model should tend to overpredict leak rates for hot leg conditions for a range of L/D < 5. Eq (7) is similar to that proposed in Ref. 9, but in that case the flow was always assumed to be choked and no limits were proposed for L/D.

The uncertainties in prediction of leak rates through cracks will usually be dominated by uncertainties associated with crack geometry. The Zahoor model, Eq (6), gives a dependence of the crack opening area on the crack length approximately proportional to $c^{5.2}$. Thus, the presence of ligaments could change the leak rate by two orders of magnitude or more. Bounding estimates of crack length will typically grossly overestimate the leak rate.

3.5 Conclusions

Previous tests at ANL have shown that a single–phase orifice discharge model can accurately predict leak rates for flaws with widths as small as 0.18 mm (0.007 in.). Additional tests have been performed to better establish the range of validity of the orifice flow model. The tightness of cracks can be described in terms of the length of the flow channel L, approximately the wall thickness, and a hydraulic diameter D, which for a crack is taken as twice the crack opening displacement. The test results suggest that the critical value of L/D for the transition between choked and non–choked flow is on the order of 3–4. This value of L/D is strictly valid only for the value of the subcooling used in the tests, which corresponds to the cold–leg conditions. However, these values should give conservative estimates of the critical value of L/D for hot–leg conditions.

These results together with previous work by Amos and Shrock on flow through slits have been used to develop a simple leak rate model. A value of L/D ≈ 75 (7 mm, operating Δp; 4 mm,

MSLB) marks the transition between channel flow (dependent on L/D) and orifice flow (independent of L/D). L/D ≈ 3-4 (19 mm, operating Δp; 11 mm, MSLB) marks the transition between a choked orifice and an unchoked orifice. For L/D > 4 the flow is always choked. Flashing will occur outside the wall for L/D < 135 (5 mm, operating Δp; 3 mm, MSLB), but the flow will behave as though it is choked. For L/D > 75 in addition to the losses due to choking, frictional losses within the wall become important. For L/D > 135 flashing could occur within the wall. This would result in an additional reduction in flow beyond that predicted by the model.

The major uncertainty in applying the model is probably the actual crack geometry. Remaining ligaments could greatly reduce the actual crack opening area, which is usually estimated based on a simple, rectangular or elliptical crack shape.

4 Leak Rates in Restricted Areas

4.1 Introduction

Voltage-based alternate repair criteria have been established with regard to axial outside-diameter stress corrosion cracking (ODSCC) of steam generator (SG) tubes at tube support plates (TSPs). These criteria rely on an existing database for free-span leak rates from cracks to calculate the total leakage from tubes with indications remaining in service. The database for free-span leakage is utilized because the TSPs could displace laterally during postulated main steam-line break (MSLB) loading exposing the cracks under the TSPs. To justify leaving higher voltage indications in service, a few licensees have minimized the displacements of TSPs during transients by expanding a number of tubes above and below the TSPs to effectively lock the TSPs to the tubes. Although this procedure does mitigate the potential for burst and reduce leakage for cracks in the TSP regions, it will not eliminate the potential for leakage during postulated MSLB and severe accidents from such cracks.

The objective of the present study is to analytically predict flaw opening area at postulated MSLB pressure and expected leak rate from a crack, axial or circumferential, under the TSP. A second objective is to calculate the flaw opening and leak rates from similarly situated cracks as a function of time during postulated severe accidents.

4.2 Currently Available Leak Rate Data

4.2.1 Westinghouse/EPRI Tube/TSP Data

Under Electric Power Research Institute (EPRI) sponsorship, Westinghouse carried out a test program to develop a database for leakage from indications restricted from burst (IRB) for a wide range of crack sizes. An IRB is defined as a crack inside the TSP that would burst if located in the free-span region. The principal objective of the test program was to define a bounding leak rate for a limiting IRB in an unpacked crevice. Most of the tests were performed in a high-energy steam facility with flow capability up to 30 L/min (8 gpm). The steam-line break (SLB) conditions were taken as a primary coolant temperature of 324°C (615°F) and a pressure differential of 18 MPa (2.56 ksi). The high-temperature tests were augmented by tests in a room–temperature, high–pressure test facility.

Two types of tests were run. First, testing was done with the crack completely contained within the TSP and with one end of the crack aligned with the edge of the TSP. Second, testing was done with one tip of the crack positioned (offset) outside the TSP.

The test consisted of internal pressurization of the tube and measurement of the leak rate through the crack. To prevent leakage a bladder was inserted in the tube, and the crack was opened by pressurizing the tube to the predicted free-span burst pressure with the tube constrained within the TSP. After removing the bladder, leak rate tests were then conducted on these specimens. Fifteen tube specimens (Alloy 600 MA) were tested in this way. Specimens were prepared by (1) accelerated corrosion, (2) accelerated corrosion followed by fatigue cycling, and (3) laser cutting. The laser-cut specimens were rejected because they did not simulate the leakage

behavior of stress corrosion cracks. Eight of the specimens were 22 mm (0.875 in.) in diameter, and the rest 19 mm (0.75 in.) in diameter.

Cracks with lengths of 6 to 20 mm (0.24 to 0.809 in.) were tested. The TSP thickness of 19 mm (0.75 in.) implies that the longest axial crack that can be under the TSP is 19 mm (0.75 in.). The critical throughwall crack length in 19-mm (0.75-in.) diameter tubing with lower tolerance limit material under these pressure and temperature conditions always happens to be ≈19 mm (0.75 in.). To be conservative, the diametral clearance between the tube OD and the tube hole in the TSP was set at 0.6 mm (0.025 in.), which is significantly greater than the nominal 0.4 mm (0.016 in.) clearance in the Model 51 SG.

The bounding leak rate (21 L/min [5.5 gpm] at 18 MPa [2.56 ksi]) was determined from a single test with a crack length of 19 mm (0.76 in.) and supported by two other tests with long cracks. Tests with short cracks (< 10 mm [0.4 in.]) showed no interaction with the TSP because of the small opening at postulated MSLB pressure. Cracks with throughwall lengths ≥ 14 mm (0.55 in.) and a tube/TSP gap of 0.6 mm (0.025 in.) interacted with the TSP prior to reaching the postulated MSLB pressure. For these cracks, increasing Δp after this point did not cause further increases in leak rate. Initially, the limiting flow area is the crack opening area (COA), but as the crack is pressurized it becomes the gap flow area, which is twice the area between the TSP wall and the tube OD (Fig. 62) on the radial plane through the crack:

$$\text{Gap flow area} = 2 \int_{\text{crack}} (\text{gap})\, dx \tag{8}$$

where dx denotes integration along the tube axial direction.

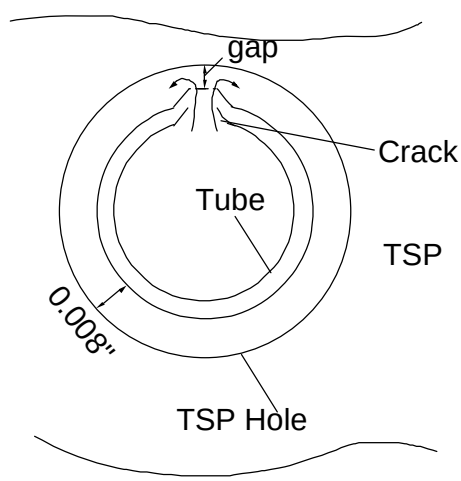

Figure 62. Gap flow area for a tube with an axial crack inside the TSP.

For such cracks, at some point increases in pressure increase the bulging and cause physical interaction between the crack flanks and the TSP, reducing the available flow area. Finally, further increases in pressure may cause the crack flanks to buckle toward the centerline of the tube, resulting in the tube being pressed tight against the TSP because of radial deformation due to elastic unloading of the crack flanks.

Except the data for the offset cracks, the leak rate data on specimens pre-deformed by pressurization with a bladder are plotted against the crack opening area and the gap flow area in Fig. 63. From the solid lines, it is evident that, except for a couple of tests with very small crack

opening area (and hence limited bulging), the correlation is better with gap flow area than with crack opening area. [Note that these data are for crevices that are unpacked with a diametral clearance between the tube OD and the TSP hole/wall of 0.6 mm (0.025 in.).]

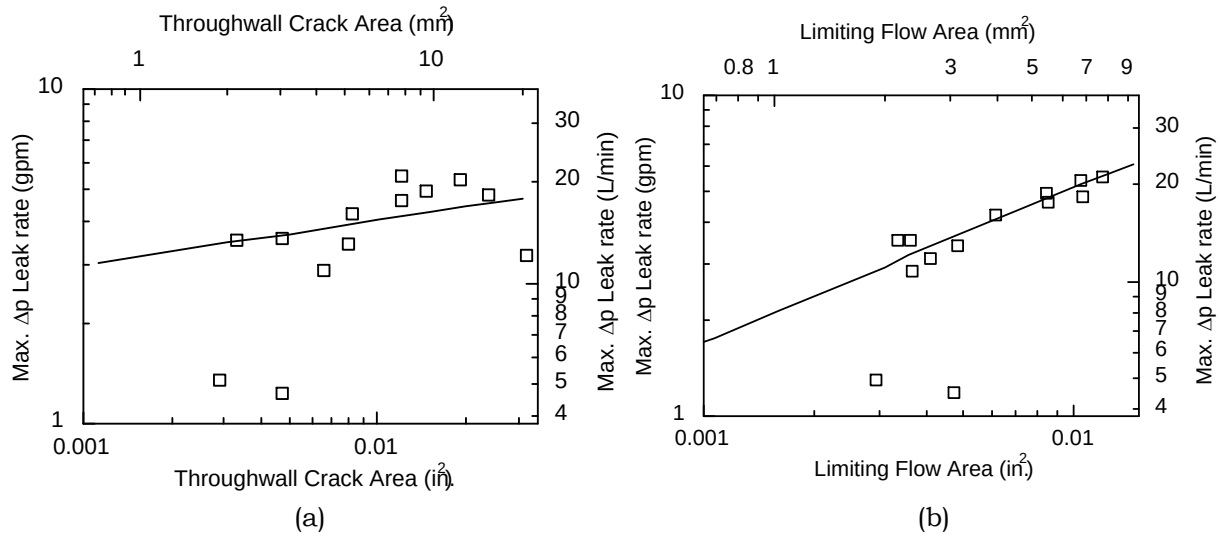

Figure 63. Correlation of leak rate data with (a) crack opening area and (b) gap flow area.

4.2.2 Dampierre-1 Tube/TSP Data

Intact tube/TSP junctions were removed from the French reactor Dampierre-1. Dampierre-1 commenced operation in 1980 and the SGs were replaced in 1990. All-volatile-treatment (AVT) water chemistry was used throughout the operation, and pH was controlled by ammonia addition until 1984 (8.8<pH<9.2) and morpholine after 1984 (9.1<pH<9.3). The assemblies included the tube, the surrounding TSP, and the crevice deposits, which held the tube in the TSP during removal. The crevice deposits were examined and were considered by Electricité de France (EdF) to be typical of SGs with drilled carbon-steel support plates. The removed assemblies were used to assess leak rates in the presence of crevice deposits and leak rates as a function of TSP displacement relative to the tube. The tests were run on crevices with and without chemical cleaning.

The leak tests were conducted at room temperature. A 0.5 mm (0.02 in.) hole was drilled through the middle of the TSP and through the deposits and the tube. The hole in the TSP was then plugged so that the leakage path from the 0.5 mm (0.02 in.) hole in the tube was through the crevice deposits. Without crevice deposits, the expected leak rate from a 0.5 mm (0.02 in.) hole at Δp=17.2 MPa (2.5 ksi) is 90 L/h (0.4 gpm). The measured leak rates through the deposit were < 0.1 L/h (4 x 10^{-4} gpm), which represents a reduction in leak rate of about a factor of 1000 due to the crevice deposits. The reduction factors from the drilled hole tests were considered to be conservative because they only include the flow resistance due to the presence of the deposits whereas the leakage from cracks within a packed crevice will also be reduced by the reduction in crack opening area due to presence of hard deposits in the crevice.

4.2.3 Tube/Tube-Sheet Data from a Retired Steam Generator

Several tube/tube-sheet (TS) junctions removed from a retired SG, including the crevice deposits, were leak tested at the ANL room-temperature, high-pressure test facility. The circumferential cracks in the specimens were very close to the top of the TS; therefore, the results are relevant to leakage under the TSP. The test data are summarized in Table 10.

The eddy-current (EC) measurements for specimen No. 6 indicated a circumferential ODSCC, with a maximum depth of 60% throughwall (TW) and 41 mm (250°) in length. Room-temperature pressure tests showed the beginning of a water leak at about 35.2 MPa (5100 psi) with a rate of 0.57 L/min (0.15 gpm). Specimen No. 6 was sectioned parallel to the tube axis, and the cross section was examined. Figure 64 is an optical metallograph of the cross section at the NDE indication of the maximum penetration. A circumferential crack initiating in the tube wall penetrates into the crevice deposit at the secondary side of the tube just above the top of the tube sheet (TTS).

Specimen No. 9 did not have any measurable leak rate up to a pressure of 52 MPa (7.5 ksi). However, post-test sectioning revealed the presence of a throughwall circumferential crack that is 0.04 mm (0.002 in.) wide (Figs. 65a-b). In contrast to specimen No. 6, the dense deposits in the TS crevice apparently prevented any leakage in this case even though the crack opening was relatively wide.

Tests on specimens 6 and 9 demonstrated that the leakage behavior of circumferential throughwall cracks at the top of tube-to-TS junctions in the presence of deposits can be widely different even in the same SG.

Table 10 A summary of leak test data for tube/TS specimens from a retired SG. Note 1000 psi = 6.895 MPa and 1 gallon = 3.8 L.

Tube Number	Plus Point Volts 1997	Plus Point Volts 2002	Pressure when leak rate was measurable (psi)	Leak rate (gpm)
6	1.54	2.95	5100	0.15
7	0.76	0.78	7300*	0.08
8	Not available	2.5	No leak to 7500 psi	No leak
9	2.36	24.85	No leak to 7500 psi	No leak

* Detected initiation of flaw weeping but no measurable leak rate at 6600 psi.

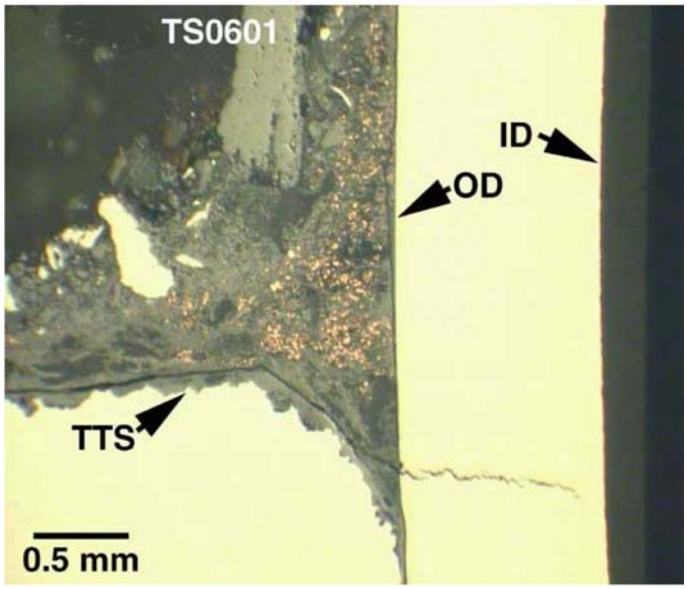

Figure 64. Optical metallography of a cross-section parallel to the tube axis at the maximum EC signals for TS0601 Alloy 600 SG tube specimen R39C43 near the TTS.

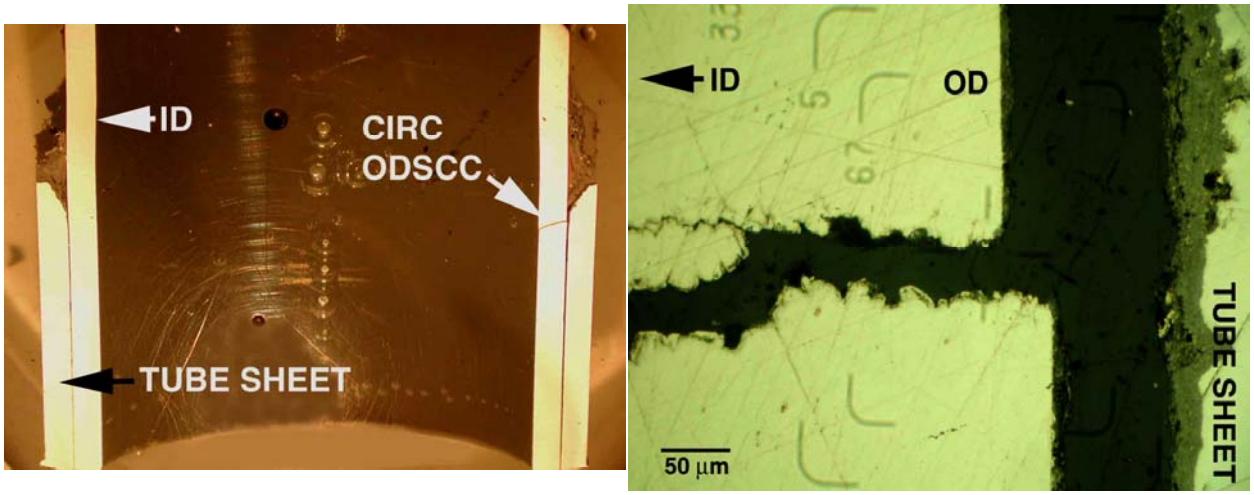

(a) (b)

Figure 65. A throughwall circumferential ODSCC with crack branching in specimen No. 9 just below the top of the tube sheet. The crack opening is about 0.04 mm.

4.3 Analyses of Crack Opening Area and Leak Rate

Finite element analyses (FEAs) were conducted for throughwall axial cracks, 13 mm (0.25 in.) and 19 mm (0.75 in.) long, and throughwall circumferential cracks, 90, 180, and 240° long. All of the tubes [22 mm (0.875 in.) OD and 1.3 mm (0.05 in.) wall thickness] were located symmetrically inside the TSP hole/wall with a 0.4 mm (0.016 in.) diametral clearance (Fig. 66). The circumferential cracks were located at the central plane of symmetry in all cases. No offsets of cracks or unsymmetrical positioning of the tube with respect to the TSP hole/wall were modeled. The TSP thickness was taken as 19 mm (0.75 in.). Most of the analyses ignored the effect of crevice deposits. A limited number of analyses were conducted to explore the effects of such deposits on crack opening area.

The limiting flow area for the leakage calculation was assumed to be the least of the following three quantities: the gap area (Eq. 1), the ID crack opening area, or the OD crack opening area. If there was a length of the crack flanks over which the radial gap between the tube OD surface and the TSP hole/wall was calculated to be fully closed, contributions from this portion of the crack to the gap area and the OD crack opening area were ignored. Because of the rotation of the tube wall associated with the bulging of the cracked section of the tube, the crack opening area was generally less on the ID than on the OD. Since the mechanical properties of the deposits are unavailable, leak rates were calculated assuming that the TSP crevices are free of deposits.

4.3.1 Leak Rate Correlation for a Postulated MSLB

An orifice discharge model has been found to be reasonably accurate for flow through cracks of length ≥ 11 mm (0.43 in.) for postulated MSLB conditions (see Section 3.4):

$$q_m = 0.6(2\rho\Delta p)^{1/2} \tag{9}$$

where q_m = mass flow rate per unit area, Δp = pressure difference across the tube, and ρ = density of water. In metric units (q_m in kg/m^2-s, Δp in MPa, and ρ in kg/m^3), Eq. 9 becomes

$$q_m = 848.3(\rho\Delta p)^{1/2} \tag{10}$$

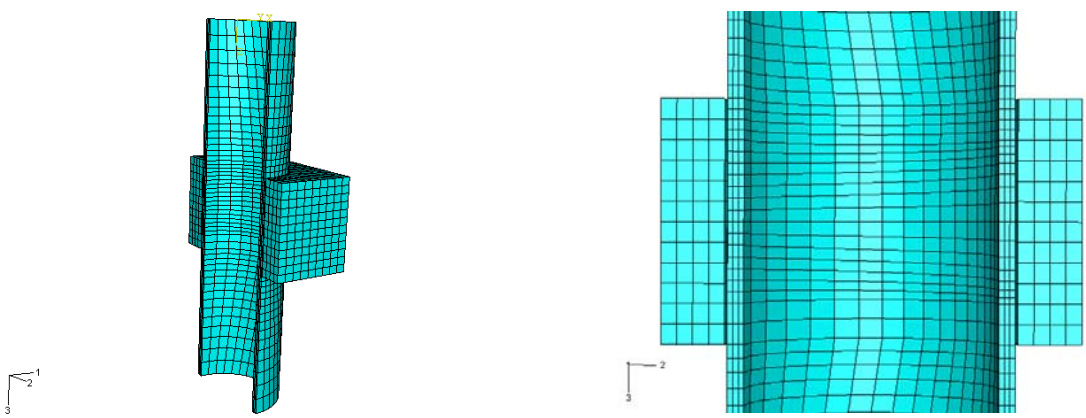

(a) (b)

Figure 66. Finite element model of the tube-to-TSP junction.

4.3.2 Leak Rate Correlation for Postulated Severe Accidents

Since the secondary side is at atmospheric pressure, it is reasonable to assume that the flow exiting the crack for a postulated severe accident is choked. Under these conditions, the exit velocity, pressure, and mass flow can be calculated with the additional assumption that the superheated steam can be treated as an ideal gas. The exit velocity is given by

$$V^* = \sqrt{\frac{2\gamma}{\gamma+1}RT} \tag{11}$$

where γ = ratio of specific heats at constant pressure and constant volume (1.4), R is the gas constant for steam (456 N-m/kg-K), and T is gas temperature in K. The mass flow per unit area (in kg/m^2-s) is given by

$$q_m = \left(\frac{2}{\gamma+1}\right)^{\frac{1}{\gamma-1}} \sqrt{\frac{2\gamma}{\gamma+1}\frac{p^2}{RT}} \tag{12}$$

where p = upstream gas pressure in Pa.

4.3.3 Material Properties Used in Analysis

Elastic Properties

The effective elastic constants for a TSP weakened by tube holes and flow holes were obtained from Westinghouse Electric Corporation data. The elastic modulus of Alloy 600 was assumed to be 193 GPa (28,000 ksi) with Poisson's ratio = 0.3.

Plastic Properties

The true stress-strain properties of Alloy 600, as reported in Ref. 10, are reproduced in Fig. 67. Because of the low stresses, the TSP was considered to behave elastically.

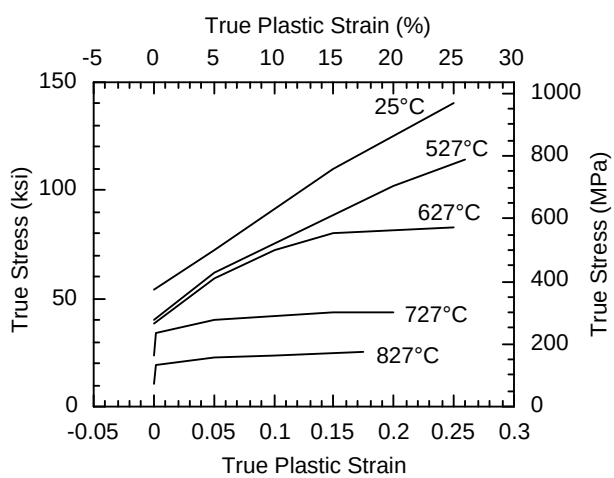

Figure 67. True stress-plastic strain curves for Alloy 600.

Creep Properties

The creep rate data of Alloy 600, as reported in Ref. 10, are reproduced in Fig. 68. The data can be fitted by the following equation:

$$\dot{\varepsilon}_c = 2.086x10^{24}\left(\frac{\sigma}{E}\right)^{4.8038} \exp\left(-\frac{65000}{RT}\right) \tag{13}$$

where σ = stress, E = Young's modulus, R = 1.987 cal/mol-K, and T = temperature in K. Because of the low stresses in the TSP, its creep deformation was ignored.

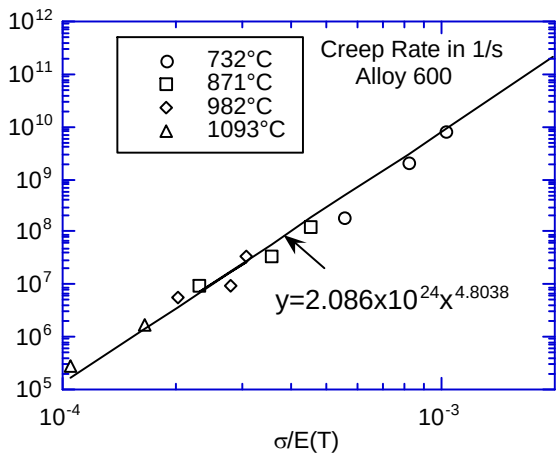

Figure 68. Creep rate properties of Alloy 600.

4.4 Results

4.4.1 Postulated Main Steam-Line Break (MSLB) Conditions

The internal pressure in the SG tube during a postulated MSLB accident was taken as a constant 17 MPa (2.5 ksi), with a constant temperature of 300°C.

Axial Crack

Two lengths of axial crack were studied: 13 and 19 mm (0.5 and 0.75 in.). The axial variation of the radial gaps between the crack flanks and the TSP tube hole/wall are shown as a function of pressure in Figs. 69a and b, respectively. The crack flanks of the 13 mm (0.5 in.) crack do not contact the TSP tube hole up to a pressure of 17 MPa (2.5 ksi). However, the flanks of the 19 mm (0.75 in.) crack make first contact with the TSP tube hole at a pressure of 12 MPa (1.8 ksi), and the radial gap is fully closed over a central length of 6 mm (0.25 in.) at 17 MPa (2.5 ksi).

The variation of the crack opening areas and the gap areas with pressure for 13 and 19 mm (0.5 and 0.75 in.) cracks is shown in Figs 70a and 70b, respectively.

In the calculation of the gap area, the contribution of the central portion of the crack, where the flanks make contact with the TSP hole/wall, to the integral in Eq. 8 is assumed to be negligible. In the calculation of the crack opening area for leakage, the contribution of the central portion of the crack opening area where the OD surface is in contact with the TSP is again taken as negligible. The limiting flow area for leakage, which is the least of the gap area, OD crack opening area, or ID crack opening area, can be taken as the lower bound of the curves shown in Figs 70a-b. For the shorter crack, the ID COA is always the limiting area. For the longer crack, the ID COA is limiting at operating pressure, but the gap area is limiting at postulated MSLB conditions.

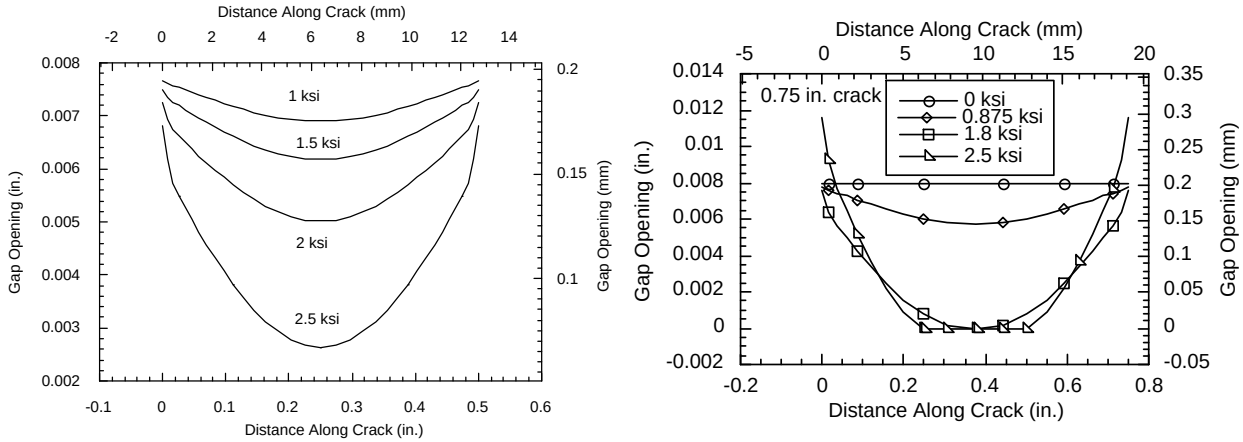

(a) (b)

Figure 69. Axial variation of radial gap between crack flank and the inner surface of the TSP tube hole with pressure for (a) 13 mm (0.5 in.) and (b) 19 mm (0.75 in.) axial cracks at 300°C.

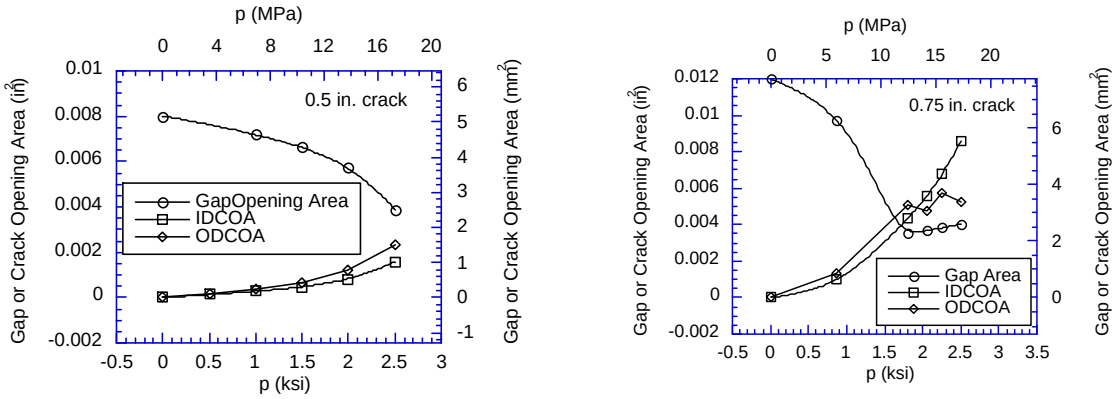

(a) (b)

Figure 70. . Variation of gap opening area, OD crack opening area, and ID crack opening area with pressure for (a) 13 mm (0.5 in.) and (b) 19 mm (0.75 in.) axial crack at 300°C.

The calculated leak rates as a function of pressure for 13 and 19 mm (0.5 and 0.75 in.) cracks are shown in Figs 71a and 71b, respectively. The leak rate for the 13 mm (0.5 in.) crack under the TSP is predicted to be the same as a free-span crack of the same length, because the tube OD surface at the crack section under the TSP does not contact the TSP hole/wall up to a pressure of 17 MPa (2.5 ksi), and the crack opening area at the ID surface controls the leakage in both cases (Fig. 71a). On the other hand, the tube OD with a 19 mm (0.75 in.) crack makes contact with the TSP hole/wall at a pressure of 12 MPa (1.8 ksi), as shown in Fig. 69b. Consequently, the leak rate curve diverges from that for the free span at pressures > 12 MPa (1.8 ksi), as shown in Fig. 71b, and at 17 MPa (2.5 ksi) the leak rate under the TSP is more than a factor of five less than the leak rate from the same size crack in the free-span region (Fig. 71b). At the postulated MSLB conditions, the leak rates for the 13 and 19 mm (0.5 and 0.75) cracks under the TSP are predicted to be 8 and 21 L/min (2 and 5.5 gpm), respectively. The results for the 19 mm crack are consistent with the Westinghouse/EPRI test data.

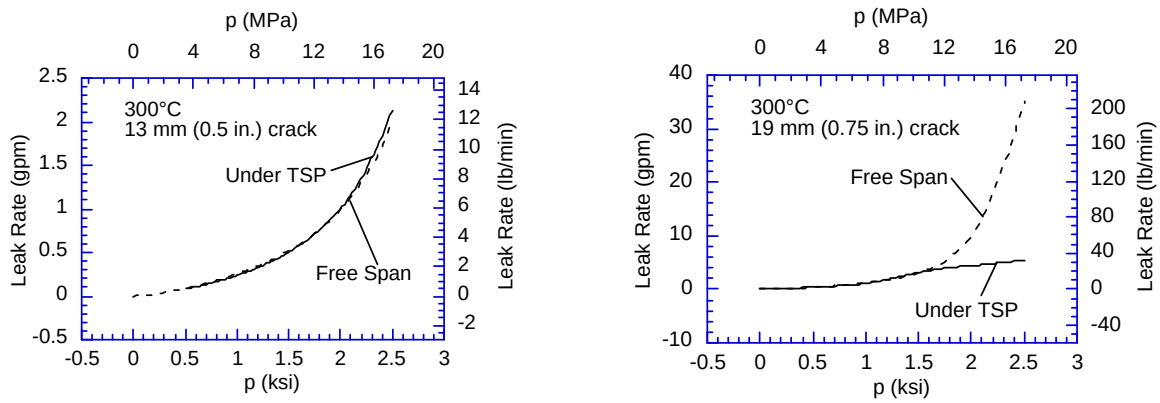

(a) (b)

Figure 71. Variation of leak rate with pressure for (a) 13 mm (0.5 in.) and (b) 19 mm (0.75 in.) axial crack at 300°C.

Circumferential Cracks

In comparison to axial cracks, circumferential cracks undergo much less radial bulging. As a result, the minimum crack extent for which contact between the tube OD surface and the TSP hole/wall occurs is about 180° at the postulated MSLB conditions of 17 MPa (2.5 ksi) and 300°C. The circumferential variations of the radial gap between the crack flanks and the TSP tube hole with pressure for 180 and 240° cracks are shown in Figs. 72a and 72b, respectively. Note that the contact length between the tube OD surface and the TSP hole/wall for a 240° crack at 7 MPa (1 ksi) is 4 mm (0.15 in.), which increases to 6 mm (0.25 in.) at a pressure of 17 MPa (2.5 ksi). The relative gap openings for 90, 180, and 240° cracks at the postulated MSLB pressure of 17 MPa (2.5 ksi) are compared in Fig. 73.

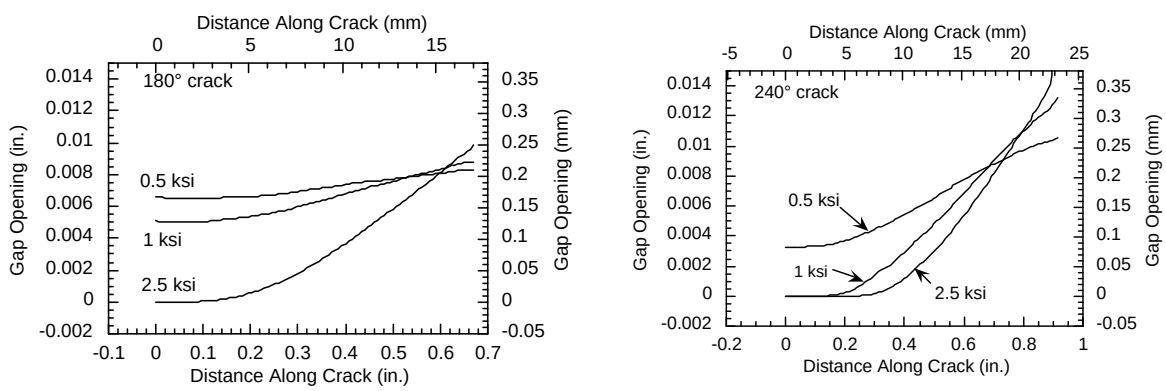

(a) (b)

Figure 72. Circumferential variation of radial gap between crack flank and the inner surface of the TSP tube hole with pressure for (a) 180° and (b) 240° cracks at 300°C.

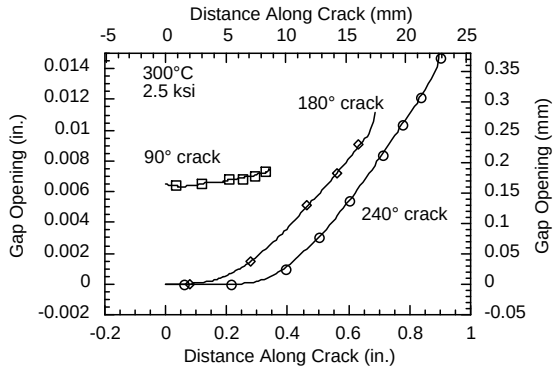

Figure 73. Radial gap variation between the tube OD surface and the TSP hole/wall for 90, 180, and 240° circumferential cracks at the postulated MSLB condition.

The variation of the ID crack opening area and the gap area with pressure for 90 and 180° cracks is shown in Figs 74a and 74b, respectively. The crack opening area is greater on the OD than the ID. The leakage-controlling area for both cases thus corresponds to the ID crack opening area.

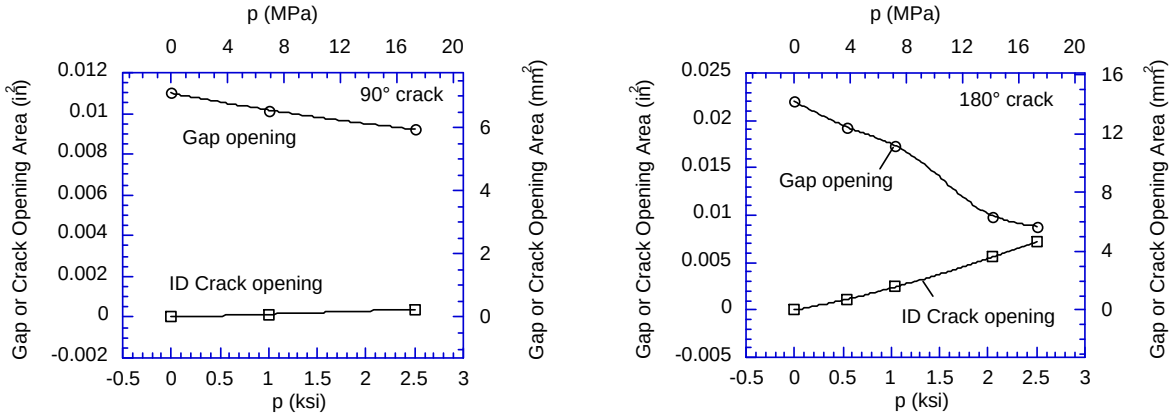

Figure 74. Variation of gap opening area and ID crack opening area with pressure for (a) 90° and (b) 180° circumferential crack at 300°C.

Since contact between the tube OD surface and the TSP hole/wall for a 240° crack occurs over a more extended region than the 180° crack, the leakage-controlling area changes with increasing pressure from initially the ID crack opening area, to the OD crack opening area, and finally to the gap area at 17 MPa (2.5 ksi), as shown in Fig. 75.

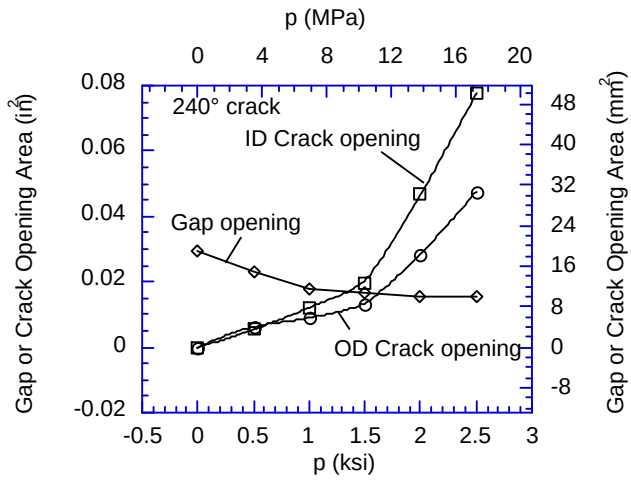

Figure 75. Variation of gap opening area and ID and OD crack opening areas with pressure for a 240° circumferential crack.

In Fig. 76, calculated leak rates are plotted against pressure for 90, 180, and 240° cracks. At the postulated MSLB condition, the leak rates for these cracks are predicted to be 2, 37, and 78 L/min (0.5, 9.7, and 20.6 gpm), respectively. Although very large circumferential cracks can result in high leak rates, the leakage for cracks in the TSP region is likely to be dominated by that due to axial cracks because circumferential cracks are not allowed to remain in service with the voltage-based alternate repair criteria.

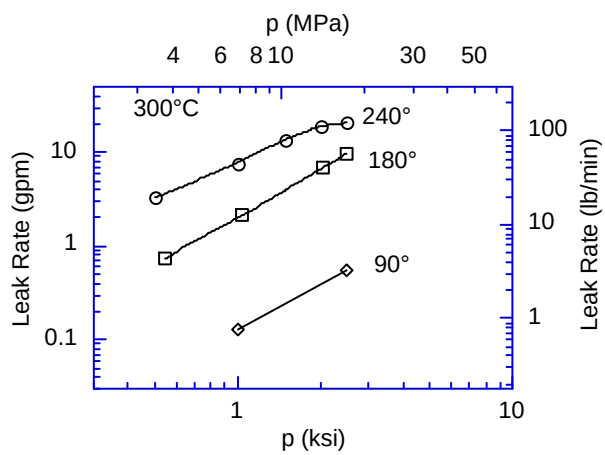

Figure 76. Variation of leak rate with pressure for 90, 180, and 240° cracks at 300°C.

4.4.2 Postulated Severe Accident Conditions

Representative temperature and pressure histories during the high temperature portion of the postulated severe accident transient are shown in Figs. 77a and 77b, respectively.[11] The maximum time is taken as 14,000 s because the surge line and hot leg are predicted to fail long before this time. Also, to be conservative, we assumed a constant pressure equal to 17 MPa (2.5 ksi).

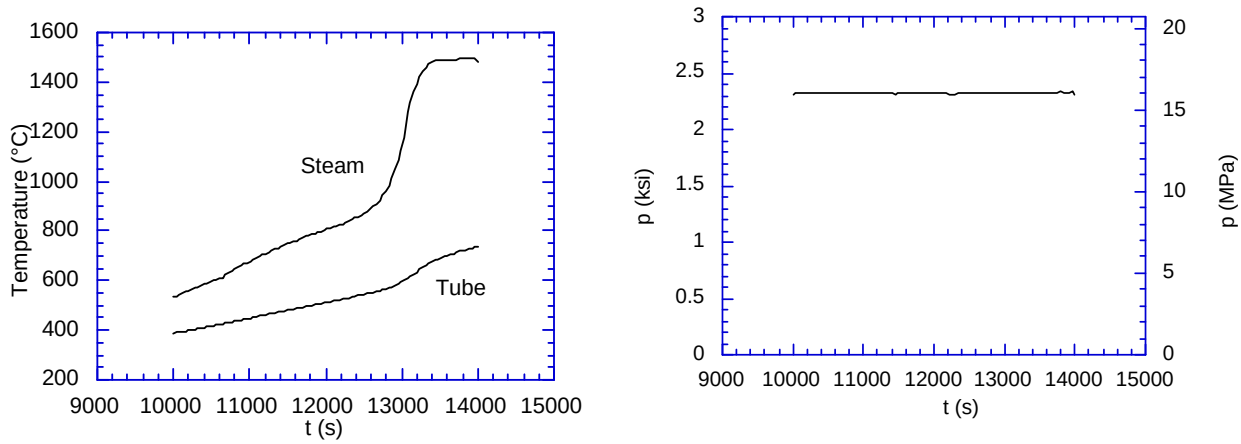

(a) (b)

Figure 77. Variation of (a) temperature and (b) pressure with time assumed for postulated severe accident analysis.

Axial Crack

The axial variations of the radial gap between the crack flanks and the TSP tube hole with time for 13 and 19 mm (0.5 and 0.75 in.) cracks are shown in Figs. 78a and 78b, respectively. Although initially at 17 MPa (2.5 ksi) pressure and low temperatures, the OD surface with a 13 mm (0.5 in.) crack does not contact the TSP hole/wall (Fig 69a). The first contact between the tube OD surface and the TSP hole/wall occurs at 12,690 s (Fig. 78a) during the transient. In the case of the 19 mm (0.75 in.) crack, the OD surface of the tube contacts the TSP hole/wall over a length of 6 mm (0.25 in.) at low temperature (Fig. 69b). At the end of 13,600 s, the contact length increases to 9 mm (0.35 in.), as shown in Fig. 78b.

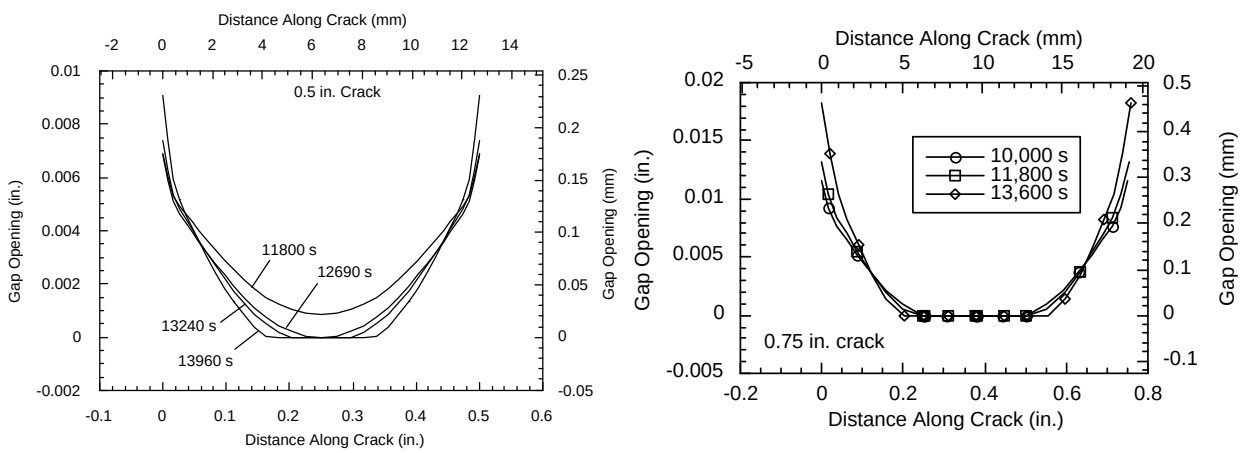

(a) (b)

Figure 78. Axial variation of radial gap between crack flank and the inner surface of the TSP tube hole with time for (a) 13 mm (0.5 in.) and (b) 19 mm (0.75 in.) axial cracks at a pressure of 17 MPa (2.5 ksi).

The crack opening area and the gap area vs. time for 13 and 19 mm (0.5 and 0.75 in.) cracks are plotted in Figs 79a and 79b, respectively. Because the first contact between the OD surface of the tube with a 13 mm (0.5 in.) crack and the TSP hole/wall occurs at time 12,600 s during the

postulated severe accident transient, and the contact length increases progressively with time, the controlling area for leakage changes from the ID crack opening area to the gap area at 12,600 s (Fig. 79a). For the 19 mm (0.75 in.) crack, the controlling area is the gap area at all times (Fig. 79 b).

The calculated leak rates as function of time for the 13 and 19 mm (0.5 and 0.75 in.) cracks are shown in Fig. 80.

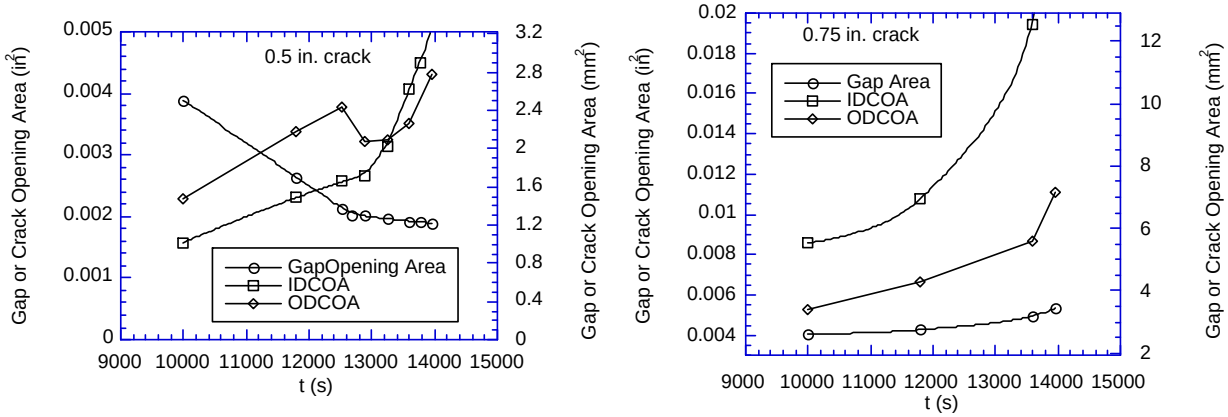

(a) (b)

Figure 79. Variation of gap opening area, OD crack opening area, and ID crack opening area with time for (a) 13 mm (0.5 in.) and (b) 19 mm (0.75 in.) axial crack.

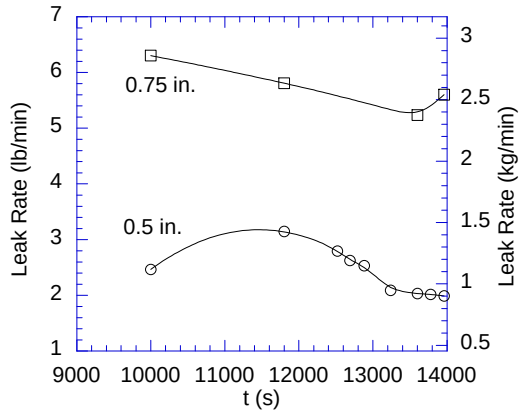

Figure 80. Variation of leak rate with time for (a) 13 mm (0.5 in.) and (b) 19 mm (0.75 in.) axial crack.

Circumferential Cracks

In contrast to axial cracks, the circumferential cracks deform little by creep during the postulated severe accident transient. As a result, the crack opening areas and gap area change very little with time, as shown in Fig. 81a-b for the 90° and 180° cracks and in Fig. 82 for the 240° crack. As in the postulated MSLB case (Figs. 74a-b and 75), the leakage-controlling area during the postulated severe accident for the 90 and 180° cracks is the ID crack opening area, and that for the 240° crack is the gap area. The leakage rates plotted in Fig. 83 show a slight reduction with time.

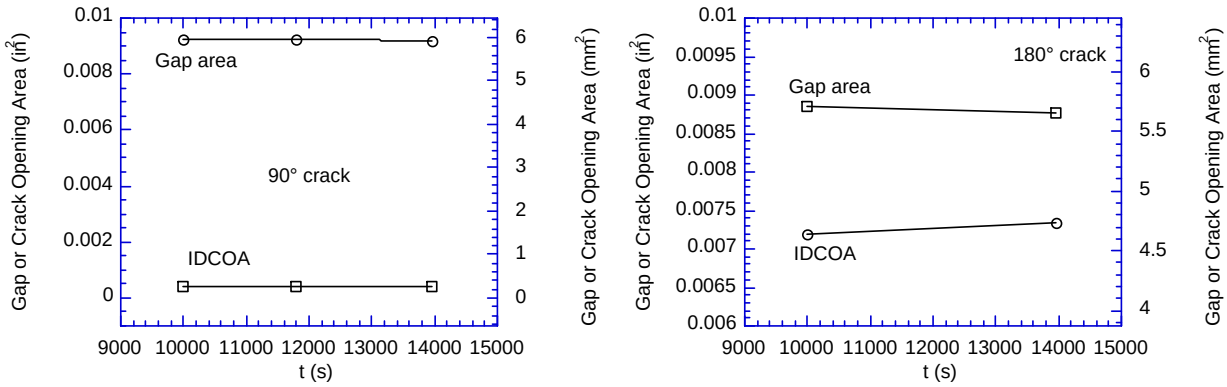

(a) (b)

Figure 81. Variation of gap opening area and ID crack opening area with time for (a) 90° and (b) 180° circumferential crack.

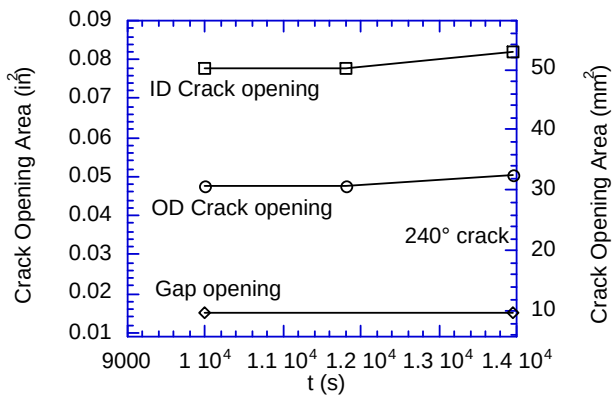

Figure 82. Variation of gap opening area and ID and OD crack opening areas with time for 240° circumferential crack.

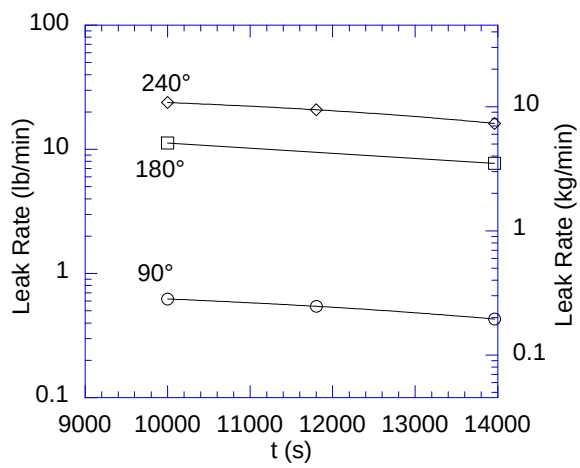

Figure 83. Variation of leak rate with time for 90°, 180°, and 240° circumferential cracks during a postulated severe accident.

4.5 Effect of Crevice Deposits on Crack Opening and Leak Rate

The leak rate results presented so far assume that there are no crevice deposits, so that the tube OD surface is free to bulge radially outwards up to 0.2 mm (0.008 in.) before making contact

with the TSP hole/wall. However, if deposits are present, they will affect the leak rate by two mechanisms. First, they will resist the radial growth of the tube and reduce the amount of crack opening area through which leakage occurs. Second, the leak rate itself will be reduced, depending on the porosity of the deposits.

The tests on the Dampierre-1 tubes, discussed earlier, showed that the reduction due to the flow resistance of the deposits alone may be as much as a factor of 1000. As reported earlier, two tests on the tube-to-TS junction specimens from the retired steam generator conducted at ANL showed different behavior. One leaked at a rate of 0.57 L/min (0.15 gpm) after the circumferential crack became throughwall at a pressure of 35.2 MPa (5.1 ksi). The other did not have any measurable leak rate up to a pressure of 52 MPa (7.5 ksi), even though post-test sectioning revealed a 0.04-mm (0.002-in.) wide throughwall circumferential crack. Thus, the effect of deposits on the leak rate varies widely.

The resistance provided by the deposits on the tube deformation will depend on its stiffness. Figure 84 shows the effect of the elastic modulus of the deposits on the crack opening displacement of a 13 mm (0.5 in.) axial crack under the TSP. Depending on the effective modulus of the deposits, the maximum COD may be reduced by almost a factor of 5 or perhaps more.

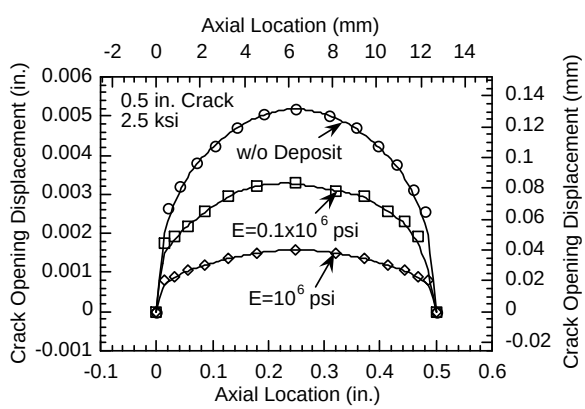

Figure 84. Effect of elastic modulus of deposits on the crack opening displacement of a 13 mm (0.5 in.) axial crack.

The mechanical properties of the crevice deposits are not well characterized. Although the elastic bulk modulus of pure crystalline magnetite is known,[12] it is not relevant for our purposes. More detailed information is available on deposits, which have some similarity to crevice deposits. The physical and chemical composition of deposits is complex. Turner et al. at Chalk River Laboratory[13] conducted a detailed study on the effect of chemistry on the hardness of deposits. The deposits are formed from corrosion products from the feed train, which are continuously fed into the steam generator during normal operation. Copper and iron species are the main corrosion products together with impurities such as silica, carbonate, sodium, magnesium, calcium, chloride, and sulfate. These chemicals are introduced to the feed train by the make-up water and condenser leakage and form a hard, consolidated deposits in the SG. The investigation at Chalk River[13] determined the effects of both physical and chemical processes on the consolidation and hardness of the deposits, which are a result of the elimination of porosity within the deposits in much the same way as sintering of ceramics. Tests were conducted in both isothermal and heat transfer conditions after corrosion products were added. Hardness of the deposits was measured by both the Vickers hardness number and crushing strength. Depending on the impurities, the deposits can be either soft or hard. A relatively small amount of chemical reaction or precipitation significantly increased hardness. All samples with added phosphates were harder than those without added phosphates and had significantly higher crushing strength. For example, the crushing strength of deposits made from a mixture of iron and cupric oxides increased from about

2 MPa with zero phosphate to a maximum 20 MPa with 3 mol % of phosphates. Similarly, 1 mol % addition of zinc silicate caused a maximum increase of the hardness of the deposits. Further increases of concentration of phosphates or zinc silicates actually reduced the hardness. Precipitation of soluble impurities, such as calcium sulfate, within the pores of the deposits was identified as an effective mechanism for deposits consolidation.

The parametric studies that have been performed show that the presence of deposits in the crevice is likely to have a significant impact on the effective leak area. However, to develop an FEA model for leak rate through cracks under TSPs with deposits, we will need better data on the mechanical properties of deposits as well as other physical properties, such as porosity and permeability, neither of which are currently available. Because of their strong dependence on chemistry, the physical and mechanical properties of the deposits may vary from plant to plant and maybe even from TSP to TSP in the same plant.

4.6 Conclusions

Finite element analysis of the SG tube with axial cracks under the TSP showed that the controlling leakage area during postulated MSLB and severe accidents is the ID crack opening area for short cracks [≤ 13 mm (0.5 in.)] and the gap area between the OD surface and the TSP hole/wall for longer cracks. This observation is in agreement with that reported by Westinghouse test results.

During a postulated MSLB, axial cracks ≤ 13 mm (0.5 in.) do not contact the TSP hole/wall with a radial clearance of 0.2 mm (0.008 in.), assuming there are no deposits in the crevice. This length is consistent with the maximum crack length of 14 mm (0.55 in.) reported by Westinghouse for a radial clearance of 0.3 mm (0.012 in.) between the tube OD surface and the TSP hole/wall. During postulated severe accidents, the tube OD surface makes contact with the TSP hole/wall at 12,690 s, and the contact length increases to 3 mm (0.1 in.) at 13,240 s.

In contrast to the 13 mm (0.5 in.) crack, the 19 mm (0.75 in.) crack does contact the TSP hole/wall over a length of 6 mm (0.25 in.) during MSLB. This observation is also consistent with that made by Westinghouse. During postulated severe accidents the contact length increases to 9 mm (0.35 in.) at 13,600 s.

In comparison to the axial cracks, the circumferential cracks undergo much less radial bulging during a postulated MSLB. As a result, the minimum crack length at which contact between the tube OD surface and the TSP hole/wall occurs is about 180° (corresponding to a length of 35 mm [1.4 in.]). The contact length between the tube OD surface and the TSP hole/wall for a 240° crack is 4 mm (0.15 in.).

In contrast to axial cracks, the circumferential cracks deform very little by creep during the postulated severe accident transient. As a result, the crack opening areas and gap area change very little with time during the postulated severe accident.

At the postulated MSLB conditions, the leak rates for 13 and 19 mm (0.5 and 0.75) axial cracks under the TSP are predicted to be 8 and 21 L/min (2 and 5.5 gpm), respectively. The leak rates for the 90, 180, and 240° circumferential cracks are predicted to be 2, 37, and 78 L/min (0.5, 9.7, and 20.6 gpm), respectively.

At 12,000 s during the postulated severe accident, the leak rates in the 13 and 19 mm (0.5 and 0.75) axial cracks under the TSP are predicted to be 1.4 and 2.6 kg/min (3 and 5.8 lb/min). The leak rates in the 90, 180, and 240° circumferential cracks at the same time are predicted to be 2.3, 4.5, and 9 kg/min (5, 10, and 20 lb/min), respectively, and they decrease slightly with time.

The calculated leak rates reported here assume that crevice deposits are absent. Tests on Dampiere-1 tube-to-TSP junctions, including deposits, showed that leak rates could be reduced by as much as a factor of 1000 compared to those without deposits. Studies on deposits carried out at Chalk River showed that the hardness, crushing strength, and consolidation properties of deposits depend strongly on the crevice chemistry. Small changes in crevice chemistry can lead to significant changes in these properties.

5 References

1. "Effect of Pressurization Rate on Degraded Steam Generator Tube Burst Pressure," Report TR–1006252, EPRI, Palo Alto, September 2001.

2. K. Kasza, S. Majumdar, J. Park, and J. Franklin, "Results from Pressure and Leak Rate Testing of Laboratory-Degraded Steam Generator Tubes," NUREG/CR-6789, Argonne National Laboratory, 2002.

3. S. Majumdar, K. Kasza, and J. Franklin, *Pressure and Leak–Rate Tests and Models for Predicting Failure of Steam Generator Tubes*, NUREG/CR–6664, Argonne National Laboratory, 2000.

4. S. Majumdar, S. Bakhtiari, K. Kasza, and J. Y. Park, *Validation on Failure and Leak–Rate Correlations for Stress Corrosion Cracks in Steam Generator Tubes*, NUREG/CR–6774, Argonne National Laboratory, 2002.

5. *Steam Generator Tubing Burst Testing and Leak Rate Testing Guidelines,* Report TR-1006783, EPRI, Palo Alto, December 2002.

6. F. Erdogan, "Ductile Failure Theories for Pressurized Pipes and Containers," *Int. J. Press. Vessels and Piping*, Vol. 4, pp. 253–283, 1976.

7. A. Zahoor, "Ductile Fracture Handbook," Electric Power Research Institute, Palo Alto, CA, 1989.

8. C. N. Amos and V. E. Schrock, "Two–Phase Critical Flow in Slits," *Nuclear Science and Engineering*, Vol. 88, pp. 261–274, 1984

9. E. Gillot, B. Cochet, P. Richard, and C.F. Faidy, "Validation of leak before break analysis for steam generator tubes", *SMIRT–9, Vol. D*, Lausanne, 1987.

10. J. L. Rempe, S. A. Chavez, G. L. Thinnes, C. M. Allison, G. E. Korth, R. J. Witt, J. J. Sienicki, S. K. Wang, L. A. Stickler, C. H. Heath, and S. D. Snow, "Light Water Reactor Lower Head Failure Analysis," NUREG/CR-5642, Idaho National Engineering Laboratory, 1993.

11. C. D. Fletcher, R. W. Shumway, and D. L. Barber, "Revised SCDAP/RELAP5 Base Case Calculation for Zion TMLB' Station Blackout Event", ISL-NSAD-TR-03-18, Information Systems Laboratories, Inc., Idaho Falls, ID, October 2003.

12. C. Haavik**,** S. Stolen, H. Fjellvag, M. Hanfland, and D. Hausermann, "Equation of State of Magnetite and Its High-Pressure Modification: Thermodynamics of the Fe-O System at High Pressure," American Mineralogist, Volume 85, pages 514–523, 2000.

13. C. W. Turner, M. E. Blimkie, and P. A. Lavoie, "Physical and Chemical Factors Affecting Sludge Consolidation," AECL-11674, COG-96-492-I, Chalk River Laboratories, Ontario, 1997.